Time domain terahertz electro- and magneto-optic spectroscopy

Moore, Graeme Patrick

Award date:
2001

Awarding institution:
University of Bath

Time Domain Terahertz Electro- and Magneto-Optic Spectroscopy

Submitted by Graeme Patrick Moore
for the degree of
Doctor of Philosophy
of the University of Bath
2001

Signed : 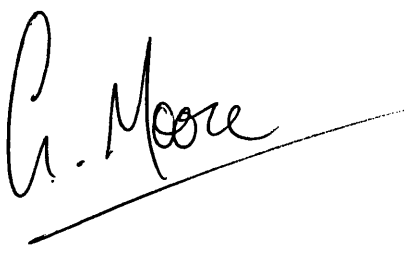

ProQuest LLC
789 East Eisenhower Parkway
P.O. Box 1346
Ann Arbor, MI 48106-1346

To John, Hilary, Audrey *&* Léo

Γνωθι Σαυτον

'Know Thyself'
Inscribed on the temple of Apollo in Delphi.

'Sing to me of the man, Muse, the
man of twists and turns
driven time and again off course,
once he had plundered
the hallowed heights of Troy.
Many cities of men he saw and
learned their minds,
many pains he suffered, heartsick
on the open sea,
fighting to save his life and bring
his comrades home

— Book I, 'The Odyssey' by Homer
(translated by R. Fagle).

Abstract

A time domain terahertz spectrometer and a bolometer have been used to study the coherent THz radiation emitted from n- and p-type InAs surfaces illuminated by femtosecond near infrared pulses. The magnetic field enhancement of the emitted average power in different polarisations and experimental geometries has been studied and is in qualitative agreement with the predictions of a Drude-Lorentz model for the radiation emitted by surface photocurrents. The dependence of the emitted radiation on the sample temperature, the sample doping density and type and the power density of the excitation beam has been studied. The emitted average power was found to decrease rapidly with increasing n-type doping, particularly above doping densities of $\sim 10^{18}\,\mathrm{cm}^{-3}$. A calibrated Golay cell was used to measure the absolute average power emitted under the different conditions, and the peak average power was measured to be $30\,\mu\mathrm{W}$ for an excitation beam of 1·2 W average power at 765 nm, and for a sample with a carrier density of $1{\cdot}7\times 10^{15}\,\mathrm{cm}^{-3}$ at 10 K and under the influence of a magnetic field of 5 T.

A report of InAs having been used as a source of coherent THz radiation for ultrafast spectroscopy, to probe optically excited cyclotron resonance in high resistivity silicon is presented. The masses of the carriers calculated from the cyclotron resonance measurements were found to be $m_{\perp} = 0 \cdot 19 m_e$ and $m_{\parallel} = 0 \cdot 90 m_e$. The temperature dependence of the cyclotron resonance was measured over the range 5 K to 80 K, and a peak is found at ~30 K which can be explained in terms of ionised and neutral impurity scattering at temperatures below 30 K and by phonon scattering above 30 K.

The measurement of small amplitude ferromagnetic resonance oscillations in the time domain in thin films of permalloy(78), iron and cobalt has been achieved by using the time resolved magneto-optic Kerr effect. A stripline device was fabricated to provide an out of plane broadband magnetic pulse with a peak strength of ~5 Oe. The observed frequencies are shown to agree well with the established theory.

Acknowledgements

Over the past four years there are many people to whom I am grateful for their support, guidance and friendship. With regards to the work presented in this thesis, I thank my supervisor Dr. Steve Andrews for giving me the opportunity to undertake the work, and for his guidance; in particular I would like to thank him for his assistance during the final stages of the work. I would like to thank Dr. C.C. Phillips and Dr. E.H. Linfield for providing the InAs samples. I would also like to thank Dr. Adam 'Barmy' Armitage for his help, guidance, instruction and general encouragement since his arrival half way through my studies. From early on, I thank Dr. Julian 'Fluffy' Cluff, Chris Shaw and Dr. Peter Huggard for the assistance they offered in the lab and the clean-room. I must also thank Dr. Sivaraya 'Siva' Sivapathasundaram and Wendy Lambson for their unwaivering support during the long hours in the cleanroom.

Away from work, I owe a big thank you to my friends from all over. To Caroline I owe a lot, and will never forget the support she gave me during the difficult times. My good friends Geoff, Sarah, Neil and Helen I thank for their patience and company. In Bath I would like to thank my old housemates Claudia and Jim for the friendship and general good times in Alpine Gardens — and 'The Bell'! I would also like to thank 'Evil' Gary for sharing his dubious sense of humour whilst sat in one of a range of pubs in Bath, along with Barmy. A lot of thanks has to go to Mark Acres, his generosity in keeping my communication lines open!, his proof reading and general constructive criticism of this thesis. Whilst all of this work was undertaken in Bath, I worked in Paris for 3 months after my funding had run out, and I would like to thank Dr. Jacques Ferré, Dr. Jean-Pierre Jamet, Dr. Alexandra Mougin, and of course Dr. Rhonda Hyndman, with whom I spent many hours extolling the virtues of Parisian life. I would also like to thank Françoise, for making me so welcome in Paris.

Finally there are four people to whom I dedicate this thesis, and to whom I owe more than anyone — my parents, John and Hilary, my grandmother, Audrey (rest in peace), and my close friend, Léo. Words cannot express how much I owe to the support, friendship, love and patience that all of you have given me.

Contents

List of Figures

List of Tables

Chapter 1

Introduction

The far infrared, or terahertz (THz), range of the electromagnetic spectrum is of great importance for the study of materials due to the large number of physical processes in this range. Initially, Fourier transform spectroscopy was the most popular technique to study the far-infrared spectrum. More recently however, the development of time domain terahertz spectroscopy has reinvigorated the field of far infrared (FIR) spectroscopy. The time domain spectrometer consists of many parts, but is essentially an extension of the work by Hertz on sparkgap dipole transmitters and receivers [1]. A modern development of Hertzian dipoles is the use of microfabricated, dipole antennae bridged by ultrafast photoconducting switches. These photoswitches were first developed by Auston *et al.* [2] and are commonly referred to as Auston switches.

The use of the microfabricated transmitter and receiver allows measurements to be made with sub-picosecond time resolution, and a sensitivity to average powers of $\sim$20 aW at room temperature. In addition, the detection is coher-

ent in that a measurement of the electric field amplitude and the phase can be made. The FIR properties of systems as wide ranging as semiconductors [3], dielectrics [3], superconductors [4], liquids, gases [5] and flames [6] have been investigated by time domain THz spectroscopy. Recent applications have been directed towards the study of coherent wavepacket dynamics in atoms and condensed matter [7], phonons [8], plasmons [9], cyclotron resonance [10], THz Hall measurements [11], scattering problems [12], intermolecular interactions [13] and plasma diagnostics [14]. The use of time domain THz spectroscopy has also been applied to medical tomography [15], in particular the imaging of teeth [16].

The development of ultrafast millimetre and sub-millimetre wave measurements began in 1981 with the realisation of photoconductive materials with sub-picosecond carrier recombination times [17]. This allowed the fabrication of photoconductive devices with switching speeds of a few picoseconds [18], and microstriplines down which the signals can propagate [19]. The research in this area was motivated by its potential as a tool for physical studies of the intrinsic physics of the building blocks of THz frequency systems such as switches, microstriplines and antennae [20, 21, 22].

Picosecond electrical pulses are commonly used to probe fast electrical circuits [23] but their propagation along the interconnects leads to distortion and attenuation of the pulse. To preserve the broad frequency content, Auston constructed photoconductive dipole antennae, excited by femtosecond visible or near infrared laser pulses in order to radiate the electric field pulses into free space in the form of THz beams [2]. To detect the radiated transients, a portion of the beam was delayed in time relative to the initial pulse and used to sample the free space transients by gating a similar photoconductive dipole connected to a current am-

plifier. The current, which is proportional to the detected electric field, was then recorded as a function of the delay between the pump and gate pulses. The freely propagating transient technique is inherently time domain and the final result of an experiment is the optoelectronically reconstructed time-domain signal [24]. Fourier analysis can be performed to convert the recorded traces to the frequency domain. This technique opened the way to THz transmission spectroscopy, and in a series of papers Fattinger and Grischkowsky [25] describe a range of improvements to the method culminating in a spectroscopic capability with an unrivalled sensitivity over the frequency range 0·1–3 THz.

In addition to the optoelectronic devices described above, co-development of purely optical THz radiation generation and detection techniques took place using electro-optic crystals. By utilising the process of optical mixing, an optical pulse travelling through an EO (electro-optic) crystal will create an associated second order polarisation wave. If the optical pulse is temporally short (picosecond or less), then the time-varying polarisation wave will radiate significant components in the THz frequency range [26, 27]. In order for the difference wave that is generated along the path of the pulse in the crystal to interfere constructively, the material must be either phase matched or short compared with the difference wavelength [28]. All optical detection can be achieved by measuring the polarisation rotation of a time delayed probe beam caused by the electric field of a THz transient passing through an EO crystal [26]. In order to optimise the time resolution the probe beam must pass through the EO crystal, colinearly with the transient. A recent report by Han *et al.* [29] discusses the differences between terahertz time domain spectroscopy and far infrared Fourier transform spectroscopy, and concludes that for frequencies <3 THz, the maximum sensitivity of the time domain system is generally six orders of magnitude better.

Some of the reports on the emission of THz radiation from InAs surfaces have used EO detection, *i.e.* all optical, rather than the optoelectric photoconducting switches. The dipole and all optical devices each offer their own advantages and disadvantages, and different combinations can be chosen to fulfill particular requirements. The dipole receivers are more sensitive than the EO crystals, but have a narrower bandwidth [30]. In addition, the dipole receivers are exceptionally stable, well matched to the dipole transmitter bandwidth and are not unduly sensitive to laser noise. The maximum bandwidth of the dipole receiver has recently been explored and a bandwidth of up to 20 THz has been reported [31, 32]. This improvement is due to the reduction in laser pulse duration to 12 fs. Bolometers can also be used to measure the radiation, but due to the response time, which is much greater than the temporal width of the THz transient, interferometric techniques must be used to recover frequency information.

The need to generate and detect broad-band THz radiation of sufficient brightness has lead to the investigation of different types of emitter [33, 34]. The illumination of bare semiconductor surfaces by ultrafast optical pulses to generate THz radiation has been reported over a number of years [35, 36] and the use of fabricated heterostructures to enhance the emitted radiation has been reported. The principle mechanism for the generation of the radiation is similar to the Auston switch in as much as the surface electric field that exists in some semiconductors acts to accelerate the photoexcited carriers [37]. Recently, a large magnetic field enhancement of the generation of THz radiation in InAs samples has been reported [38]. An average emitted power of 650 μW from InAs surfaces in a magnetic field of 1·7 T at room temperature and with a near infrared average pump power of 1·5 W was claimed. Given that this value is easily more than twenty times the typical average power that can be generated by a photogated transmitter, it has sparked

a great deal of interest in using InAs, and other semiconductors, as coherent THz sources.

As well as the electric field transient, the transmitters produce a magnetic field field transient, and by coupling this transient into free-space Riordan *et al.* performed an experiment based on the magneto-optic sampling of the magnetic field transient, by using a magneto-optic sensor [39]. For the time-resolved MOKE (magneto-optic Kerr effect) studies presented here, the magnetic field pulse associated with the transient current [40] in the stripline was used as a broadband magnetic driving field [41] to perturb the magnetisation of ferromagnetic thin films. A GaAs photoconductive switch similar in design to that used in the THz transmitters, was used in the construction of the time domain MOKE device. The initial work by Freeman *et al.* was concerned with the investigation of the spin lattice relaxation time in gold [42]. This was then followed by the measurements of ferromagnetic resonances in thin film permalloy [43]. Similar work by Hicken *et al.* [44, 45, 46] was performed on thin films of iron. Freeman *et al.* then went further and constructed an ultrafast Kerr microscope which has been used to study the magnetisation dynamics of micron scale elements of thin film permalloy [47]. Subsequently a theoretical description of some of the dynamics of precessional magnetisations was presented by He *et al.* [48] and extended by Zhang and Hübner [49]. Crawford *et al.* have recently shown that the coherent control of precessional dynamics in thin film permalloy can be achieved [50]. A more extensive discussion of the MOKE and the techniques used is given in Chapter 5.

Included within the work presented in this thesis is the study of the generation of THz electromagnetic radiation by the ultrafast optical excitation of InAs surfaces,

and the subsequent enhancement of the emitted radiation by the application of high strength magnetic fields. In Chapter 3 initially the average THz power that is generated is discussed in terms of the results obtained by using a Golay cell, and the average power of the emitted THz radiation is discussed in terms of a Drude-Lorentz model. Qualitative agreement is found for the more lightly doped n-type samples. The results of the magnetic field dependence of the emitted electric field transient detected by a dipole receiver are presented, and a model based on the coherent emission by bulk plasma oscillations is discussed.

Chapter 2 describes the way in which the TDTS operates and gives detailed descriptions of the most important components, such as the generation of the ultrashort optical pulses, the THz optics and the dipole receiver used to detect coherently the THz radiation. The THz frequency radiation generated in InAs was then used as a novel source of coherent THz radiation to perform sub-picosecond resolution time domain spectroscopy on optically excited cyclotron resonance in high resistivity silicon, as described in Chapter 4.

Chapter 5 describes the way in which an optical pump probe measurement technique was used to generate short duration broad-band magnetic fields and how the time resolved magneto-optic Kerr effect (MOKE) was used to detect small amplitude ferromagnetic resonances in different ferromagnetic materials.

References

[1] Edited by P. Hertz
'Heinrich Hertz.'
San Francisco Press Inc., 1977.

[2] D.H. Auston, K.P. Cheung & P.R. Smith
'Picosecond Photoconducting Hertzian Dipole.'
Applied Physics Letters, pp. 284–286, **45**(3), August 1984

[3] D. Grischkowsky, S.R. Keiding *et al.*
'Far Infrared Time-Domain Spectroscopy with Terahertz Beams of Dielectrics and Semiconductors.'
Journal of the Optical Society of America B, pp. 2006–2015, **7**(10), 1990;
'Electrical Characterization to 4 THz of n- and p-type GaAs Using THz Time-Domain Spectroscopy.'
Applied Physics Letters, pp. 840–842, **61**(7), 17^{th} Aug. 1992

[4] M.C. Nuss, K.W. Goosen *et al.*
'Terahertz Time-Domain Measurement of the Conductivity and Superconducting Band Gap in Niobium.'
Journal of Applied Physics, pp. 2238–2241, **70**(4), Aug. 1991

[5] M. van Exter, C. Fattinger & D. Grischkowsky
'Terahertz Time-Domain Spectroscopy of Water Vapor.'
Optics Letters, pp. 1128–1130, **14**(20), 15^{th} Oct. 1989.

[6] R.A. Cheville & D. Grischkowsky
'Observation of Pure Rotational Absorption Spectra in the ν_2 Band of Hot H_2O in Flames.'
Optics Letters, pp. 531–533, **23**(7), April 1998;
'Far Infrared THz Time Domain Spectroscopy of Flames.'
Optics Letters, pp. 164–168, **20**(15), Aug. 1995

[7] H.G. Roskos, M.C. Nuss *et al.*
'Coherent Submillimeter-Wave Emission from Charge Oscillations in a Double-Well Potential.'
Physical Review Letters, pp. 2216–2219, **68**(14), 6^{th} Apr. 1992

[8] C. Waschke, H. Roskos *et al.*
'Coherent Submillimeter-Wave Emission from Bloch Oscillations in a Semiconductor Superlattice.'
Physical Review Letters, pp. 3319–3322, **70**(21), May 1993

[9] W. Sha, A.L. Smith & W.F. Tseng
'Coherent Plasma Oscillations in Bulk Semiconductors.'
Physical Review Letters, pp. 4273–4276, **74**(21), May 1995

[10] D. Some & A.V. Nurmikko
'Real-Time Electron Cyclotron Oscillations Observed by Terahertz Techniques in Semiconductor Heterostructures.'
Applied Physics Letters, pp. 3377–3379, **65**(26), Dec. 1994

[11] W.J. Waleki, D. Some *et al.*
'Terahertz Electromagnetic Transients as Probes of a Two-Dimensional Electron Gas.'
Applied Physics Letters, pp. 1809–1811, **63**(13), Sept. 1993

[12] R.A. Cheville & D. Grischkowsky
'Properties of Surface Waves Determined via Ballistic THz Time Domain Spectroscopy.'
Physical Review E, pp. 1336–, **50**, 1994.

[13] B.N. Flanders, R.A. Cheville *et al.*
'Pulsed Terahertz Transmission Spectroscopy of Liquid $CHCl_3$, CCl_4, and their Mixtures.'
Journal of Physical Chemistry, pp. 11824–11835, **100**(29), July 1996

[14] R.A. Cheville & D. Grischkowsky
'Time Domain Terahertz Impulse Ranging Studies.'
Applied Physics Letters, pp. 1960–1962, **67**(14), 2^{nd} Oct. 1995

[15] D.M. Mittleman, S. Hunsche *et al.*
'T-ray Tomography.'
Optics Letters, pp. 904–906, **22**(12), June 1997

[16] D. Arnone, C. Ciesla & M. Pepper
'Terahertz Imaging Comes into View.'
Physics World, pp.35–40, **13**(4), April 2000

[17] P.R. Smith, D.H. Auston *et al.*
'Picosecond Photoconductivity in Radiation-Damaged Silicon-on-Sapphire Films.'
Applied Physics Letters, pp. 47–50, **38**(1), 1st Jan. 1981

[18] *'Picosecond Optoelectronic Devices'*
D.H. Auston
Academic Press, London, 1984

[19] M.B. Ketchen, D. Grischkowsky *et al.*
'Generation of Subpicosecond Electrical Pulses on Coplanar Transmission Lines.'
Applied Physics Letters, pp. 751–753, **48**(12), 24th March 1986

[20] M. van Exter & D. Grischkowsky
'Characterization of an Optoelectronic THz Beam System'
IEEE Transactions on Microwave Theory and Technique, pp. 1684–1691, **38**(11), Nov. 1990

[21] J.T. Darrow, X.-C. Zhang *et al.*
'Saturation Properties of Large-Aperture Photoconducting Antennas.'
IEEE Journal on Quantum Electronics, pp. 1607–1616, **28**(6), June 1992

[22] W.H. Knox
'Optical Properties of Quasi-Zero-Dimensional Magneto-Excitons.'
Applied Physics A, pp. 491–502, **A53(6)**, Dec. 1991

[23] *'Optoelectronic Techniques for Microwave and Millimetre-Wave Engineering.'*
W.M. Robertson
Artech House Publishers, London, 1995
ISBN: 0890067112

[24] D. Krökel, D. Grischkowsky & M.B. Ketchen
'Subpicosecond Electrical Pulse Generation Using Photoconductive Switches with Long Carrier Lifetimes.'
Applied Physics Letters, pp. 1046–1047, **54**(11), 13th March 1989.

[25] C. Fattinger & D. Grischkowsky
'Point Source Terahertz Optics.'
Applied Physics Letters pp. 1480–1482, **53**(16), Oct. 1988;
'Terahertz Beams'
Applied Physics Letters, pp. 490–492, **54**(6), Feb. 1989;
M. van Exter, Ch. Fattinger & D. Grischkowsky
'High-Brightness Terahertz Beams Characterized With an Ultrafast Detector.'
Applied Physics Letters, pp. 337–339, **55**(4), July 1983

[26] D.H. Auston
'Subpicosecond Electro-Optic Shock Waves.'
Applied Physics Letters, pp. 713–715, **43**(8), Oct. 1983

[27] X.-C. Zhang, B.B. Hu *et al.*
'Generation of Femtosecond Electromagnetic Pulses from Semiconductor Surfaces.'
Applied Physics Letters, pp. 1011–1013, **56**(11), 12th March 1990.

[28] A. Yariv
'Optical Electronics'
CBS College Publishing, New York, 1985.

[29] P.Y. Han, M. Tani *et al.*
'A Direct Comparison Between Terahertz Time-Domain Spectroscopy and Far-Infrared Fourier Transform Spectroscopy.'
Journal of Applied Physics, pp. 2357–2359, **89**(4), Feb. 2001.

[30] Y. Cai, I. Brener *et al.*
'Coherent Terahertz Radiation Detection: Direct Comparison Between Free-Space Electro-Optic Sampling and Antenna Detection.'
Applied Physics Letters, pp. 444-446, **73**(4), July 1998.

[31] S. Kono, M. Tani *et al.*
'Detection up to 20 THz with a Low-Temperature-Grown GaAs Photoconductive Antenna Gated with 15fs Light Pulses.'
Applied Physics Letters, pp. 4104–4106, **77**(25), Dec. 2000.

[32] S. Kono, M. Tani & K. Sakai
'Ultrabroadband Photoconductive Detection: Comparison with Free-Space Electro-Optic Sampling.'
Applied Physics Letters, pp. 898–900, **79**(7), Aug. 2001.

[33] X.-C. Zhang & D.H. Auston
'Optoelectronic Measurement of Semiconductor Surfaces and Interfaces with Femtosecond Optics.'
Journal of Applied Physics, pp. 326–338, **71**(1), 1st Jan. 1992.

[34] X.-C. Zhang, Y. Jin *et al.*
'Magnetic Switching of THz Beams.'
Applied Physics Letters, pp. 2003–2005, **62**(17), 26th Apr. 1993.

[35] R. Kersting, J.N. Heyman *et al.*
'Coherent Plasmons in n-doped GaAs.'
Physical Review B, pp. 4553–4559, **58**(8), Aug. 1998.

[36] C. Weiss, R. Wallenstein *et al.*
'Magnetic Field Enhanced Generation of Terahertz Radiation in Semiconductor Surfaces.'
Applied Physics Letters, pp. 4160–4162, **77**(25), 18th Dec. 2000.

[37] Jacobsen RH, Birkelund K *et al.*
'Interpretation of Photocurrent Correlation Measurements used for Ultrafast Photoconductive Switch Characterization.'
Journal of Applied Physics, pp. 2649-57, **79**(5), March 1996.

[38] N. Sarukura, H. Ohtake *et al.*
'High Average-Power THz Radiation from Femtosecond Laser-Irradiated InAs in a Magnetic Field and its Elliptical Polarization Characteristics.'
Journal of Applied Physics, pp. 654–656, **84**(1), 1st July 1998.

[39] J.A. Riordan, F.G. Sun *et al.*
'Free-Space Transient Magneto-Optic Sampling.'
Applied Physics Letters, pp. 1452–1454, **71**(11), Sep. 1997.

[40] Z. Piao, M. Tani *et al.*
'Carrier Dynamics and Terahertz Radiation in Photoconductive Antennas.'
Japanese Journal of Applied Physics, pp. 96–100, **39**, Part 1, No.1, Jan. 2000.

[41] M.R. Freeman, M.J. Brady & J. Smyth
'Extremely High Frequency Pulse Magnetic Resonance by Picosecond Magneto Optic Sampling.'
Applied Physics Letters, pp. 2555–2557, **60**(20), May 1992.

[42] M. Johnson, A. Y. Elezzabi & M.R. Freeman
'Direct Measurement of the Conduction Electron Spin-Lattice Relaxation Time T_1 in Gold.'
Physical Review Letters, pp. 3220–3223, **77**(15), 7th Oct. 1996.

[43] W.K. Hiebert, A. Stankiewicz & M.R. Freeman
'Direct Observation of Magnetic Relaxation in a Small Permalloy Disk by Time-Resolved Scanning Kerr Microscopy.'
Physical Review Letters, pp. 1134–1137, **79**(6), 11th Aug. 1997.

[44] J. Wu, J.R. Moore *et al.*
'Optical Pump-Probe Studies of the Rise and Damping of Ferromagnetic Resonance Oscillations in a Thin Fe Film.'
Journal of Magnetism and Magnetic Materials, pp. 189–198, **222**, 2000.

[45] R.J. Hicken & J. Wu
'Observation of Ferromagnetic Resonance in the Time Domain.'
Journal of Applied Physics, pp. 4580–4582, **85**(8), April 1999.

[46] R.J. Hicken & J. Wu
'Generation of Optically Triggered-Magnetic Field Pulses for use in Pump-Probe Experiments.'
CLF Annual Report, pp. 127–129, 1997/1998.

[47] G.E. Ballentine, W.K. Hiebert *et al.*
'Ultrafast Microscopy and Numerical Simulation Study of Magnetisation Reversal Dynamics in Permalloy.'
Journal of Applied Physics, pp. 6830–6832, **87**(9), May 2000.

[48] L. He & W.D. Doyle
'A Theoretical Description of Magnetic Switching Experiments in Picosecond Field Pulses.'
Journal of Applied Physics, pp. 6489–6492, **79**(8), April 1996.

[49] G.P. Zhang & W. Hübner
'Femtosecond Spin Dynamics in the Time Domain.'
Journal of Applied Physics, pp. 5657–5660, **85**(8), April 1999.

[50] T.M. Crawford, P. Kabos & T.J. Silva
'Coherent Control of Precessional Dynamics in Thin Film Permalloy.'
Applied Physics Letters, pp. 2113–2115, **76**(15), April 2000.

Chapter 2

Experimental Apparatus and Samples

In this chapter the time domain Terahertz spectrometer (TDTS) is described. The initial description is given in terms of the operation of the TDTS with a co-planar stripline (CPS) transmitter and dipole antenna receiver. This has been done so that the operation of the TDTS is more easily understood, and because this configuration was used to optimise the system before the introduction of the InAs samples and the subsequent investigation of the generation of THz radiation by the illumination of InAs surfaces by femtosecond laser pulses. Use of the measurement system with the InAs samples is described later in Chapter 3.

Section 2.2 describes in detail the characteristics of the different InAs samples investigated and some of the non-standard semiconductor processing techniques that have been used during the course of this study.

2.1 Experimental System: The TDTS

THz frequency electromagnetic radiation was initially generated and detected with the use of a Time Domain Terahertz Spectrometer [1] shown in Figure 2.1. The TDTS in its entirety comprises two distinct parts: The first stage involves the production of ultrafast optical pulses and the second part is concerned with the generation and detection of the THz electromagnetic radiation.

2.1.1 Generation of Ultrashort Optical Pulses

At the heart of the system is a Spectra Physics 'Tsunami' titanium doped sapphire laser (Ti:sapphire). The Ti:sapphire laser is mode locked [2] and has a broad tuning range of 750-840 nm under the normal operating conditions outlined in this thesis, but a wider tuning range of 680 to 1100 nm is obtainable by changing the cavity mirrors. More importantly for the production of ultrafast optical pulses, the Ti:sapphire crystal has a large gain bandwidth product, which results in good relative intensities for the spectrum of frequencies required for use in this work. The Ti:sapphire is a self mode-locked laser and is capable of producing pulses of temporal width 70 fs at FWHM (full width half maximum) at a repetition rate of 82 MHz.

2.1.2 Mode-Locking

Mode-locking can be defined as the fundamental process of operation that induces all of the longitudinal modes of a laser cavity to oscillate with a fixed-phase

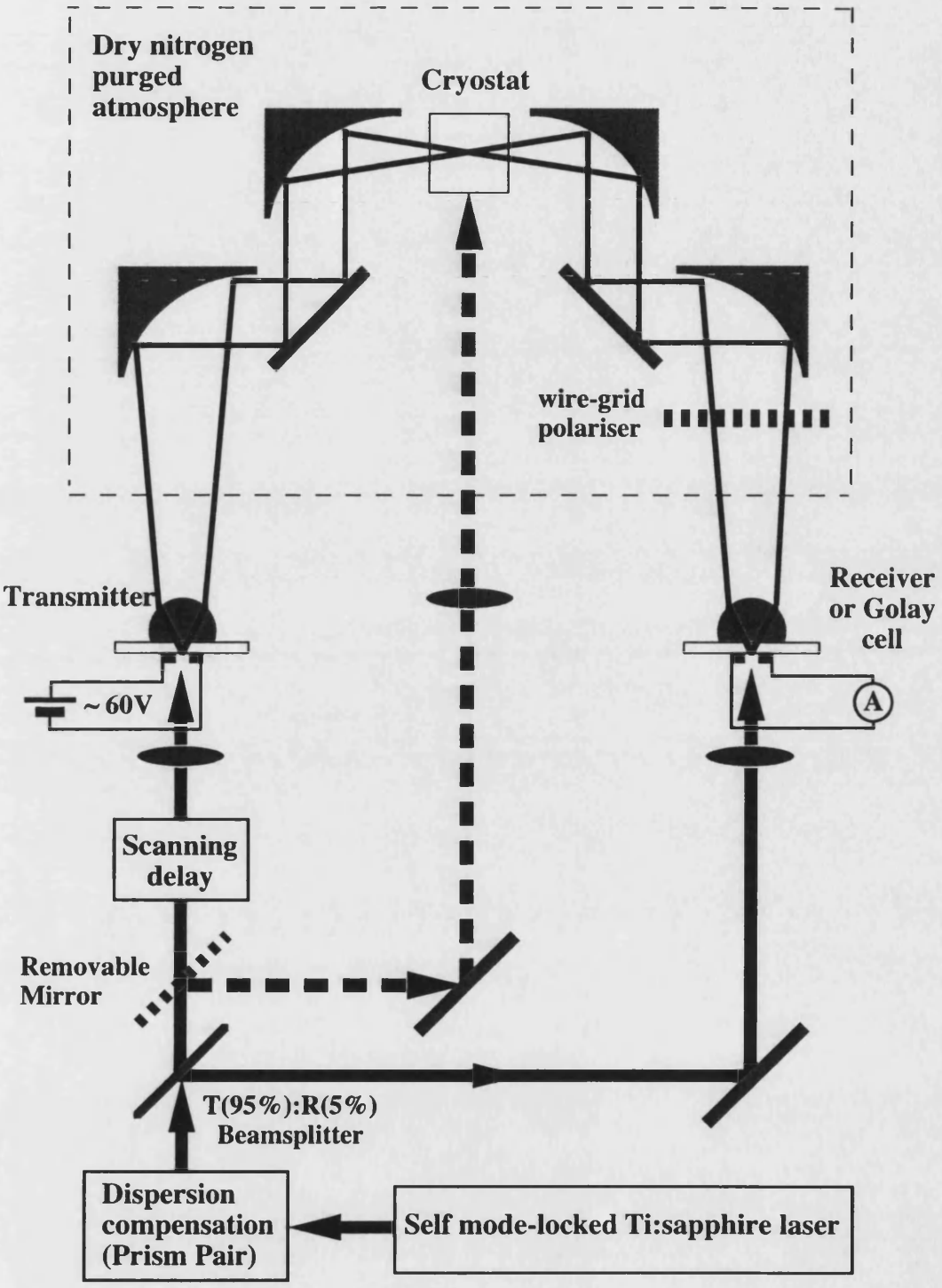

FIGURE 2.1: Schematic showing the time-domain terahertz spectrometer configured for use with the CPS transmitter and the dipole receiver.

relation (usually zero) between them [2]. In fact two distinct types of mode-locking exist, 'passive mode-locking' and 'active mode-locking', and the Tsunami Ti:sapphire uses both methods to generate the ultrashort pulses.

Passive mode-locking is observed in a Ti:sapphire laser in the form of self mode-locking, sometimes referred to as Kerr lens mode-locking, so that as the laser beam travels through the Ti:sapphire crystal it is subject to self-focusing due to the non-linear refractive index of the Ti:sapphire crystal itself [3] as is described below by Equation 2.1. Self-focusing is an induced lens effect and results from the distortion of the wavefront inflicted on the beam by itself whilst traversing the non-linear medium of refractive index n such that to the E^2 term,

$$n = n_0 + \Delta n(|E|^2) \tag{2.1}$$

where $\Delta n(|E|^2)$ is the optical field induced refractive index change; if Δn is positive, then the central, and necessarily more intense, part of the the beam will experience a larger refractive index and hence travel with a slower velocity than the less intense edge of the beam. Consequently, as the beam travels through the medium, the original wave is progressively distorted, and this distortion is similar to that imposed on the beam by a positive lens, hence the beam appears to focus by itself. A beam with a finite cross-section should also diffract, and only when the action of the self-focusing is stronger than the diffraction effect will the beam self-focus. Therefore, once the laser has begun mode-locking it will continue to do so (self-mode-locking).

As a crude explanation, self-focusing is proportional to $\Delta n(|E|^2)$, whilst diffraction is inversely proportional to the square of the beam radius, therefore as the beam radius shrinks on self-focusing, both the self-focusing and the diffraction

effects become stronger. If the increase of the latter action is more rapid than the former, then diffraction will overcome the self-focusing when the beam has reached some minimum cross-section. However, in many cases the field induced refractive index can be approximated by $\Delta n = n_2 |E^2|$, where n_2 is a constant. Then, because $|E|$ is inversely proportional to the beam radius, the self-focusing is always stronger than diffraction; if it is so initially. The beam may continue to self-focus until some other optical effect takes place and terminates the process. This self-focusing causes an amplitude modulation of the beam and this in turn incites a process known as saturable absorption in the crystal, which then helps to produce the pulses on the femtosecond scale. Pulse narrowing to the femtosecond scale takes place because the central intense portion of the pulse is able to saturate the absorber so that the loss in the cavity for this section of the pulse is less than the gain. Thus this portion experiences a nette gain whilst the wings of the pulse are attenuated by the absorber.

Active mode-locking in the Tsunami Ti:sapphire laser is achieved using an acousto-optic modulator (AOM) in the laser cavity. The AOM is driven by a low power r.f. source and serves to provide acoustic waves at a repetition frequency equal to the inverse of the round trip time of the cavity itself. The mode-locking is deemed active because a fraction of the beam is deflected onto a photodiode, which in turn detects changes in the laser output and a feedback loop is created by changing the r.f. frequency applied to the AOM.

Using these two methods, light pulses on the scale of ~ 70 fs can be produced by a Ti:sapphire laser. However, it is clear that as the laser beam is directed around a complex optical system, then the broad bandwidth pulses will be affected by the dispersive effects of the dielectric media present in the optical components.

These dielectric materials have a wavelength dependence which can be described by the Sellmeier equation [4],

$$n^2 = 1 + \frac{A\lambda^2}{\lambda^2 - \lambda_o^2} \tag{2.2}$$

Where A and λ_o are the Sellmeier coefficients and are material constants.

A temporally short light pulse exhibits a necessarily wide spectral bandwidth, and so the wavelength dependent index of refraction will cause the different spectral components to travel at different rates in the dielectric media. This is known as group velocity dispersion (GVD), and effectively means a spreading of the pulse in time. The group velocity of a pulse propagating in a dielectric medium can be expressed as,

$$\begin{aligned} \nu_g &= \frac{\mathrm{d}\omega}{\mathrm{d}k} \\ &= \nu_{ph} + \frac{k\mathrm{d}\nu_{ph}}{\mathrm{d}k} \end{aligned} \tag{2.3}$$

$$\nu_g = \frac{c}{n(\lambda)}\left(1 - \frac{\lambda}{n(\lambda)}\frac{\mathrm{d}n(\lambda)}{\mathrm{d}\lambda}\right) \tag{2.4}$$

which in turn shows a dispersion

$$\frac{\mathrm{d}\nu_g}{\mathrm{d}\omega} = \frac{\mathrm{d}\nu_g}{\mathrm{d}k} \Big/ \frac{\mathrm{d}\omega}{\mathrm{d}k} = \frac{1}{\nu_g}\frac{\mathrm{d}^2\omega}{\mathrm{d}k^2} \propto \frac{\mathrm{d}^2 n(\lambda)}{\mathrm{d}\lambda^2} \tag{2.5}$$

For $\mathrm{d}^2n(\lambda)/\mathrm{d}\lambda^2 \neq 0$ the velocity differs for the different frequency components. The case $\mathrm{d}^2n(\lambda)/\mathrm{d}\lambda^2 > 0$ is known as positive GVD (also referred to as positive chirp), the lower frequency components travel at a faster rate than the higher

frequency components, *i.e.* red leads blue; the reverse is known as negative GVD (negative chirp).

It can be shown then that an optical pulse of temporal width 70 fs, at FWHM, exiting the laser will not have the same duration at the end of the optical path. To overcome this problem, dispersion compensation is placed in the system as is shown in the schematic of the TDTS system in Figure 2.1.

2.1.3 Dispersion Compensation

Dispersion compensation can be achieved using a pair of prisms, fabricated from the material known as SF6. As was shown previously in Equation 2.2, by virtue of the wavelength dependence of the refractive index the refraction in the prisms causes the path length for the longer wavelengths to be greater. The pulse is initially refracted through the tip of the first prism and split spatially into its spectral components before being refracted through the tip of the second prism. The second prism directs the recollimated beam onto a mirror, which in turn reflects the light back through virtually the same path. With the differing path lengths for the different spectral components, the prism pair imparts a negative chirp on the pulse to compensate for the positive chirp that will be imparted by the remaining optics, and the prism pair itself. This is shown schematically in Figure 2.2,

A spectrum analyser was used when adjusting the laser for mode-locking to give a qualitative impression on the duration of the pulses. However, if a quantitative analysis of the pulse duration was sought then an autocorrelator was used.

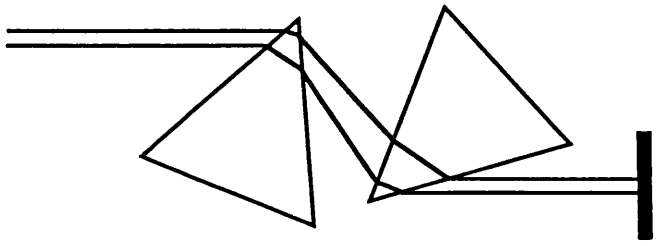

FIGURE 2.2: Schematic to show the arrangement of the prism pair to compensate for the group velocity dispersion in the optical system

The autocorrelation method relies on two principles. The first being the interaction of light pulses with a non-linear medium to give rise to second harmonic generation (SHG). The second being the production of relative time delays from the different path lengths experienced by the optical pulses incident on the non-linear medium. In this case, the non-linear medium used was a KDP (Potassium-Dihydrogen Phosphate) crystal in the co-linear arrangement, which is sometimes referred to as interferometric autocorrelation.

To measure the temporal width of the light pulse, the laser beam is split so that the two beams incident on the KDP crystal are of equal intensity. One of the beams is directed via a scanning delay line to enable the relative path lengths of the pulses to be changed. When the relative delay between the two co-incident beams is zero, then the beams are aligned spatially and temporally within the crystal. When this criterion is satisfied, and the phase matching condition is met, then the second harmonic pulse is generated as a function of the two incident optical pulses.

The autocorrelation signal is a measurement of the intensity of the generated second harmonic radiation, as a function of the relative delays between the two

co-incident optical beams. This is shown in Equation 2.6, where $E_o(t)$ is the envelope of the optical pulse of frequency ω, and $\phi(t)$ is the time-dependent phase. The autocorrelation signal is a measurement of the intensity of the second harmonic pulse, which is proportional to the square of the sum of the electric fields of the incident optical pulses.

$$\mathcal{I} \propto \int_{-\infty}^{\infty} |(E_o(t)e^{i(\omega t+\phi(t))} + E_o(t-\tau)e^{i(\omega(t-\tau)+\phi(t-\tau))})^2|^2 \mathrm{d}t \qquad (2.6)$$

The shape of the light pulses produced by the Ti:sapphire laser is generally assumed to have a sech^2 profile, and according to Sala *et al.* [5], if the measured signal is of the form $\mathcal{I} = \mathrm{sech}^2(t/T)$, then the pulse width $\Delta t'$ is related to the real pulse width Δt by the ratio,

$$\frac{\Delta t}{\Delta t'} = 0.6482 \qquad (2.7)$$

where $\Delta t'$ is the full width at half maximum (FWHM) of the autocorrelation envelope.

2.1.4 Generation and Coherent Detection of THz Transients

To further assist in the understanding of the TDTS, a brief description of the transmitting and receiving antennae is given in the following sections. To ensure that the TDTS is optimised and performing consistently between experiments, the system is always initially tested using the CPS transmitter as the THz radiation source. Two distinctly different methods were used to detect the THz

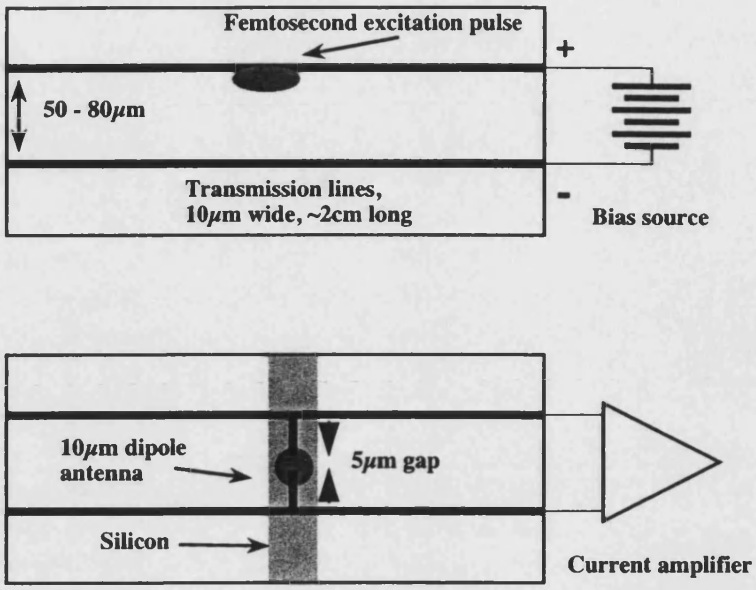

FIGURE 2.3: Schematic showing the CPS transmitter (top) and dipole receiver (bottom) structures

radiation, coherent and non-coherent detection, which are described later in more detail. The coherent detection was achieved by use of the dipole receiver, two different devices having been used, one fabricated on silicon on oxide on silicon, the other was a new generation of dipole receiver fabricated on oxygen ion implanted GaAs. The second, non-coherent, detection technique involved the use of a bolometer called a Golay cell, which was used to determine the absolute average radiated power. The structures of the transmitter and receiver are shown in Figure 2.3

Coplanar Stripline Transmitter

The transmitter consists of a photoconducting coplanar stripline (CPS) structure as shown in Figure 2.3, fabricated by the thermal evaporation of a 10 nm titanium layer followed by a ≥ 150 nm gold layer (Ti:Au) onto a SI-GaAs (semi-insulating

gallium arsenide) substrate. The stripline geometry consists of a pair of 25 mm long 10 μm wide strips, separated by a gap of 50 μm. The high resistivity ($\varrho > 10^7\,\Omega\,\mathrm{cm}$) of SI-GaAs allows a bias voltage of $\sim 60\,\mathrm{V}$ to be applied between the stripline tracks. This design of transmitter was found by Katzenellenbogen and Grischkowsky [6] to radiate faster and more powerfully than the original devices constructed on silicon by Auston [7]. The Ti:sapphire laser output is focused via a plano-convex cylindrical lens placed in front of a $\times$ 20 microscope objective lens resulting in a focal region of $\sim 100\,\mu\mathrm{m} \times 5\mu\mathrm{m}$. It was found that focusing the excitation beam close to the anode of the CPS transmitter lead to a stronger THz emission. This can be partly attributed to a geometrical enhancement of the electrostatic field, and the presence of traps in SI-GaAs[8] and the different mobilities of electrons and holes[9]. In fact modelling of a similar structure [8] has indicated that when biased above the Ohmic regime, the applied potential is dropped within $\sim 5\,\mu\mathrm{m}$ of the anode, with the field increasing by about an order of magnitude in the last $1\,\mu\mathrm{m}$.

The typical average power used to illuminate the transmitter is $\sim 30\,\mathrm{mW}$, beyond which the radiated THz amplitude begins to saturate and there is an increased risk of device damage. The incident photon energy, typically 1.64 eV, is greater in energy than the band gap of GaAs ($\mathrm{E}_{g(\mathrm{GaAs})} = 1.42\,\mathrm{eV}$), hence the incident radiation creates electron-hole pairs within the illuminated area, and within a few microns of the surface. These electron-hole pairs then accelerate until they reach drift velocity. Cumulative screening effects do not pose a problem as the carriers recombine or travel the whole length of the track separation on a time scale shorter than the Ti:sapphire repetition period, $\sim 10\,\mathrm{ns}$ [10].

From Maxwell's equations, the transient current, $j(t)$, that is created at the

surface has an associated transient electric field as described by Equation 2.9, where $N(t)$ is the number of carriers, $v(t)$ is the average velocity and e is the charge on the electron.

$$E(t) \propto \frac{\mathrm{d}j(t)}{\mathrm{d}t} = \frac{\mathrm{d}N(t)}{\mathrm{d}t} e\nu(t) + N(t)e\frac{\mathrm{d}\nu(t)}{\mathrm{d}t} \tag{2.8}$$

During the time of illumination, this equation is dominated by the $\mathrm{d}N/\mathrm{d}t$ term, which is the displacement current term. Post illumination, the photogenerated carriers continue to accelerate in the applied field until they reach drift velocity or the field is screened by the spatial separation of the electrons and holes. Using such a model, Keiding *et al.* [11] have successfully reproduced the qualitative shapes of THz transients from biased coplanar striplines. Due to the mismatch of the refractive indices of GaAs and air and the direction of acceleration, most of the THz radiation that is generated is preferentially emitted into the GaAs substrate [11], which is transparent at these low THz frequencies. At the back surface of the GaAs substrate, the THz radiation is subsequently collected and partially collimated by a high resistivity hyper-hemispherical silicon lens, which is separated from the back of the GaAs substrate by a thin layer of paraffin oil to reduce losses by reflection at the interface. The silicon lens is not in a fixed position but is held in place by a spring and can be freely translated over the surface of the GaAs substrate by the use of micrometers; the presence of the paraffin oil also assisting in this. The hyper-hemispherical lens and the subsequent THz optics required to collect and steer the THz beam are described in more detail in §2.1.6

The Dipole Receiver

The structure of the receiver is shown in Figure 2.3. Two types of receiver were used in the course of this work, the first was the SiOSi (silicon on oxide on silicon) receiver, the other being of similar electrode design, but on a substrate of oxygen ion implanted GaAs.

The SiOSi receiver consists of a 1·05 μm polycrystalline silicon layer grown by chemical vapour deposition on a thermally grown 0·6 μm thick silicon dioxide (SiO_2) layer, itself grown on a high resistivity ($\varrho > 1{\cdot}4\,k\Omega cm$), 1 mm thick, $\langle 111 \rangle$ silicon substrate. The silicon epilayer is then ion implanted to increase the carrier trapping rate [12] by increasing the defect density — thus achieving a very short carrier lifetime. The carrier lifetime was measured by time dependent reflectivity, and for an oxygen ion irradiation dose of $10^{15}\,cm^{-2}$, the lifetime was found to be 550±50 fs [1].

On this ion damaged Si epilayer, a pair of Ti:Au tracks was deposited by thermal evaporation, to form the structure shown in Figure 2.3. No annealing of these tracks is required as the ion implantation results in a good ohmic contact to the epilayer because of the presence of defect states created by the ion implantation. At the centre of each track an antenna stub extends towards the opposing track to form a 5 μm gap. The silicon not directly surrounding this region, was removed by reactive ion etching in a SF_6:O_2 plasma [10]. This process is undertaken to reduce the Johnson noise of the receiver by minimising the inter-track resistance [10]. Finally, an anti-reflection coating of a $\lambda/4$ layer of SiO_2 was sputtered on to the surface to maximise the gating power, and to provide a little protection for the device.

The method of fabrication of the antenna structure on the GaAs substrate is the same as that described above for the SOS device.

The receiver gating beam is focused to a $\sim 5\,\mu$m spot in the centre of the gap between the receiver stubs, and the laser power is limited to $\sim 20\,$mW to avoid thermal damage to the receiver [11]. The $5\,\mu$m gap between the antenna stubs presents an impedance of $100\,$kΩ in the absence of the gating beam, but reduces to a resistance of the order of $0{\cdot}1\,\Omega$ when illuminated. Hence when the electric field transient is temporally and spatially co-incident with the optical gating beam at the receiver, then a current flows that is proportional to the amplitude of the instantaneous field. A low noise current amplifier with a bandwidth of $8\,$kHz at a gain of $10^8\,$V/A then converts this current to a voltage. The important point to note here is that the current that is detected in the receiver is directly proportional to the amplitude of the instantaneous THz electric field, so that phase information about the transient is obtained. This is why the detection technique is coherent.

The current and therefore the electric field of the transient is measured as a function of the relative delay between the source and receiver exciting pulses, and thus the transient is resolved temporally on a sub-picosecond time scale with a rapidly scanned delay line and can be observed in real time on an oscilloscope. The relative delay can be varied up to a maximum of $150\,$ps at frequencies up to $10\,$Hz by the use of a rapid scanning delay line (rapid SDL). Typically 200 full scans of the THz transient were performed, thus improving the signal to noise ratio (SNR) by a factor of 14, if the noise is assumed to be random. The carrier lifetime has been measured [1] to be $\sim 550\,$fs, and it is this lifetime that acts as one of the limitations of the system.

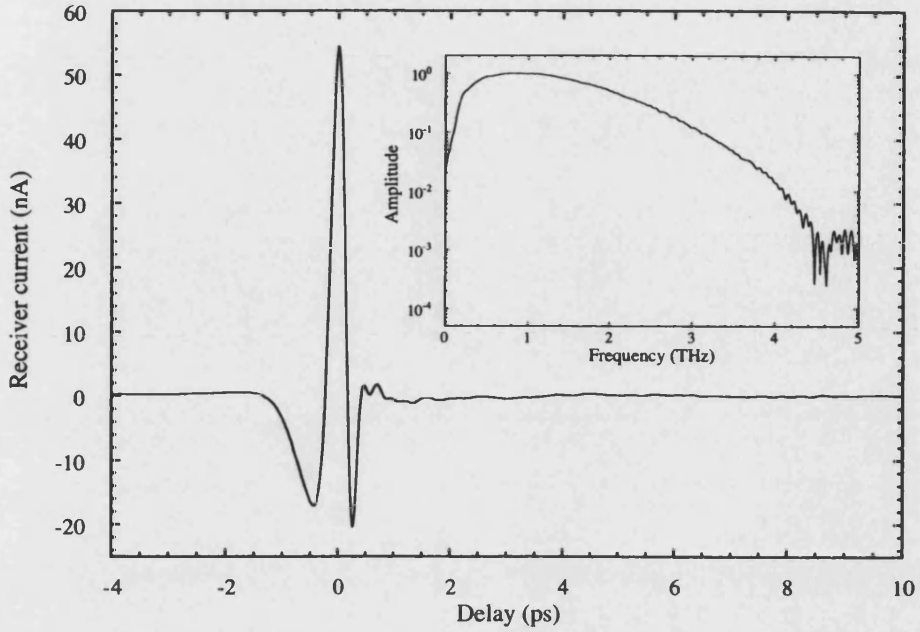

FIGURE 2.4: THz transient emitted by line focus excitation of GaAs CPS transmitter and detected by a 10 μm dipole receiver. The inset shows the associated frequency spectrum of the transient, obtained by performing a FFT.

A critical factor to take into account when using any receiver is the noise level. In the absence of laser illumination, the SiOSi device exhibits noise of 10 fA $/\sqrt{\text{Hz}}$ in the region 100 Hz to 10 kHz, compares with the illuminated receiver noise level of $\sim$100 fA $/\sqrt{\text{Hz}}$. The 'dark noise' is dominated by thermal (Johnson) noise; however, when illuminated it is the laser noise that dominates.

The 'sensitivity' of the receiver can be determined by replacing it with a bolometer and measuring the power, which is proportional to the square of the current in the receiver. In this way a value for the sensitivity of the SiOSi receiver was determined to be 10 μA W$^{-1/2}$; a factor of two error is estimated in this value due to the accuracy of the calibration of the bolometer. This value is in agreement with the estimate of van Exter and Grischkowsky [10] of 15 μA W$^{-1/2}$, despite the

use of different THz optics and receiver design.

Figure 2.4 shows a THz transient emitted from a GaAs CPS transmitter, detected with the 10 μm SiOSi dipole receiver. This result shows a typical pulse shape, although the overall detected amplitude is much larger than normally used, due to the increase in the excitation power to 170 mW.

2.1.5 The Golay Cell

As well as using the dipole receiver to detect the amplitude of the electric field transient, a Golay cell, a room temperature bolometer, was used to detect the absolute power emitted by the InAs. The dipole antenna receiver was replaced by the Golay cell, whilst ensuring that the aperture of the Golay cell was positioned to be as close as possible to the original position of the silicon lens. The aperture of the Golay cell is a 3·5 mm diameter diamond window, whereas the high resistivity silicon lens has a radius 4·75 mm. The large detection bandwidth of the Golay cell is due to the fact that it measures the absorption of radiation by an absorber which in turn heats a gas in a closed capsule. The rise in pressure causes an expansion of a flexible membrane upon which a mirror is situated, see Figure 2.5. The displacement of this mirror due to the expansion of the gas is monitored by observing the deflection of a reference light beam.

The Golay cell was carefully calibrated by use of a filtered black body source [13], a CO_2 laser [14] and a HeNe laser. The Golay cell detects the input power, not the electric field of incident electromagnetic radiation. Thus to eliminate background radiation noise, the calibration beam, and the optical pump beam in the experiments, was modulated. The Golay cell has a very low temporal

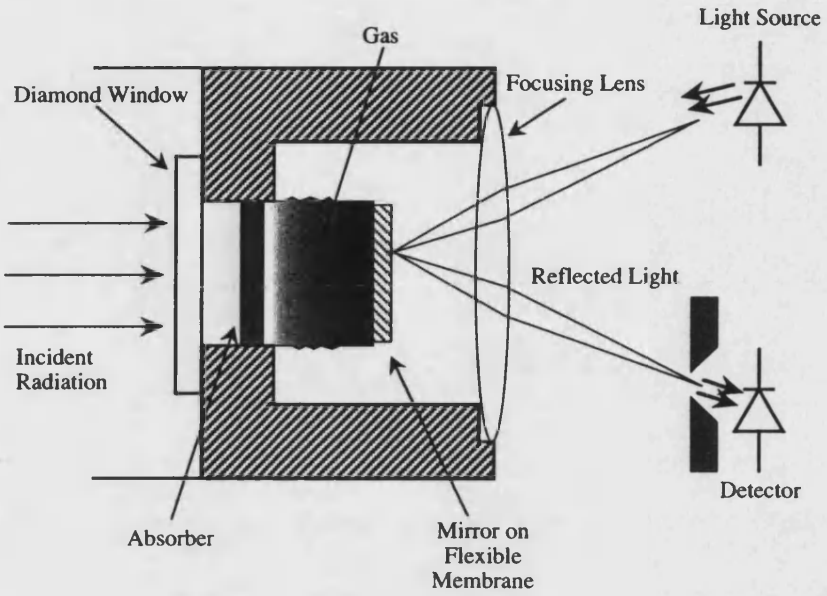

FIGURE 2.5: Schematic showing the internal components of a typical Golay cell.

resolution, the bandwidth is 20 Hz, and so a modulation frequency of 19 Hz was used. The sensitivity found when using the black body source, was found to be $12\,\mathrm{kV\,W^{-1}}$, which was also the result found when the calibration using the HeNe laser was performed. In the case of the CO_2 laser calibration, the beam width of the CO_2 laser was found to be larger than the diameter of the aperture of the Golay cell, and so the Golay cell was scanned across the beam in the horizontal plane at several vertical positions. By de-convolving the beam profile with the Golay cell aperture, the fraction of the laser beam that entered the cell was obtained, the sensitivity was subsequently found to be $9\,\mathrm{kV\,W^{-1}}$.

As well as the calibration factor for the Golay cell, some of the THz radiation emitted by the InAs samples is lost due to the cryostat windows and a filter covering the aperture of the Golay cell. By using the CPS transmitter, the loss due to

the cryostat has been measured, and the transmission of the windows calculated to be 50% for the THz frequencies studied. The collection efficiency of the Golay cell has been calculated to be 20% and the transmission coefficient of the filter for these frequencies has been measured to be 88%. Hence an overall calibration factor of 1·056 mV/μW is used to determine the absolute power detected by the Golay cell.

2.1.6 The THz Optics

As the THz radiation from a source excited by a small optical excitation beam will necessarily be strongly divergent, there is a need to collect and focus the radiation from the transmitter or InAs sample — and similarly focus the THz onto the antenna stubs of the receiver. To this end, there is a hyper-hemispherical high resistivity silicon lens mounted on the backside of the transmitter and receiver. High resistivity silicon was chosen due to its low dispersion and absorption in the relevant part of the electromagnetic spectrum [15], although for the transmitter, there is a slight refractive index mismatch at the GaAs/Si interface.

The lens design is such that, when ignoring diffraction effects, the radiation from the transmitter is focused when the antenna is located at a distance H from the tip of the lens, where H is given by,

$$H = \frac{Rn}{n-1} \tag{2.9}$$

where n is the refractive index of silicon, and $R = 4.75\,\text{mm}$ the radius of the lens. Any radiation at incident angles larger than 17° to the lens-air interface surface

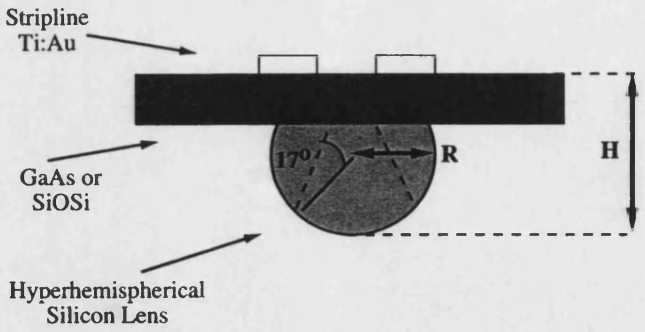

FIGURE 2.6: The hyper-hemispherical high resistivity silicon lens structure, as mounted on the reverse of the CPS transmitter and dipole receiver.

normal are lost due to total internal reflection,this angle therefore determines the width of the THz exit pupil [15].

Upon exiting the silicon lens, the THz beam converges to a point ~30 mm from the the lens and approximately 115 mm in front of the first off-axis parabolic mirror (OAPM), in the focal plane. The beam is then directed through a wire grid polariser, with an extinction ratio of 1:10, to select the p-polarised component. A second OAPM of focal length 250 mm, is present and displaced from the first by the sum of their focal lengths to ensure that all the frequency components are focused as well as possible at the same point [11]. The THz beam is then focused to a spot of ~6 mm at FWHM (Full Width Half Maximum), at the centre of the cryostat sample space. The far infra-red (FIR) cold windows which separate the helium cooled sample space from the outer vacuum jacket are made from high resistivity silicon to minimise absorption and dispersion of the THz transients. the silicon windows are 2 mm thick and thus any reflections from the interfaces are delayed by ~46 ps relative to the main transient. Sealing the vacuum chamber are windows made from 32 μm thick Mylar which has a lower refractive index than silicon, and thus the loss of the THz radiation by reflection is a smaller effect than in silicon. A similar set of optics on the exit of the cryostat guides

the THz beam to the dipole receiver.

To optimise the receiver sensitivity and bandwidth, the silicon lens situated on the back of the receiver is manouevered across the surface to change the coupling of the THz radiation into the receiver; the position of the incident optical excitation beam on the dipole is also changed. The SNR and bandwidth is critically dependent on both of these actions.

To perform experiments using the InAs samples as the source for the THz radiation, the transmitter pump beam was redirected through optical access windows of the cryostat via a focusing lens of focal length 25 cm such that the spot size at the sample surface, 27 cm away, was $1{\cdot}2\,\mathrm{mm}^2$. Access to the sample space is via a pair of fused silica windows situated at the front of the cryostat. To enable the emitted radiation to be collected and measured, the sample is oriented such that the surface is at 45° to both the input optical windows, and the exit windows in most experiments. In some experiments, however, a specially designed attachment was used that allowed the sample to be placed with the surface normal parallel or perpendicular to the magnetic field, whilst still retaining the 45° angle to the incident light. This attachment is shown in plan view for the different geometries in Figure 2.7.

As well as observing reflections from the optics as mentioned above, reflections are observed from the back surface of the more transparent samples. The reflections are typically seen about 10 ps after the main transient for samples of thickness $\sim$500 μm. To counter this problem, a thick substrate of equal refractive index to the test sample was occasionally contacted to the back surface of the sample, by the use of paraffin oil. The metal sample holder itself was modified to eliminate reflections by drilling a $\sim$1 cm hole, over which the samples were mounted.

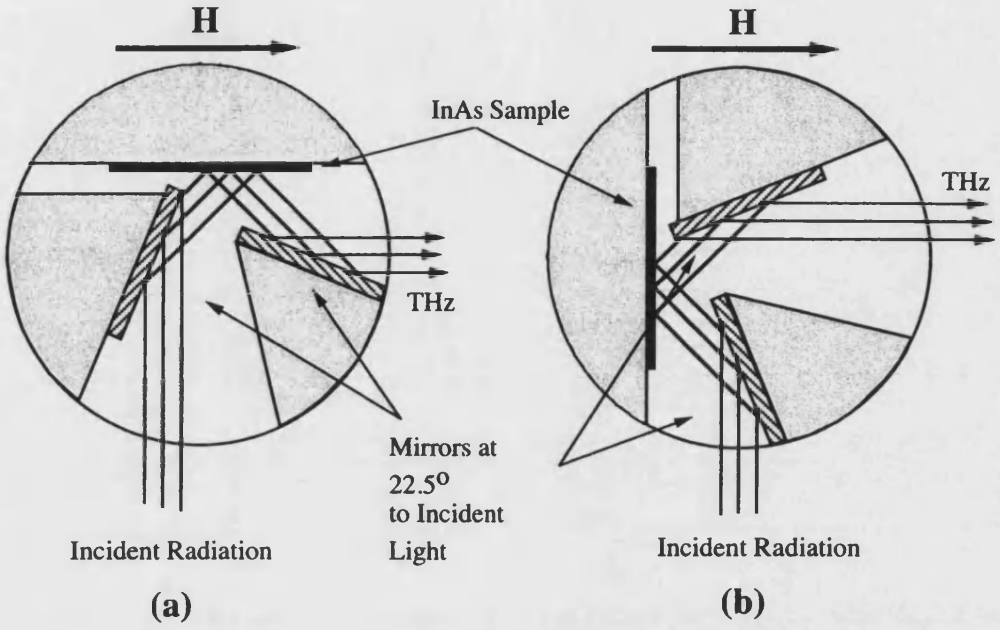

FIGURE 2.7: The sample stick attachment to allow the THz emission to be measured with the electric field and applied magnetic field **(a)** perpendicular or **(b)** parallel to one another.

2.2 Samples

The InAs samples investigated were both n- and p-type and covered a large range of carrier concentrations. The majority of the samples that have been examined in this study were grown by molecular beam epitaxy (MBE) at Imperial College [16]. These samples all have a sample designation beginning with IC and have SI-GaAs substrates, and are of varying epilayer thicknesses, as is shown in Table 2.1. The carrier concentration and mobilities were determined by the Hall measurement technique, and the measured values confirmed by far infra-red photoconductivity measurements. The difficulty in measuring the characteristics of bulk charge carriers has been discussed [17], in terms of the surface accumulation layer that exists in InAs.

Sample	Majority Carrier	Carrier Density	Sample Thickness
IC106	electron	$1{\cdot}7\times10^{15}\,\mathrm{cm}^{-3}$	4 μm epilayer
BK1	electron	$2{\cdot}0\times10^{16}\,\mathrm{cm}^{-3}$	bulk sample
IC196	electron	$1{\cdot}9\times10^{16}\,\mathrm{cm}^{-3}$	4 μm epilayer
IC311	electron	$1{\cdot}0\times10^{17}\,\mathrm{cm}^{-3}$	5 μm epilayer
IC301	electron	$7{\cdot}5\times10^{17}\,\mathrm{cm}^{-3}$	4 μm epilayer
IC317	electron	$5{\cdot}0\times10^{18}\,\mathrm{cm}^{-3}$	5 μm epilayer
IC127	electron	$4{\cdot}0\times10^{19}\,\mathrm{cm}^{-3}$	5 μm epilayer
DRA-18	hole	$5{\cdot}0\times10^{18}\,\mathrm{cm}^{-3}$	bulk sample
IC233	hole	$5{\cdot}5\times10^{18}\,\mathrm{cm}^{-3}$	5 μm epilayer
IAS1064	hole	$2{\cdot}0\times10^{17}\,\mathrm{cm}^{-3}$	5 μm epilayer
C1721	electron	$3{\cdot}0\times10^{17}\,\mathrm{cm}^{-3}$	$\sim$7000 Å epilayer
RMB1154	SI-GaAs	$\sim10^{14}\,\mathrm{cm}^{-3}$	*p-i-n* structure

TABLE 2.1: Sample descriptions and characteristics.

The sample C1721 was grown by MBE by E.H. Linfield at The Cavendish Laboratory, Cambridge University. The structure of this sample is discussed further in § 2.2.1

2.2.1 ELO Technique

The epitaxial lift-off (ELO) technique consists of cleaving a small chip (approximately 5 mm×5 mm) of the wafer and subsequently cleaning it using the standard process of consecutive immersions in trichloroethane, acetone and isopropylalcohol (IPA). The chip was then placed on a hot plate and heated up to a temperature of 125°C; upon reaching the required temperature, the surface was covered, as much as possible, by ApiezonW black wax. This wax has a melting point of approximately 120°C and slowly deforms to form a smooth 'dome' structure

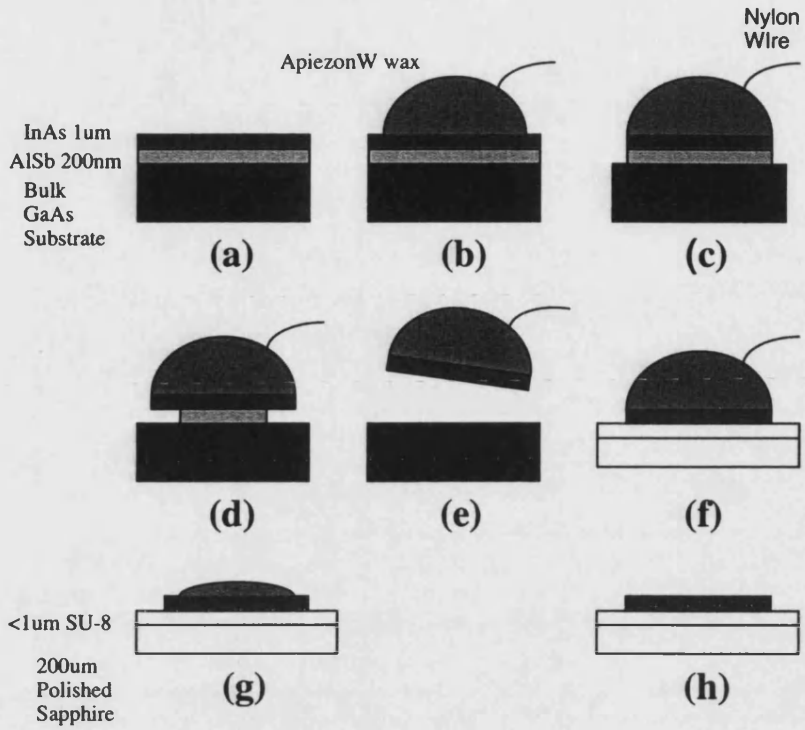

FIGURE 2.8: Sequential graphic showing the process steps involved in making an epitaxial lift-off structure. **(a)** The epitaxial lift-off sample; **(b)** the deposition of the wax and nylon handling wire; **(c)** etch of the epilayer to expose clean AlSb surface; **(d)** undercut of InAs by etching of AlAs in 10% HF; **(e)** lift-off of epilayer and wax; **(f)** positioning of the epilayer onto the host substrate, pre-spun with SU8–5; **(g)** immersion in chloroform to remove wax; **(h)** final sample.

as shown in Figure 2.8. A short piece of nylon wire ($\sim$ 5 mm) was deposited onto the wax to allow easy handling of the epilayer once it had lifted-off the substrate. The black wax was then allowed to cool — in so doing the surface of the wax cools at a different rate than the interior, resulting in the formation of a relatively large surface tension. The dilute HF solution preferentially etches the AlAs 'sacrificial layer' whilst the surface tension in the wax provides enough tension to help prevent the epilayer from binding to the GaAs substrate by van der Waals' bonding or otherwise. In effect the wax 'peels' the epilayer away from the substrate as the sacrificial layer is etched away. Prior to immersing the structure in the selective HF etch, so as to expose a clean, and hence a more readily

etched surface of AlAs, the sample was immersed in an agitated non-selective etch solution of composition $HCl:H_2O_2:H_2O$ in the ratio 1:12:48 (by volume) for 10–15 minutes at 20°C. The sample was subsequently rinsed in de-ionised (DI) water and immersed in the selective etch solution $HF:H_2O$:3M-1, at 20°C, in the ratio 20:179:1 (by volume), until the epilayer had lifted off. The anti-foaming agent (3M-1) is present in the solution so as to prevent the etch products from forming gas bubbles. This is an important issue [18] because the formation of gas bubbles slows the etch rate by preventing fresh etchant from gaining access to the exposed AlAs surface in the 'etch channel'; and in fact the pressure caused by the formation of bubbles can be sufficient to crack the epilayer during lift-off [19], thus rendering it useless. The etch takes approximately 8–10 hours, but can be accelerated by an order of magnitude [20] by lowering the temperature of the etch solution towards 0°C, which also helps to prevent the formation of gas bubbles in the 'etch channel'.

Once the epilayer has lifted-off from the substrate, then the epilayer and wax structure can be manipulated by using a set of tweezers to grasp the nylon wire. Rather than remove the sample from the etchant and allow the dust particles resting, under surface tension, at the surface of the liquid, to deposit themselves on the freshly exposed InAs surface; the sample is manipulated into a polytetrafluoroethalene (PTFE) 'basket' and lifted out of the solution, whilst still under liquid. By removing the sample in this manner, and immersing in DI water, the sample is never exposed to atmosphere, and never has to cross the surface of a liquid and be exposed to the dust particles held there.

The sample is then manouevered onto a sapphire substrate [21] that has had a thin, $\leq 1\,\mu$m, layer of SU–8 [22] photoresist spun onto it. SU–8 is a positive

photoresist and so when it is exposed to ultraviolet light the chemical composition is changed such that if it is baked at over 100°C then it forms a hard film. By spinning the SU–8 on to the sample at > 6500 r. p. m. a thin film of SU–8 of less than $1\,\mu$m in thickness is achievable.

A PTFE press, imparting a pressure of 1.5 dynes per square millimeter, is lowered onto the waxed surface of the epilayer as the water is drained away. With the press still in place, the sample is then allowed to dry and any remaining water left to evaporate. The capillary action of the water leaving the space between the host-substrate and epilayer also helps to form a good contact between the host-substrate and the epilayer, by applying a force opposite in direction to the tension provided by the wax [23].

Once the sample is free of water, the press is carefully removed and the sample is exposed to intense UV-light. Thus the SU–8 positive photoresist is chemically altered and after a short bake at approximately 60° C, to remove the solvents from the now exposed photoresist, the epilayer is firmly bonded to the host-substrate.

ApiezonW wax is soluble in chloroform — whereas the exposed SU–8 is not — and thus the whole sample is immersed in warm, 55° C, chloroform until the wax has been completely dissolved, leaving a clean surface of InAs.

The C1720 material was processed by this method to provide a sample of sufficiently small thickness that a transmission measurement at a wavelength of 765 nm could be made as discussed later Chapter 3.

References

[1] J.A. Cluff
'Time Domain Terahertz Spectroscopy.'
PhD. Thesis, University of Bath, February 2000.

[2] William M. Robertson
'Optoelectronic Techniques for Microwave and Millimeter-Wave Engineering.'
1995 Artech House Inc., Ma. USA.
ISBN: 0890067112

[3] Y.R. Shen
'The Principles of Non-Linear Optics.'
John Wiley & Sons, NY, 1984.
ISBN: 04718899989

[4] M. Born & E. Wolf
'Principles of Optics.'
Pergamon Press, Oxford, 6^{th} Edition, 1986

[5] K.L. Sala, G.A. Kenney-Wallace *et al.*
'CW Autocorrelation Measurements of Picosecond Laser Pulses.'
IEEE Journal of Quantum Electronics, pp. 990-996 **QE-16**(9), Sept. 1980

[6] N. Katzenellenbogen & D. Grischkowsky
'Efficient Generation of 380 fsec Pulses of THz Radiation by Ultrafast Laser Pulse Excitation of a Biased Metal Semiconductor Interface.'
Applied Physics Letters, pp. 222–, **58**, 1991.

[7] D.H. Auston, K.P. Cheung & P.R. Smith
'Picosecond Photoconducting Hertzian Dipole.'
Applied Physics Letters, pp. 284–286, **45**(3), August 1984

[8] S.E. Ralph & D. Grischkowsky
'Trap Enhanced Electric Fields in Semi-Insulators: The Role of Electrical

and Optical Carrier Injection.'
Applied Physics Letters, pp. 1972, **59**, 1991.

[9] U.D. Keil, D.R. Dykaar *et al.*
'Reflectivity Measurements of Femtosecond Carrier and Field Dynamics in Semiconductors.'
Applied Physics Letters, pp. 3267–3269, **64**, 1994.

[10] M. van Exter & D.R. Grischkowsky
'Characterisation of an Optoelectronic THz Beam System.'
IEEE Transactions on Microwave Theory Technology, pp.1684–1691, **38**(11), Nov. 1990.

[11] P. Uhd-Jepsen, R.H. Jacobsen *et al.*
'Generation and Detection of THz pulses from Biased Semiconducting Antennas.'
Journal of the Optical Society of America B — Optical Physics, pp.2424–2436, **B 13**(11), Nov. 1996.

[12] F.E. Donay, D. Grischkowsky *et al.*
'Carrier Lifetime Versus Ion-Implantation Dose in Silicon-on-Sapphire.'
Applied Physics Letters, pp. 460–462, **50**(8), Feb. 1987.

[13] The calibration of the Golay took place at QMC Instruments is London, with a standard commercially available black body source.

[14] The calibration of the Golay cell with the CO_2 laser took place at the Toshiba Cambridge Research Centre (TCRC).

[15] Ch. Fattinger & D. Grischkowsky
'Terahertz Beams.'
Applied Physics Letters, pp. 490–492, **54**, 1989.

[16] P.D. Wang, S.N. Holmes *et al.*
'Electrical and Magneto-Optical Studies of MBE InAs on GaAs.'
Semiconductor Science and Technology, pp. 767–786, **7**, 1992.

[17] Y.J. Jung, B.H. Kim & H.J. Lee
'Electrical Transport and Energy-Band Structure in InAs.'
Physical Review B, pp. 3151–3164, **26**(6), Sept. 1982.

[18] Y. Sasaki, T. Katayama *et al.*
'High-Speed GaAs Epitaxial Lift-Off and Bonding with High Alignment Accuracy Using a Sapphire Plate.'
Journal of the Electrochemical Society, pp. 710–712, **146**(2), 1999.

[19] P. Demeester, I. Pollentier *et al.*
'Epitaxial Lift-Off and its Applications.'
Semiconductor Science and Technology, pp. 1124–1135, **8**, 1993.

[20] J-I. Maeda, Y. Sasaki *et al.*
'High-Rate GaAs Epitaxial Lift-Off Technique for Optoelectronic Integrated Circuits.'
Japanese Journal of Applied Physics, pp. 1554–1557, **36, 1**(3B), Mar 1997.

[21] H.-M. Heiliger, M. Vossebürger *et al.*
'Application of Liftoff Low-Temperature-Grown GaAs on Transparent Substrates for THz Signal Generation.'
Applied Physics Letters, pp. 2903–2905, **69**(19), 4^{th} Nov. 1996.

[22] S. Arscott, L. Duvillaret *et al.*
'Micromachining Techniques at Terahertz Frequencies.'
Proceedings of the EUROPTO Conference on Terahertz Spectroscopy and Applications II, pp. 335–341.

[23] E. Yablonovitch & T. Gmitter
'Wetting Angle and Surface Tension in the Crystallization of Thin Liquid Films.'
Journal of the Electrochemical Society : Solid-State Science and Technology, pp. 2625–2630, **131**(11), Nov. 1984.

[24] Wolfgang Demtröder
'Laser Spectroscopy — Basic Concepts and Instrumentation (2^{nd} Enlarged Edition).'
Springer-Verlag, Berlin.
ISBN: 3–540–57171–X

[25] C.F. Klingshirn
'Semiconductor Optics.'
Springer-Verlag, Berlin.
ISBN: 3–540–58312–2

[26] E. Yablonovitch, T. Gmitter *et al.*
'Extreme Selectivity in the Lift-Off of Epitaxial GaAs Films.'
Applied Physics Letters, pp. 2222–2224, **51**(26), 28^{th} Dec. 1987.

[27] E. Yablonovitch, T. Gmitter *et al.*
'Van der Waals' Bonding of GaAs Epitaxial Liftoff Films onto Arbitrary Substrates.'
Applied Physics Letters, pp. 2419–2421, **56**(24), 11^{th} June 1990.

[28] J. Fastenau, E. Özbay *et al.*
'Epitaxial Lift-Off of Thin InAs Layers.'
Journal of Electronic Materials, pp. 757–760, **24**(6), 1995.

Chapter 3

THz Emission from InAs

Zhang *et al.* reported the first observation of the generation of optically induced ultrafast electromagnetic radiation with terahertz bandwidth, from bare semiconductor surfaces and interfaces [1, 2]. A large selection of bulk, epitaxial and superlattice samples from III-V, II-VI and group-IV semiconductors were then investigated [3], but not InAs. The largest average powers were found to be generated in materials that have surface regions of high electric field due to the pinning of the Fermi level by mid-gap surface states, which gives rise to surface accumulation or depletion layers. The illumination of these semiconductor surfaces by femtosecond optical pulses excites transient photocurrents [3] which can result in the emission of THz radiation. Additionally, by the illumination of some semiconductors surfaces with high power optical beams, optical rectification can result in the emission of THz radiation. The effect of the application of magnetic and electric fields on the emission of the THz electromagnetic radiation from GaAs *p-i-n* structures was subsequently reported by Zhang *et al.* [4, 5]. It was shown that by the application of a magnetic field, the polarity of the transient could be

switched by changing the polarity of the magnetic field, and that the emission could be enhanced. The geometry of the experiment was such that the optical pulse was normal to the surface of the samples and the emitted THz radiation was measured by a detector mounted along this axis behind the sample. The enhancement of the emission was found to depend on the magnetic field strength and was found to be linear for applied fields less than 0·1 T and super linear for stronger fields up to the maximum observed field of ~0·5 T.

Recent reports of the generation of high average power THz radiation from InAs surfaces subject to large magnetic fields and excited by near infrared radiation have generated a lot of interest. Initially, Sarukura *et al.* [6, 7] claimed to have measured, by a bolometric technique, 650 μW average power THz radiation from an undoped ($2\times10^{16}\,cm^{-3}$) bulk InAs sample at room temperature and 1·7 T, by excitation with 1·5 W average power near infrared radiation. A separate report by M^{c}Laughlin *et al.* [8] claimed to have measured, also by a bolometric technique, a lower average power of only 12 μW from a similar InAs sample at 8 T and 170 K with an average near infrared excitation power of 0·14 W. In both these reports, the frequency spectrum of the emitted THz radiation was also measured, but was contaminated by absorption due to water vapour; Sarukura *et al.* having used a polarising Michelson interferometer and M^{c}Laughlin *et al.* an electro-optic sampling technique (EOS). The bandwidth of the technique used by Sarukura *et al.* was larger than that of the EOS technique used by M^{c}Laughlin *et al.*, but the bandwidth of the emission was observed to be about the same.

Meinart *et al.* [9] proposed a theory for the THz emission from optically excited semiconductors in crossed electric and magnetic fields in terms of Bloch equations. However, the model did not predict the enhancement of the emission by

the application of a magnetic field, because the experimental geometry and optical effects were not included. A report by Weiss *et al.* [10], did include the optical effects and the magnetic field enhancement was predicted, and gave relatively good agreement at fields <1 T. The magnetic field enhancement of the THz radiation from a range of semiconductors including InAs, InP, GaSb and InSb was also studied by Weiss *et al.* [11] and although the largest magnetic field enhancement factor was found for InSb, the largest overall emission was found to come from InAs.

Potential applications for the use of InAs as a source of coherent THz radiation have been discussed [12, 13], but it has been concluded that the powers that are generated at room temperature and with magnetic fields <1 T compare unfavourably with those generated by a biased stripline at room temperature and with no need for the application of a magnetic field. The optical excitation of the surface of InAs by 1·55 μm wavelength femtosecond laser pulses has also been investigated [14] due to the wide use of this wavelength in optical fibre communications.

The purpose of the work presented here was to investigate the emission of THz frequency electromagnetic radiation from InAs surfaces subject to different conditions, and to use both time domain and bolometric detection techniques in the form of a photoconductive antenna and a Golay cell respectively. The results presented attempt to clarify some aspects of the emission mechanism and verify the average emitted THz power that can be obtained from bare InAs surfaces. A comparison of this power with that generated by a biased stripline source is also made.

3.1 Experimental Techniques

The use of the TDTS has been described in Chapter 2, hence only a brief discussion is given here in terms of the study of InAs. Before an InAs sample is used as the source for the coherent THz radiation, the CPS transmitter is used together with the dipole receiver to optimise the TDTS in the experimental configuration shown in Figure 2.1. The optimisation procedure is also described in Chapter 2, and is iteratively performed to give a large current (~15 nA) in the receiver, but more importantly to give a large bandwidth. The bandwidth discussed in this thesis is thus defined as the upper frequency at which the amplitude of the detected frequency spectrum drops to one tenth of the maximum (*i.e.* 10^{-2} in power), and will be referred to as $f_{0\cdot1}$. Typically, an $f_{0\cdot1}$ bandwidth of 3·2 THz can be achieved with the TDTS, as shown in the insert of Figure 2.4.

Once the optimisation of the TDTS has been performed, the optical beam incident on the CPS transmitter is redirected by a removable mirror, via a focusing lens, through the front optical access window of the cryostat. The focusing lens has a focal length of 25 cm and was situated 29 cm from the cryostat window, thus at 37·5 cm from the sample at the centre of the cryostat insert. Figure 3.1 shows how the TDTS in this configuration differs from the standard operating geometry in Figure 2.1. The sample was arranged in the cryostat as described in §2.1.6, and the point of illumination of the sample and the sample angle were adjusted to achieve a large peak to peak signal and $f_{0\cdot1}$ bandwidth. The usual conditions for the pump beam incident on the sample resulted in a measured average power of 360 mW at a wavelength of 765 nm, hence a pulse energy of ~4·5 nJ.

The detected amplitude of the THz transient emitted from the more heavily

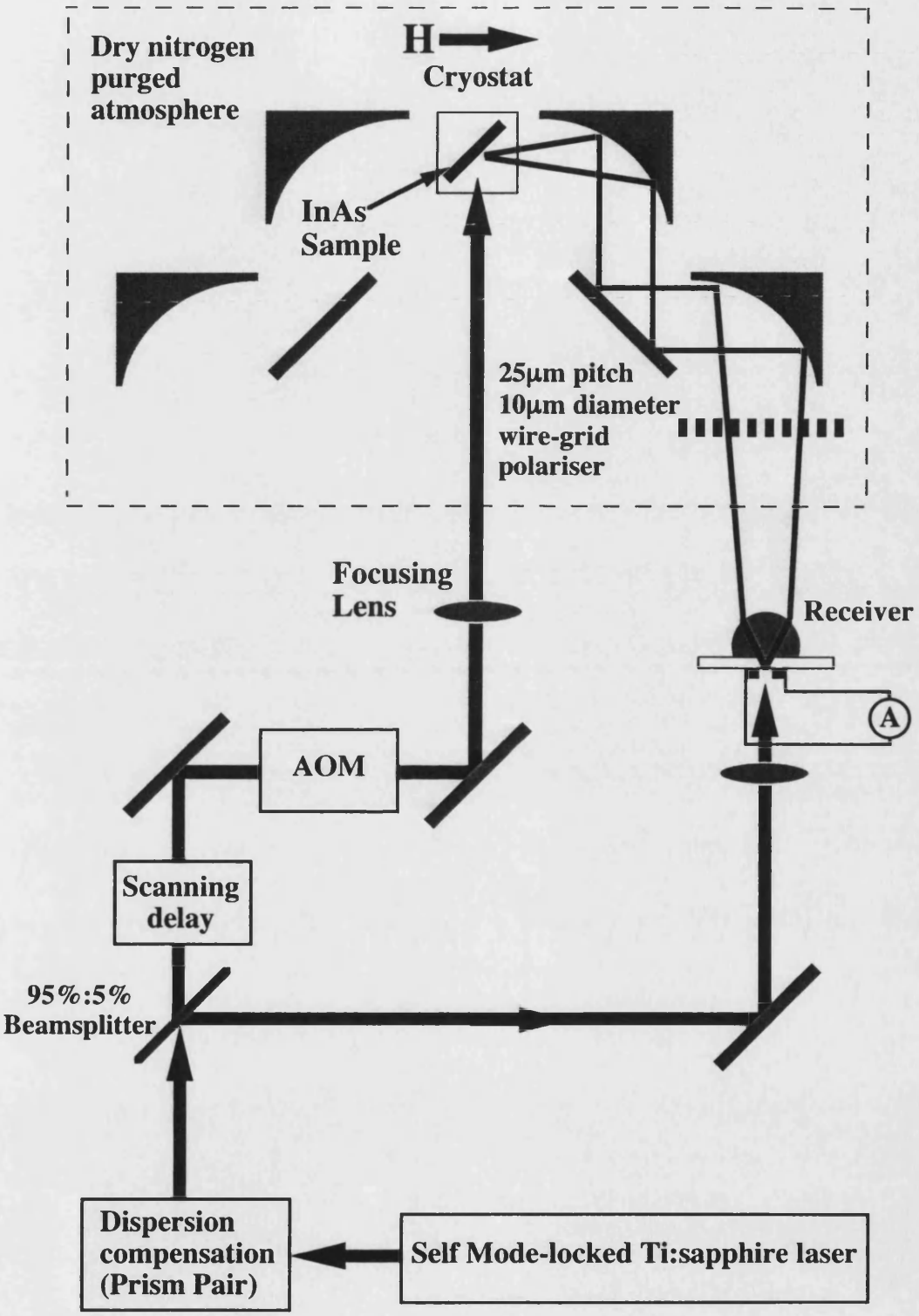

FIGURE 3.1: The TDTS experimental configuration to detect the THz radiation emitted from the surface of an InAs sample.

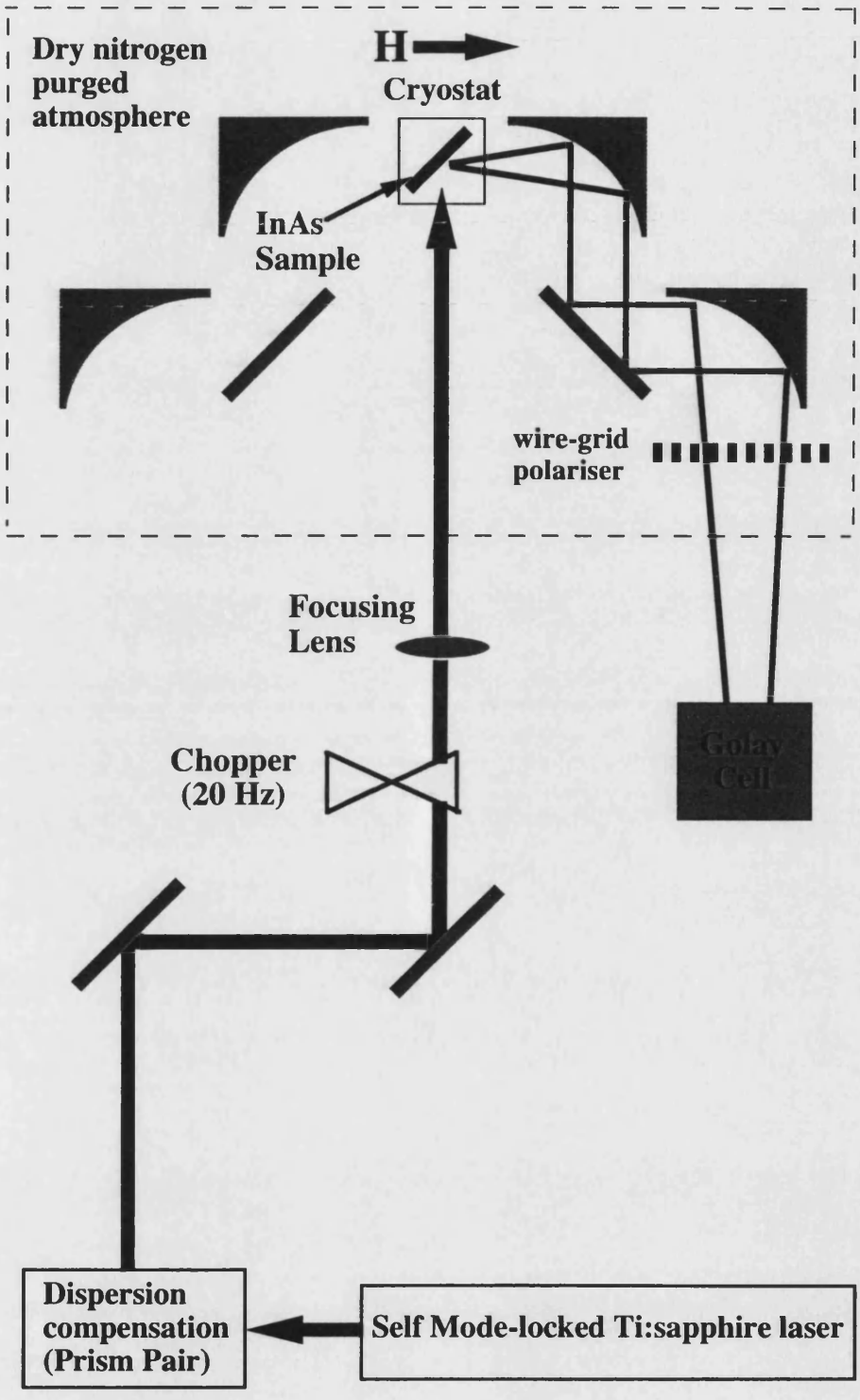

FIGURE 3.2: The experimental geometry to detect the average THz power emitted from the surface of an InAs sample by using a Golay cell.

doped InAs samples was significantly smaller than that observed for the lightly doped samples. Therefore, to improve the signal to noise ratio (SNR), an acousto-optic modulator (AOM) was introduced into the pump beam, operating at a frequency of 6·043 kHz, with a modulation depth of 90 %. A lock-in amplifier (LIA) was used to measure the modulated signal detected by the receiver, and the output from the LIA fed into an averaging oscilloscope. The LIA was used with a line filter and with a time constant of 300 μs or 1 ms, depending on the scan length and rate of the rapid scanning delay line (SDL).

When bolometric measurements were made with the Golay cell, the system was initially set up so that a good peak to peak signal was detected by the receiver. The Golay cell was then inserted in place of the receiver, and a mechanical chopper modulating the beam at 20 Hz was inserted in the beam path prior to the focusing lens; neither the AOM nor the SDL were used with the Golay cell. Figure 3.2 shows the experimental system when the Golay cell was used.

3.2 Properties of Indium Arsenide

When a semiconductor surface or interface is illuminated by an ultrafast laser pulse with photon energy greater than that of the band gap of the semiconductor, electron-hole pairs are created in the material within the absorption depth of the incident radiation. If there is a static electric field at the surface or interface, the free carriers are driven by the static field and accelerate along the field direction and produce a transient photocurrent. One of the largest average powers of THz radiation is generated in InAs, which is due in part to the presence of a large electric field found at the surface because of the presence of occupied surface

states which pin the Fermi level above the conduction band minimum[15]. The Fermi level has been observed to lie up to ~0·1 eV above the conduction band minimum on simple oxidised InAs surfaces[16, 17]; although it has been observed to lie up to ~0·6 eV above the conduction band minimum when metal alkali adatoms are introduced to the surface instead of oxygen [18]. The downward band bending leads to the formation of accumulation and inversion layers at the surface of *n*-type and *p*-type InAs respectively which give rise to relatively large electric fields of the order of $10\,\mathrm{kV\,cm^{-1}}$ [19].

The surface accumulation layer is similar to a two-dimensional electron gas (2DEG) [20], and is ~100 Å from the surface and one thermal wavelength [21], or 80 Å wide [22], with a sheet carrier density of $\sim 10^{12}\,\mathrm{cm^{-2}}$ [23]. Figure 3.3 shows the results of a calculation of the carrier density close to the surface region for two different *n*-type InAs samples with doping concentrations of $10^{15}\,\mathrm{cm^{-3}}$ and $10^{18}\,\mathrm{cm^{-3}}$ and for a *p*-type sample with a bulk carrier concentration of $10^{18}\,\mathrm{cm^{-3}}$. As can be seen, the carrier density in the surface accumulation layer is relatively independent of the carrier concentration of the bulk charge carriers, and the majority carrier type. The calculation assumes a surface state pinning energy of 0·3 eV and takes into account the effects of quantum confinement as discussed by Lachenmann *et al.* [24]. The calculated value of $\sim 3\times10^{12}\,\mathrm{cm^{-2}}$ sheet density, is supported by the measured values reported in the literature, and by some of the results in this thesis. The density of the free carriers in the surface accumulation layer has been observed to be independent of temperature down to ~10 K [25, 26]. The properties of the electrons in the surface accumulation layer differ from those of the electrons in the bulk [27, 28]. The electron mobility of nominally undoped ($\sim 2\times10^{16}\,\mathrm{cm^{-3}}$) bulk *n*-type InAs has been measured to be $10^{5}\,\mathrm{cm^{2}\,V^{-1}\,s^{-1}}$ or more, whereas in the surface accumulation layer it has been determined to be

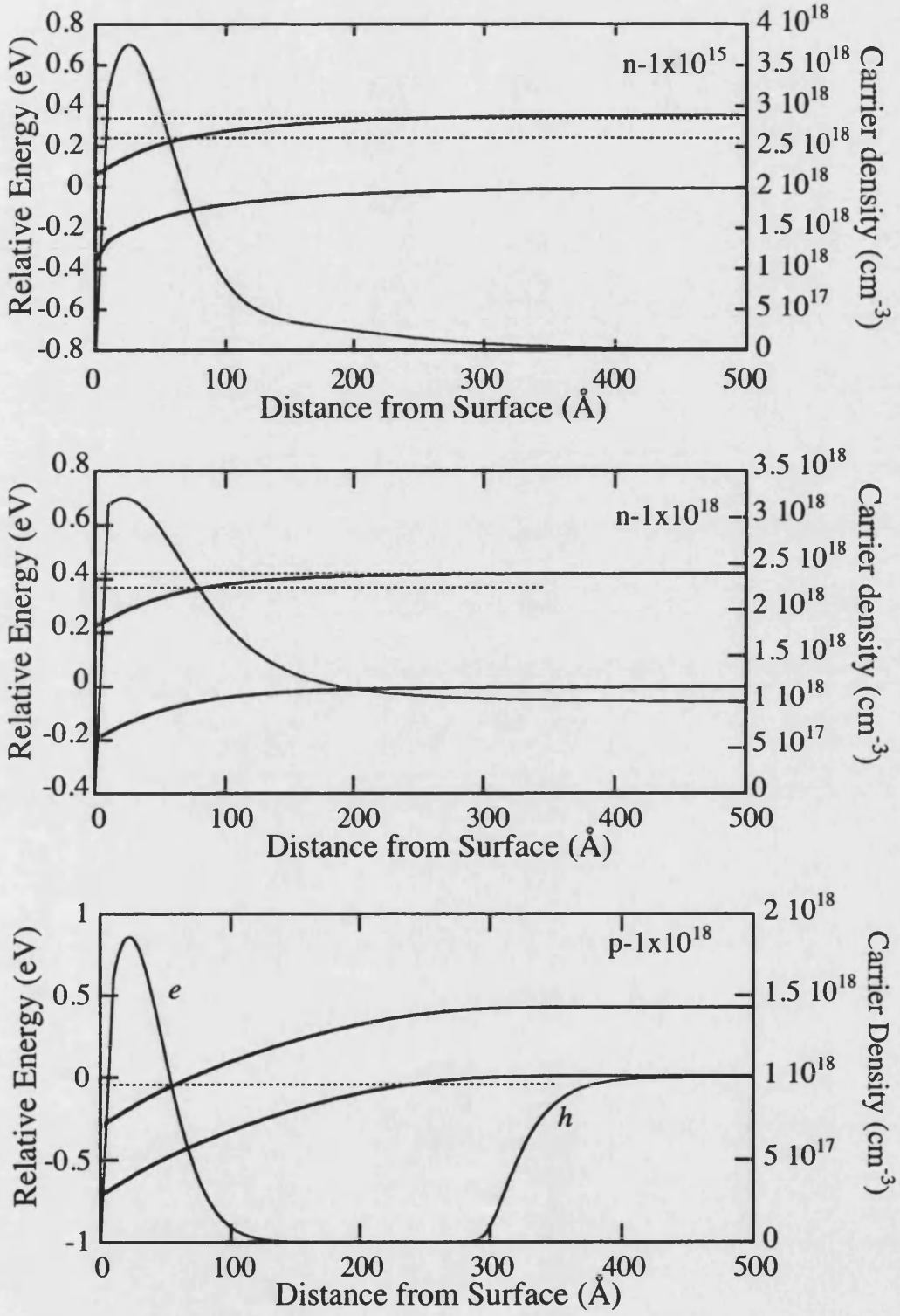

FIGURE 3.3: Carrier concentration dependence of the density of the surface accumulation layer in two n-type and one p-type samples. The dashed lines denote the energy range over which the surface bound states exist.

typically less than $10^4\,\mathrm{cm^2\,V^{-1}\,s^{-1}}$ [29]. The pinning of the Fermi level at the surface and the associated band-bending increases the electron effective mass in the surface accumulation layer to $\sim 0{\cdot}06 m_e$ because of the effects of band non-parabolicity. The bulk electron effective mass has been determined [30] to be $0{\cdot}023 m_e$ at the conduction band minimum.

Some optical properties of InAs were measured because of the existence of this surface accumulation layer, and the lack of information in the literature concerning the effects it may have. The absorption depth of near infrared radiation was measured along with the angle dependent reflectivity to determine that the samples would behave as expected. To measure the high frequency characteristics of the surface accumulation region, the frequency dependent reflectivity of THz radiation was also measured, by using the CPS transmitter as a source of THz radiation.

The absorption depth of near infrared radiation was measured using a sub-micron n-InAs epilayer, with a carrier concentration of $\sim 2\times 10^{16}\,\mathrm{cm^{-3}}$, mounted on a sapphire substrate as described in §2.2.1. The transmission of the radiation was measured through the epilayer and sapphire substrate, and then compared with the transmission through the sapphire substrate alone. The absorption coefficient of the InAs sample at room temperature was found to be $(2{\cdot}50\pm 0{\cdot}25)\times 10^5\,\mathrm{cm^{-1}}$ for a photon energy of 1·62 eV, which matches relatively well the values given in the literature [31]. The absorption depth is small, as can be seen by making a comparison with GaAs, which has an absorption coefficient of $2{\cdot}0\times 10^4\,\mathrm{cm^{-1}}$ at the same photon energy. The determination of the absorption coefficient of InAs is an important result, because it shows that the majority of the photoexcited carriers are created in a thin sheet well within the region of the surface accumulation layer.

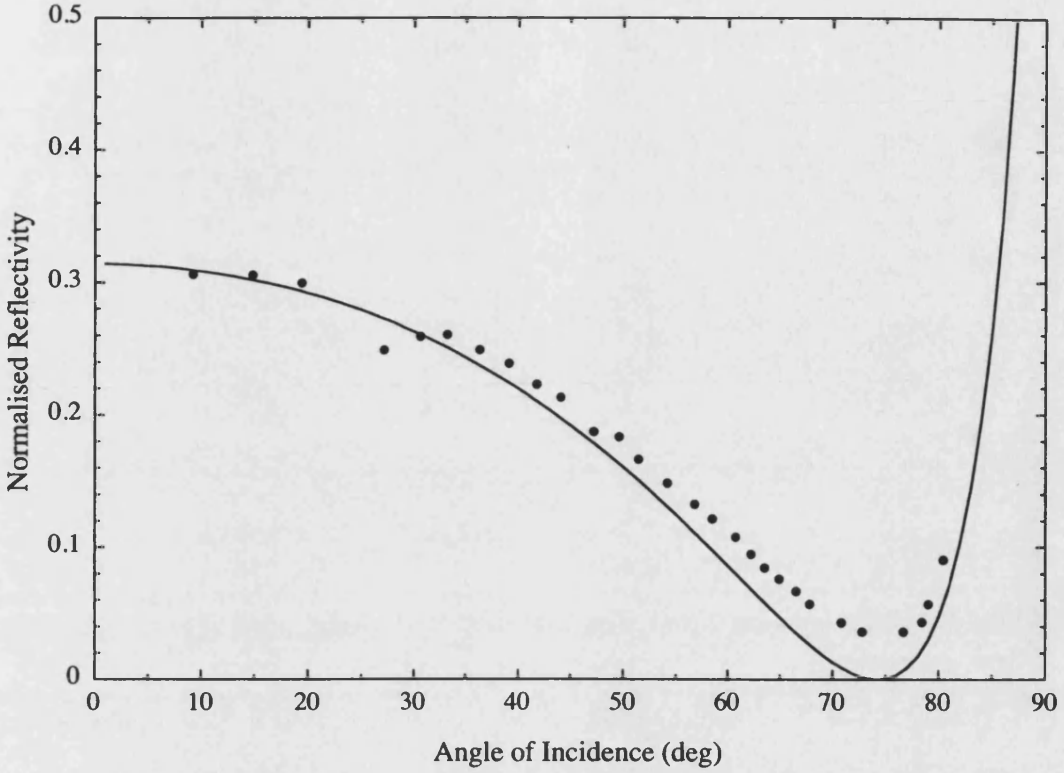

FIGURE 3.4: The measured absorption as a function of the angle of incidence of the light for the sample BK1 (n-$2\times10^{16}\,\mathrm{cm}^{-3}$).

The angle dependent reflectivity of the near infrared radiation was measured at a wavelength of 765 nm for the incident radiation p-polarised relative to the plane of incidence, on the nominally undoped sample designated as BK1 (see Table 2.1). The minimum reflectivity is expected at Brewster's angle, $\vartheta_B = \tan^{-1}(n_s/n_o)$ where the refractive index of undoped n-InAs $n_s = 3{\cdot}7$ [32] and n_o is the refractive index of air. For these values, Brewster's angle is $\vartheta_B = 75°$, which corresponds to the measured reflectivity shown in Figure 3.4.

3.2.1 Reflectivity of THz Radiation

To measure the high frequency reflectivity of InAs samples, THz radiation was reflected from the surface of the samples and detected by the receiver; the CPS transmitter was used as the source for the THz radiation. The InAs samples were placed in the path of the THz radiation and the reflected beam from the surface collected and directed on to the dipole receiver in the usual manner. The Fourier components associated with the measured THz transient were then determined by performing a FFT on the recorded traces. The reflected frequency spectra were referenced to the spectra obtained by reflection of the THz beam from separate gold mirrors, which were the same sizes as the individual InAs samples investigated. The reflectivity of the mirrors was measured before and after each sample and the results normalised to this average reference. Two *n*-type (IC106 and BK1) and two *p*-type (IAS1064 and DRA18) InAs samples were investigated, and the results are compared with those predicted by calculations based on a Drude model, which is shown in Figure 3.5. There is relatively good qualitative agreement between the model and the experimental data.

The features seen at 0·15 THz and 1·8 THz for the samples IC106 and BK1 respectively can be explained in terms of absorption of the THz radiation by bulk plasma oscillations. The frequency of the plasmons, ω_p can be described by the equation

$$\omega_p = \sqrt{\frac{Ne^2}{\varepsilon m_e^*}} \tag{3.1}$$

where N is the density of free carriers, ε is the high frequency dielectric constant, e is the electron charge and m_e^* is the electron effective mass. From Equation 3.1

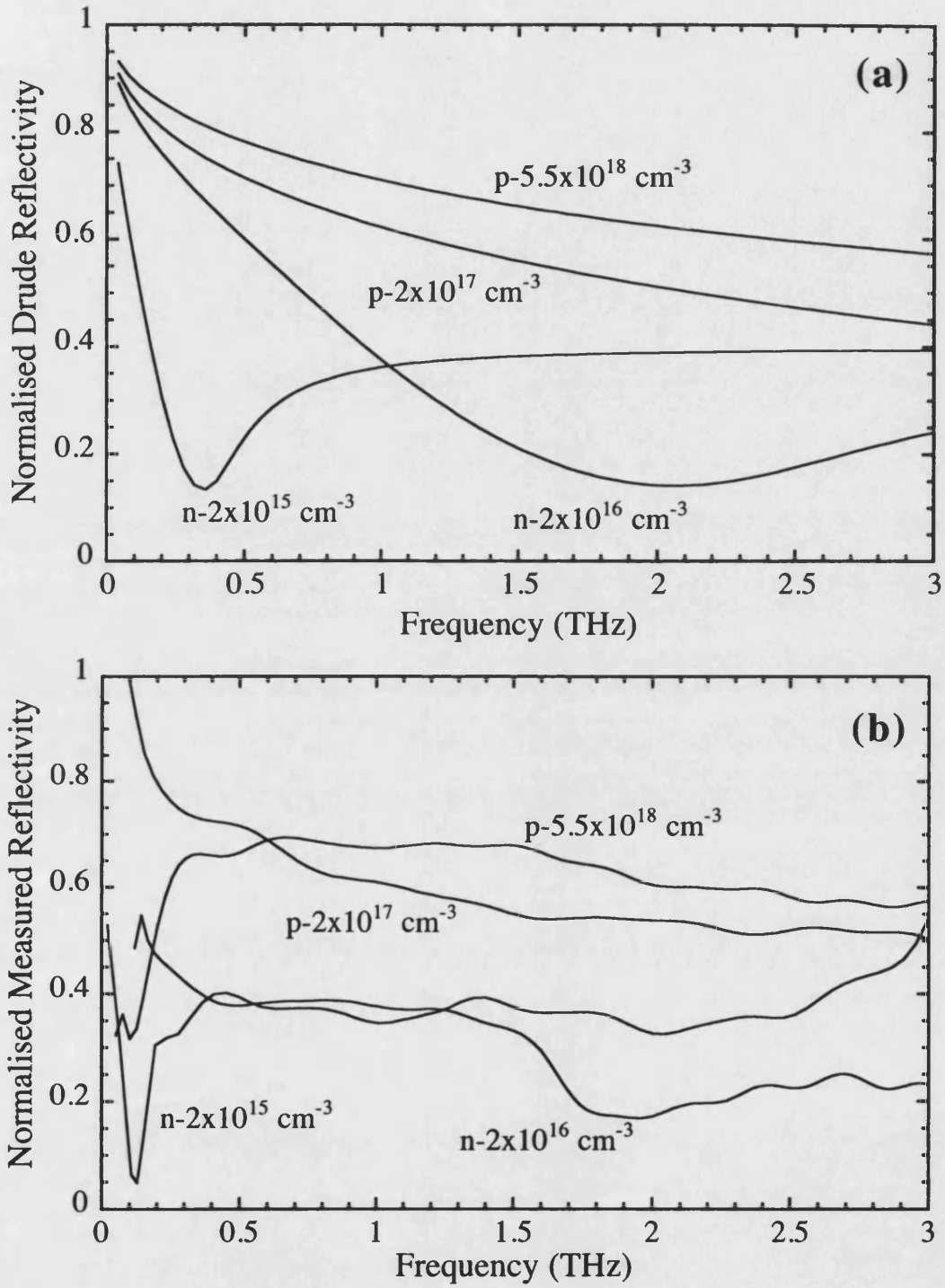

FIGURE 3.5: A comparison of the **(a)** a calculation based on the Drude model and **(b)** the measured reflectivity of THz radiation by differently doped InAs samples.

it is possible to calculate the density of the carriers associated with the plasma oscillations. In this case the carrier concentrations are found to be $1{\cdot}0{\times}10^{14}\,\mathrm{cm}^{-3}$ and $1{\cdot}3{\times}10^{16}\,\mathrm{cm}^{-3}$ for IC106 and BK1 respectively. If these values are compared with those in Table 2.1, relatively good agreement is found for the BK1 sample but IC106 has been measured by a Hall technique to have a carrier concentration an order of magnitude larger [33].

It is an important point to make that no plasmons are observed for the p-type samples. This is not unexpected, as the light hole plasmon frequency that is generated in each sample is 55 THz and 10 THz for DRA18 and IAS1064 respectively, and both these frequencies are beyond the detection bandwidth of the receiver. This also holds true for the more heavily doped n-type samples, such as IC311 which has a carrier concentration of $1{\cdot}0{\times}10^{17}\,\mathrm{cm}^{-3}$, and thus a bulk plasmon frequency of 31 THz.

3.2.2 Sample Characteristics

The physical reason for the large transient currents that give rise to the large amplitude electric fields that are radiated from InAs surfaces is the presence of the surface states which ultimately, by the band-bending, give rise to the large surface accumulation electric fields. It is thought the surface states arise through the same mechanism that pins energy levels at 300-500 meV above the conduction band minimum at InAs/GaAs interfaces [34].

Dislocations at a surface or interface in InAs affect the local conductivity in several ways, and any dangling bonds can produce amphoteric native defects [35]. To investigate whether samples grown by MBE (molecular beam epitaxy) or bulk

growth techniques differ, samples prepared by each method, but with nominally the same doping density, were studied (see Table 2.1). The surface finish on a CZ wafer (grown by the Czochralski method) is achieved by mechanical polishing, which is in contrast to MBE growth where no mechanical polishing of the surface after fabrication is required. The different processes and the effect on the surface states in $\langle 100 \rangle$ n-InAs has been explored in the literature [36]. Indeed, according to Ölsson *et al.* [19] the strain from the InAs–GaAs interface mismatch extends up to 2–3 μm into the InAs epilayer. The differences between a polished wafer and an MBE grown wafer in terms of the surface states, and hence in this case the surface electric field, are unknown. The samples IC196 and BK1 were studied both with the Golay cell and the receiver, and only slight differences were found in the signals, which could be attributed to experimental error and slight differences in properties of the samples.

To investigate further the effect of the surface states on the THz emission, two samples of BK1 were etched in a solution of $HCl:H_2O_2:H_2O$ in the ratio 1:12:48 for 10 minutes to remove the surface oxides [37] and a few hundred Ångströms of the InAs from the surface. One of the samples was subsequently rinsed in DI water, the other having been immersed in a solution of $(NH_4)_2S$ that acts as a passivating solution [38]. The solution prevents the formation of surface oxides, particularly on InAs, by the formation of a mono-layer of InS instead of InO. Both these samples, however, exhibited the same behaviour as the untreated BK1 sample.

3.3 Magnetic Field Enhancement of the THz Radiation Emission from InAs Surfaces

The initial experiments to measure the emitted THz radiation from InAs surfaces, were performed with the Golay cell to determine the absolute average powers generated by the different InAs samples under a range of different experimental conditions. Subsequently the dipole receiver was used to study the THz transients and the results compared with the measurements made with the Golay cell.

Both the Golay cell and the dipole receiver were used within one metre of the centre of the split coil superconducting magnet, and so they were tested for a magnetic field dependence. In the case of the Golay cell, a HeNe laser was placed up to two metres away from the magnet, and the light directed through the aperture of the Golay cell, which was situated in its usual position. The magnetic field was increased to a maximum of 7 T in 1 T steps, and the output of the Golay cell recorded. A small magnetic field dependence was discovered above 6 T; the effect being a decrease in the signal between 6 T and 7 T of the order of 10% due to the action of the stray field on the thermionic valve used in the construction of the Golay cell. This effect is corrected for in the data. No significant stray magnetic field dependence was found for the receiver, which was tested by using the TDTS in transmission mode with the CPS transmitter.

Most of the InAs samples investigated consisted of $\sim 4\mu$m thick InAs epilayers on GaAs substrates, and as such the component of the THz radiation that is emitted into the bulk of the samples tends to be reflected from the back interface and is observed in the time domain as a transient delayed temporally relative to the main initial transient. For the most lightly doped samples the amplitude of this

reflection is comparable with amplitude of the main transient. To try to reduce the effect of this reflection, a thick, ~5 mm, GaAs substrate was placed in optical contact with the back surface and the sample mounted over a hole in the sample stick.

3.3.1 Bolometric Detection of the Emitted Average THz Power

In this thesis, *s*-polarised light is defined as light where the electric field is perpendicular to the plane of incidence of the incident radiation; hence *p*-polarised is defined as that polarisation where the electric field is in the plane of incidence.

The initial experiments on the InAs samples were performed to determine the temperature dependence of the magnetic field enhancement of the emitted radiation. This was performed because it was thought that the signal might increase with decreasing temperature, as the mobility of the carriers increased [39], and to investigate the unexpected results of the temperature dependence of the emitted THz radiation presented by M^{c}Laughlin *et al.* [40], which were contrary to those reported by Ohtake *et al.* [41] and Kono *et al.* [42]. M^{c}Laughlin *et al.* had performed their initial work at 175 K, and Sarukura *et al.* at room temperature. However, one of the initial reports by Zhang *et al.* on several different semiconductor materials had shown a significant increase in the emitted power with decreasing temperature [5].

The magnetic field applied to the samples was ramped from 0 to 7 T and a value for the average power emitted was recorded every 0·5 T in both the *s*- and *p*-polarisations of the emitted radiation. The temperature was then decreased from

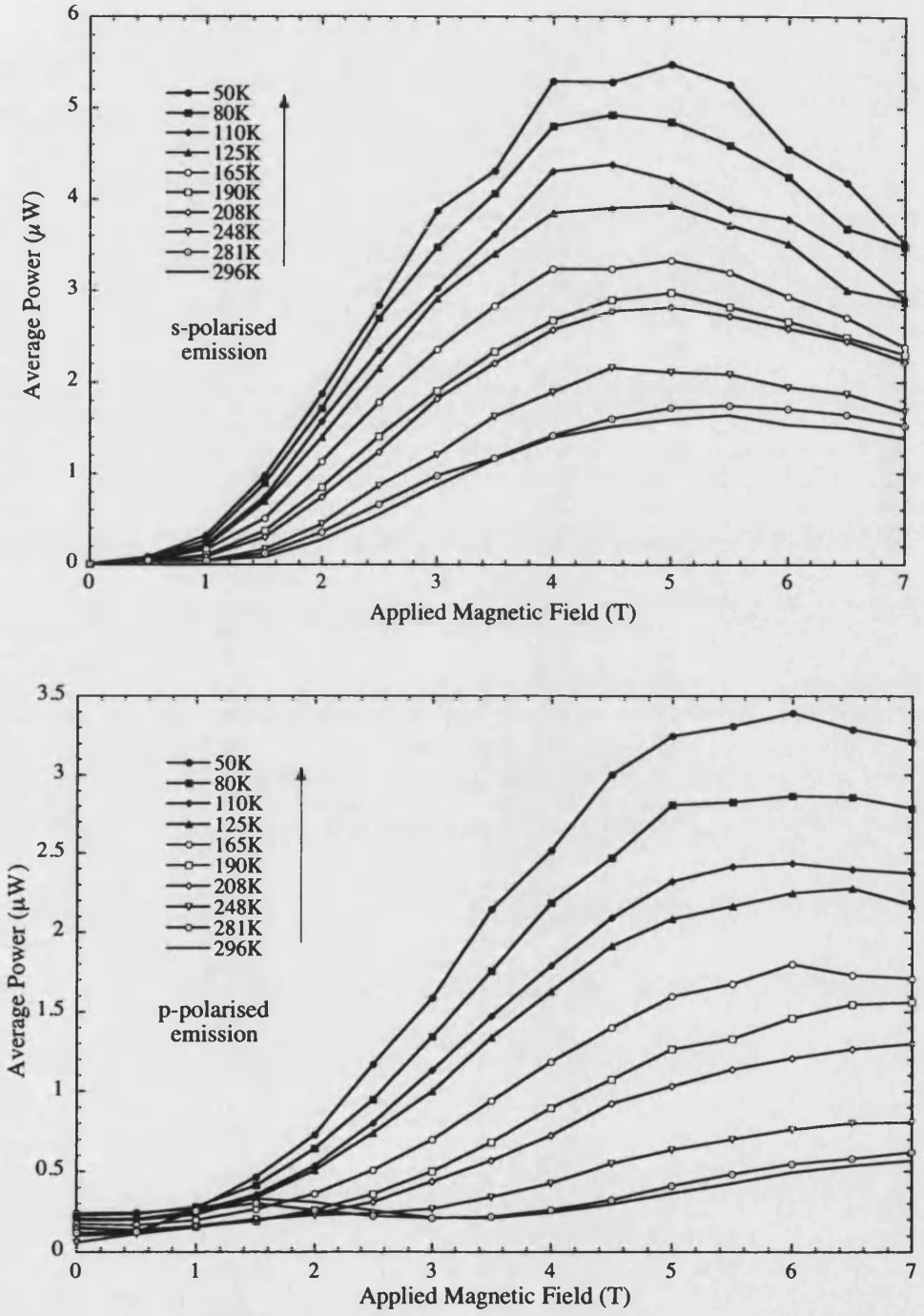

FIGURE 3.6: The average THz power emitted in the s-polarisation (top) and the p-polarisation (bottom) as a function of both sample temperature and applied magnetic field for the sample IC106 with an average optical pump power density of $15\,\mathrm{W\,cm^{-2}}$, at 765 nm.

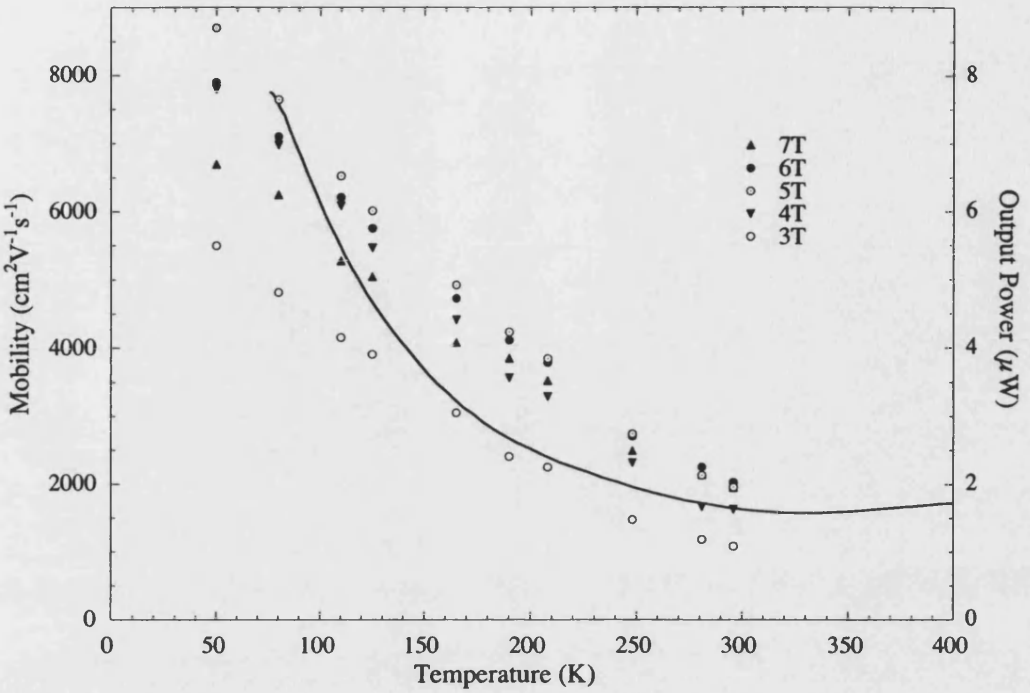

FIGURE 3.7: The temperature dependence of the measured average THz power (dots) from IC106 compared with the mobility [29] (solid line).

300 K to 10 K and the same procedure performed every ~50 K. Figure 3.6 shows the measured average power as a function of applied magnetic field and sample temperature of IC106 for both the *s*- and *p*-polarisations. The power output is seen to increase with decreasing sample temperature, and Figure 3.7 shows the temperature dependence of the measured power at a range of magnetic fields compared with the temperature dependence of the electron mobility, measured by Wang *et al.* [29].

Although a similar temperature dependent trend was observed for the samples designated as BK1 and IAS1064, which are *n*-type and *p*-type InAs respectively, the greatest power was observed for the sample with the highest mobility, that of IC106, with an average power of ~5·5 μW in the *s*-polarised component and

$\sim$3·5 μW in the p-polarised component. Both BK1 and IAS1064 showed lower power levels in both polarisations, as is seen in Figure 3.8 which shows the average power as a function of magnetic field at a sample temperature of 10 K. It is interesting to note that the detected power levels saturate in all of these samples at high magnetic field strengths, which is contrary to the measurements reported by M^{c}Laughlin *et al.* However, the observation of the saturation is supported by a more recent report by Sarukura *et al.* [43], in which even the double peak structure is observed in the s-polarised component of the magnetic field dependent emission of a sample with similar carrier concentration to the sample BK1. IC106, BK1 and IAS1064 are the only InAs samples that were investigated using bolometric detection. This is because the range of samples that were available for measurement at the time did not include the 'mid-range' n-type samples and the signals from the more heavily doped samples were too weak to be measured by the Golay cell.

3.3.2 Ballistic Model

The qualitative shapes of the magnetic field dependent measurements and an approximate upper limit for the average power generated, can be discussed principally in terms of the acceleration of electrons and light holes in the region of the surface accumulation layer. The strong electric field in this region provides sufficient force on the charge carriers to account for the average powers that are observed. In the model presented in this section, the electric field is assumed to be constant, with negligible screening effects due to the free carriers already present in the sample. The electrons and holes created during the time interval of the laser pulse, $\sim$70 fs, are accelerated due to the action of the electric and magnetic fields on them, leading to a time varying current, such that the current

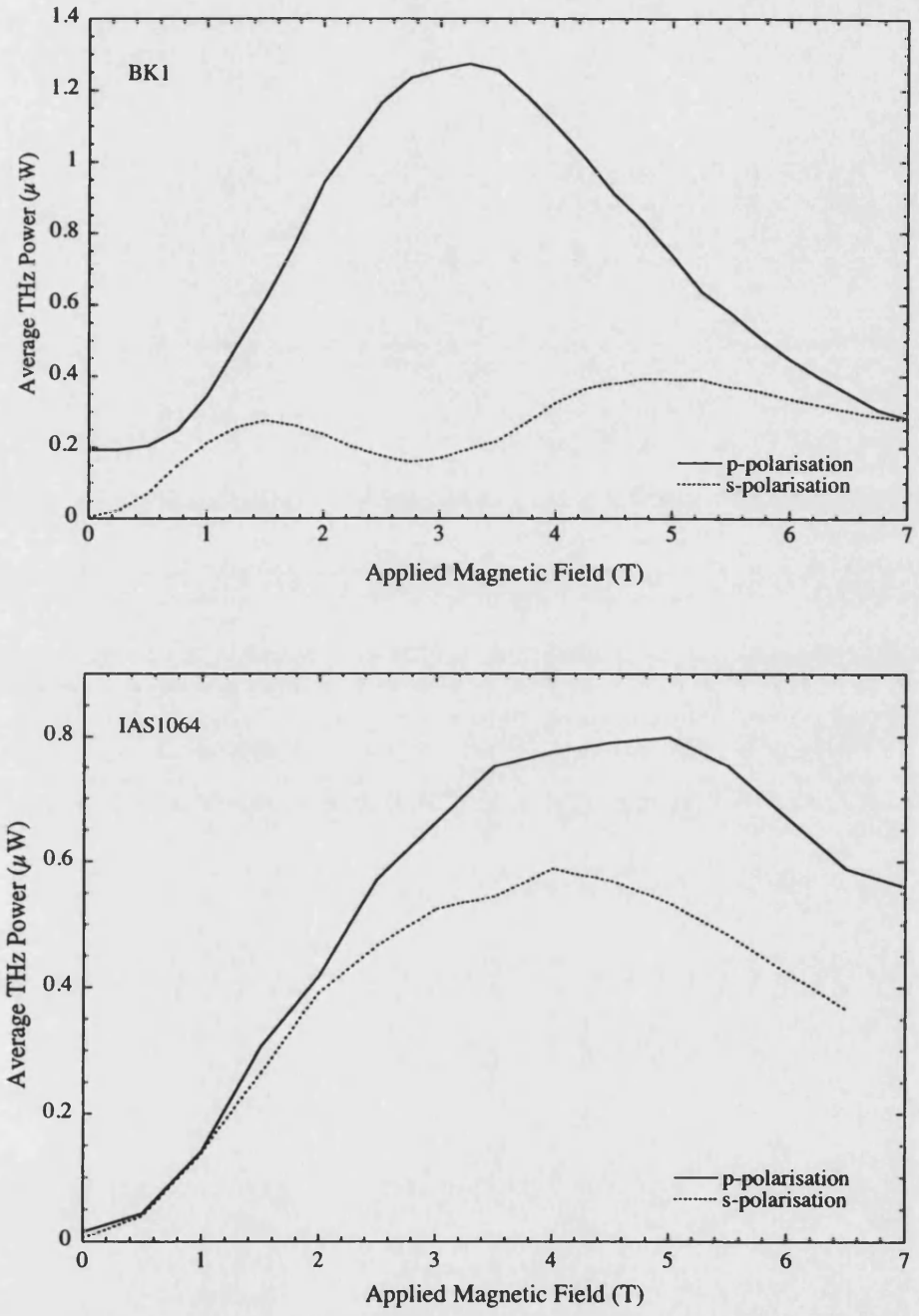

FIGURE 3.8: The average THz power emitted in the s-polarisation (dashed) and the p-polarisation (solid) by BK1 (top) and IAS1064 (bottom) as a function of applied magnetic field, at 10 K. An average near infrared pump power density of 15 W cm^{-2} was used at a wavelength of 765 nm.

density $\mathbf{j}$ can be defined as,

$$\mathbf{j}(t) = -Nq\mathbf{v} \tag{3.2}$$

where any diffusive contribution has been neglected. This is a common and convenient approximation [44], although it is more difficult to justify in this context due to the high density and energies of the photoexcited carriers. In the above equation N is the density of free carriers and $\mathbf{v}$ is the carrier velocity, averaged over the carrier distribution.

The current derivative is calculated as a function of time, taking into account the screening of the electric field due to the spatial separation of the photogenerated electrons and holes, in a manner similar to that described by Jepsen *et al.* [45] for a biased stripline antenna.

$$\frac{\mathrm{d}\mathbf{j}}{\mathrm{d}t} = Nq\frac{\mathrm{d}\mathbf{v}}{\mathrm{d}t} + \frac{\mathrm{d}N}{\mathrm{d}t}q\mathbf{v} \tag{3.3}$$

The time dependence of the free carrier density is given by Equation 3.4 below, such that the photo-excited carriers are able to contribute to the photocurrent for a time τ_c, defined as the 'capture time', until they enter a region of low electric field, or collide with the surface.

$$\frac{\mathrm{d}N}{\mathrm{d}t} = -\frac{N}{\tau_c} + g(t) \tag{3.4}$$

The term $g(t)$ is the generation rate of free carriers by the laser pulse, which is described using a sech^2 pulse of width 80 fs [46].

For a semiconductor in crossed electric and magnetic fields, the Drude-Lorentz model can be used to describe the time dependence of the average velocity [47], using a phenomenological conductivity scattering time, τ_s, to describe the effect of all intra- and inter-valley scattering processes for the dominant charge carrier,

$$\frac{\mathrm{d}\mathbf{v}}{\mathrm{d}t} = -\frac{\mathbf{v}}{\tau_s} + \frac{q}{m^*}(\mathbf{E} + \mathbf{v} \times \mathbf{B}) \tag{3.5}$$

where $\mathbf{B}$ is the applied magnetic field, m^* is the effective mass of the dominant charge carrier and $\mathbf{E}$ is the effective electric field acting in the region of the charge carriers, such that

$$\mathbf{E}(t) = \mathbf{E}_s - \frac{\mathbf{P}_{sc}(t)}{\eta\varepsilon} \tag{3.6}$$

In Equation 3.6, $\mathbf{E}_s$ is the surface accumulation electric field, ε is the high frequency dielectric constant, $\mathbf{P}_{sc}$ is the space-charge polarisation created by the photocarriers separating spatially in the field and η is a phenomenological constant describing the size of this screening effect. The screening parameter is unity in the case of carriers being created in an infinitesimally thin layer, but larger if the electron and hole charges overlap on picosecond time scales, as described by Jepsen *et al.* [45]. This parameter is needed because the spatial distribution of the carriers is not explicitly taken into account in the model. The polarisation term $\mathbf{P}_{sc}$ in Equation 3.6 provides a restoring force which leads to plasma oscillations of a frequency described previously in Equation 3.1. These oscillations have been observed in the InAs samples and an example is presented later in §3.4. The time dependence of the space-charge polarisation can be represented by,

$$\frac{\mathrm{d}\mathbf{P}_{sc}}{\mathrm{d}t} = -\frac{\mathbf{P}_{sc}}{\tau_r} + \mathbf{j} \tag{3.7}$$

where τ_r is the recombination time for the dominant charge carrier and is much longer than τ_c or τ_s [45].

By inserting Equation 3.6 into Equation 3.5 and taking the time derivative, then Equation 3.7 can be used to obtain the following second order differential equation,

$$\frac{\mathrm{d}^2\mathbf{v}}{\mathrm{d}t^2} + \frac{1}{\tau_s}\frac{\mathrm{d}\mathbf{v}}{\mathrm{d}t} + \frac{\omega_p^2\mathbf{v}}{\eta} = \frac{e}{m^*}\left[\frac{\mathbf{P_{sc}}}{\eta\epsilon\tau_r} + \left(\frac{\mathrm{d}\mathbf{v}}{\mathrm{d}t} \times \mathbf{B}\right)\right] \tag{3.8}$$

where the ω_p is defined as the angular plasma frequency in Equation 3.1. The radiated electric field is proportional to the carrier acceleration, $\mathrm{d}\mathbf{v}/\mathrm{d}t$, given in Equation 3.8, and so by solving the coupled Equations 3.7 and 3.8 together with Equations 3.2 and 3.4, then the radiated THz pulse can be calculated.

If the current density $\mathbf{j}$ is known, then it is possible to calculate the average power emitted in a direction α_2 by taking a time varying current confined in a volume V, which is small in each dimension with respect to the emission wavelength. The direction α_2 is defined as that between the surface normal and the axis of detection. For a point dipole, the power emitted into a unit solid angle along a direction α_2 can be expressed by Equation 3.9 [48], where θ is the angle between the current density $\mathbf{j}$ and the surface normal and ϕ_o is the corresponding azimuthal measured relative to the plane of emission. f is the repetition frequency of the laser and n is the bulk THz refractive index averaged over the spectral bandwidth of the emission.

$$\mathrm{I}_{p,s}(\alpha_2) \approx \frac{fV^2n}{6\pi\varepsilon_o c^3}\int_0^T \left(\frac{\partial \mathbf{j}}{\partial t}\right)^2 \mathrm{P}_{p,s}\left(\theta(t), \phi_o(t), \alpha_2\right)\mathrm{d}t \tag{3.9}$$

In Equation 3.9, Fraunhofer diffraction across the illuminated area is not taken into account. The finite size of a coherent source must also be taken into account because of Fraunhofer diffraction. If the time taken for the light to travel across the illuminated area is long compared with the scattering time, then the effect is small. For longer scattering times, however, the effect is to reduce significantly the radiated power. In this case, for an illuminated area of the sample of $\sim$1 mm^2, it is found that the radiated power is reduced by a factor of $\sim$30 for radiation with a frequency of 1 THz.

The terms P_p and P_s in Equation 3.9 contain factors that relate to the interface dipole angular power distribution, and have been derived by Lukosz [48] for the p- and s-polarisations respectively. These factors take into account the transformation of the transmission coefficient for the emitted radiation and the change in the solid angle of emission when passing from the semiconductor to a vacuum.

$$P_p = \frac{3}{2\pi} \frac{\cos^2 \alpha_2 \left(\cos\theta \sin\alpha_1 + \sin\theta \cos(\phi - \phi_o) \cos\alpha_1\right)^2}{n^3 \left(\frac{1}{n}\cos\alpha_1 + \cos\alpha_2\right)^2} \tag{3.10}$$

$$P_s = \frac{3}{2\pi} \frac{\cos^2 \alpha_2 \sin^2\theta \sin^2(\phi - \phi_o)}{n^3 \left(\cos\alpha_1 + \frac{1}{n}\cos\alpha_2\right)^2} \tag{3.11}$$

In the above equations α_1 is related to α_2 by $\sin\alpha_1 = \sin\alpha_2/n$. Lukosz has shown that the radiation patterns emitted by a dipole close to an interface between two different materials can be described simply in terms of the orientation of the dipole relative to the interface, the relative refractive index and the distance of the dipole from the interface. It has been shown that the presence of an interface can be expected to influence strongly the emission process if the dipole is within a distance of the surface which is comparable with the emission wavelength.

Within this limiting distance, the radiation emitted by a dipole parallel to the interface is much stronger than that emitted by a dipole perpendicular to the interface [48, 10], this is shown in Figure 3.9. Although the scale of the plots make it a little difficult to the see the emission for a dipole in a material with a high dielectric constant similar to InAs, the dipole parallel to the surface for a value of ε=1 is evidently much stronger than that found for a dipole perpendicular to the interface.

The physical effect of the interface is to enhance the increase in the radiated power with magnetic field by increasing the fraction of the radiation that is emitted into the vacuum. This is achieved by the action of the magnetic field which increases the angle θ between the current $\mathbf{j}$ and the surface normal by the Lorentz force.

The model takes into account the emission due to the additional acceleration of the charge carriers by the application of the magnetic field, together with the enhancement of the radiation due to the terms derived by Lukosz for a dipole at an interface. The physical parameters that have most effect on the qualitative shape of the plots predicted by the model and illustrated in Figure 3.11 are the carrier mass, the scattering times τ_s and τ_c and the phenomenological screening parameter η. In these plots, the electron effective mass at the band edge is taken as $0{\cdot}023m_e$, a scattering time, τ_s, of 100 fs, and a capture time, τ_c, of 10 ps is assumed along with a value for η of 10.

For n-InAs, the dielectric constant at high frequencies is taken to be 14.6 [32], and it can be seen with reference to Fig 3.10 that the proportion of the generated radiation that is emitted into the vacuum along the axis of detection, is small compared with the amount radiated into the substrate. This is supported by experimental observations, where large amplitude reflections of the time domain

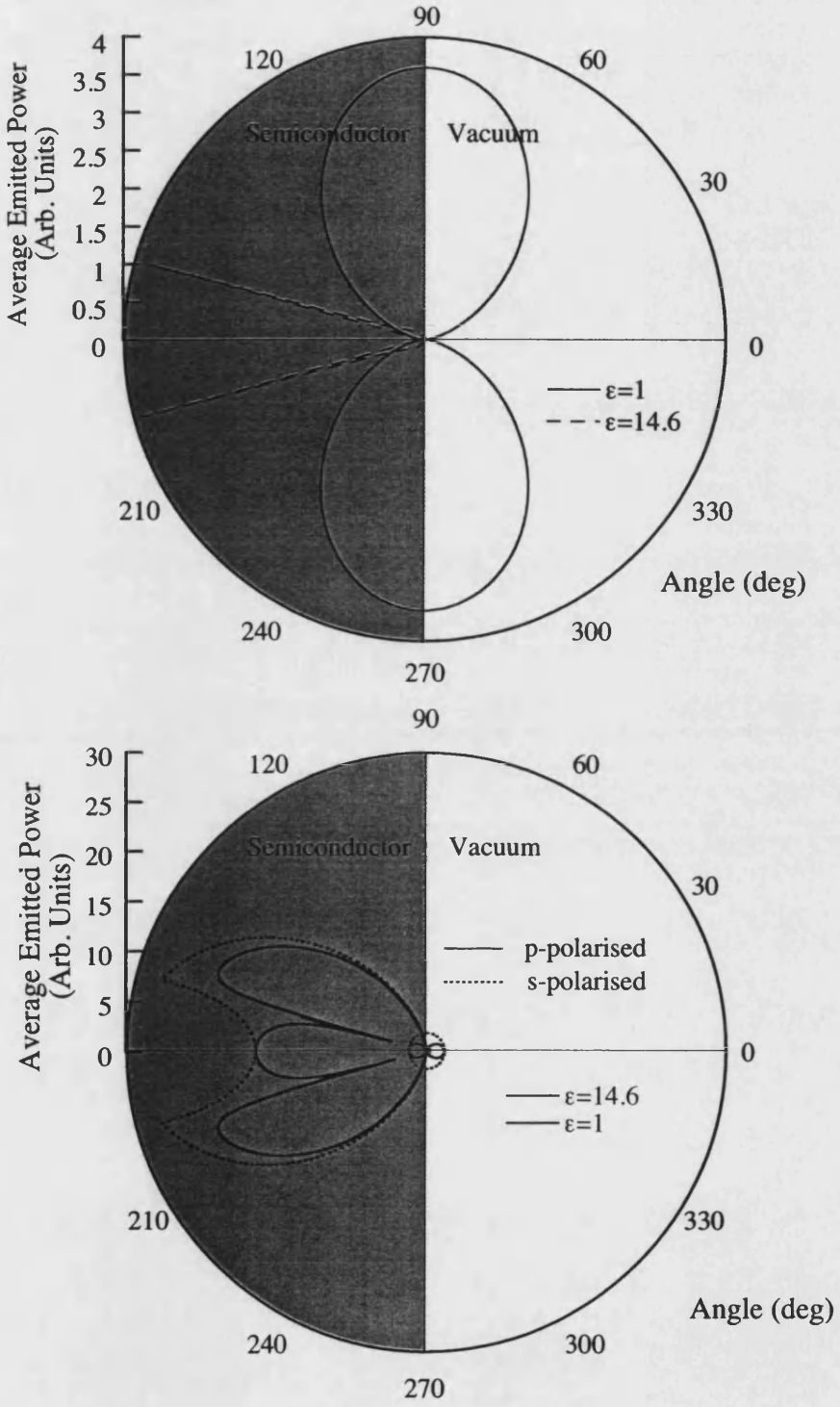

FIGURE 3.9: The differences between the dipole radiation emitted from a dipole perpendicular (top) and parallel (bottom) to a dielectric interface.

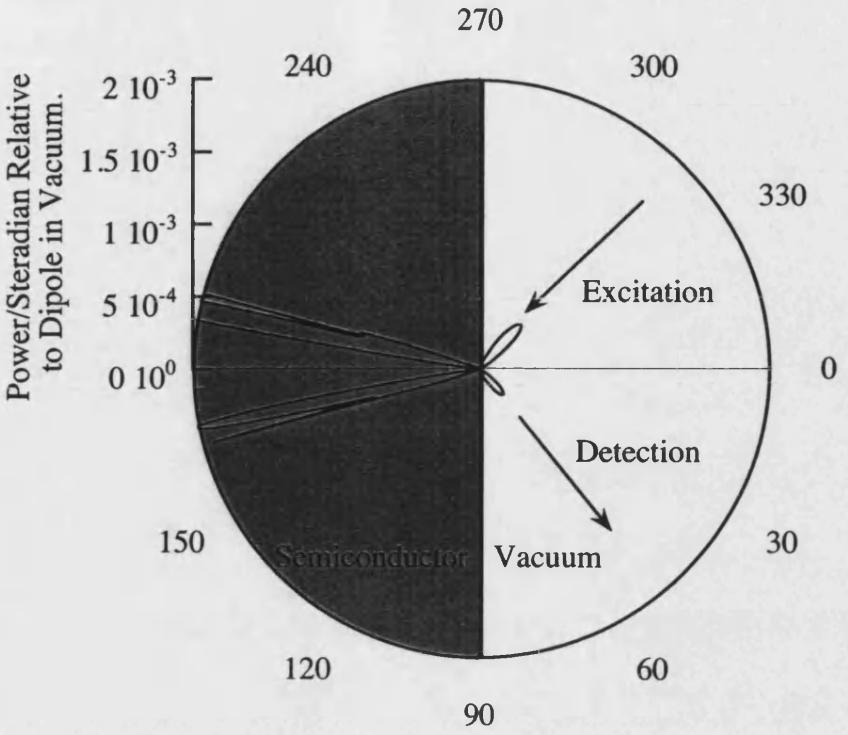

FIGURE 3.10: The dipole radiation emitted from the surface of InAs in the standard experimental configuration.

THz transients are observed from the back of the samples for the lightly doped epilayers of InAs. An effect not accounted for in the model, but that may act as another complication in the system is the fact that the epilayer samples constitute a stratified medium of GaAs and InAs on the scale of the emission [49]. This is despite the results of the THz reflectivity, shown earlier in Figure 3.5, which show that the dielectric properties of the surface layer can be treated simply for the high frequency radiation that is generated in the samples.

Figure 3.11 shows examples of the predicted variation of the emitted power with applied magnetic field for a sample in the usual geometry of 45° and for the geometry where the sample surface normal, and hence the surface electric field, is perpendicular to the applied magnetic field. The sample stick insert shown

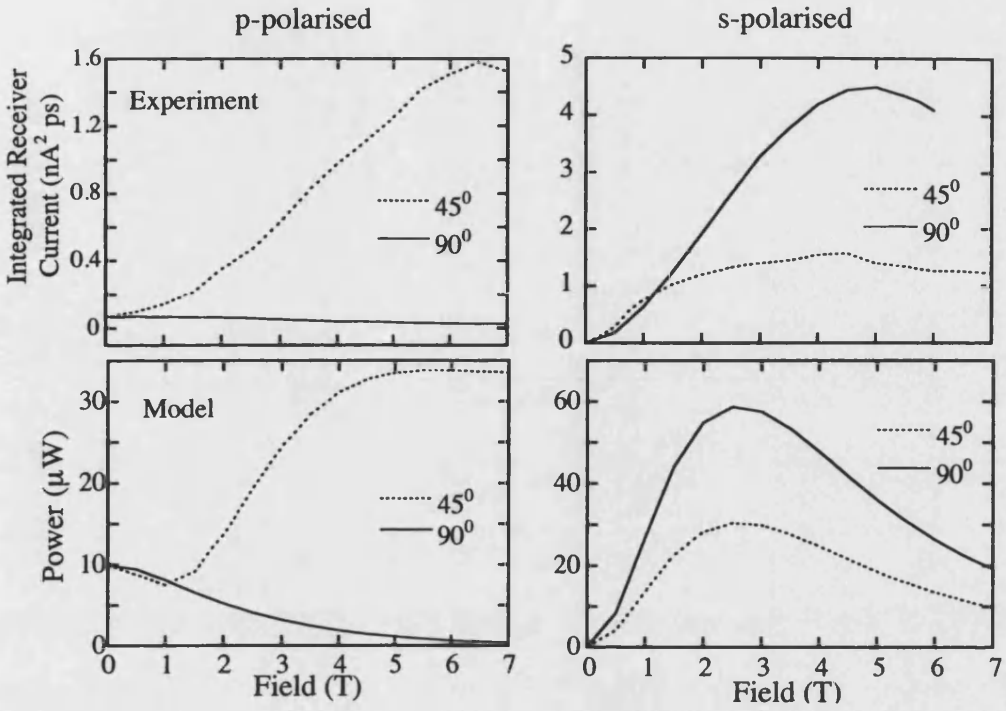

FIGURE 3.11: A comparison of the model with the measured effect for a p-$5{\cdot}5{\times}10^{18}\,\mathrm{cm}^{-3}$ sample. The angles 45° and 90° refer to the angle that the surface normal of the sample makes with the magnetic field.

in Figure 2.7 was used to provide a means by which the electric and magnetic fields could be crossed perpendicular to one another, whilst ensuring the light remained incident at 45° to the surface normal. In this somewhat simplified geometry, relatively good qualitative agreement is found between the model and the experimental results. The p-polarised component of the emission is found to decrease in amplitude with increasing applied field. This observation is predicted by the model, although the ratio of the zero field to the high field emitted power levels is seen to be less in the experimental data.

There is less qualitative agreement between the model and the experimental results when comparing the s-polarised component of the emission, although the measured emission does reach saturation in the 45° geometry, but at higher field

values. However, in this model the field at which the output saturates can be altered by changing the screening parameter, η, and the effective mass of the electron.

In this model, although the absolute average powers predicted, and the variation with an applied magnetic field show reasonable qualitative agreement with the observed magnetic field enhancement, the polarity of the emitted transient that is predicted by the model is incorrect. This is obviously a major flaw in the model, and thus there are extra, or different, effects that must be included in the model in the future, as it is developed further. Section 3.3.5 discusses the inclusion of terms to account for a diffusion current as well as the drift current, and the overall effect this has on the model, which is to give the correct polarity. Another deficiency is that the predicted magnetic field enhancement when comparing the signal strengths at 0 T and 7 T is not as great as that which is observed. However, the absolute powers that are predicted by the model are found to be of the right order of magnitude, $\sim 10^{-5}$ W, and the different experimental geometries show reasonable qualitative agreement with the experimental, for this relatively simple model of a very complicated system.

3.3.3 Coherent Detection of THz Electrical Transients

For the coherent detection of the transient THz electric fields the dipole receiver was used in the TDTS, as previously described. In this way the magnetic field dependence of the THz transients was investigated directly, and the average power that was generated within the bandwidth of the receiver was qualitatively compared with the results taken with the Golay cell. The measurements were made on the whole range of n- and p-type samples, and in some cases both the s-polarised component as well as the p-polarised component of the emission were measured. All measurements were taken at temperatures in the range 5 K to 30 K.

Figure 3.12 shows the p-polarised THz transients recorded for the full range of n -type samples, at 0 T and 7 T to show how the characteristics of the detected transient change with the application of the magnetic field. The small amplitude oscillations that are present after the initial transient in many of the traces are due to an optically excited absorption feature of the high resistivity silicon windows in the cryostat, and are discussed further in Chapter 4. With reference to the THz transients shown in Figure 3.12, it is clear that the peak to peak amplitude of the transients decreases with increasing carrier concentration, such that over the carrier density range $2\times10^{15}\,\mathrm{cm}^{-3}$ to $4\times10^{19}\,\mathrm{cm}^{-3}$, the amplitude of the transient is reduced by a factor of $\sim$300. Over this large range of samples with increasing doping densities, the mobility of the charge carriers decreases due to ionised impurity scattering, but there are also other effects by which the overall amplitude of the transient may be reduced. The surface accumulation field strength is expected to decrease with an increase in the bulk carrier concentration, as the bulk Fermi level rises towards the pinning energy at the surface. Additionally,

there is an increase in the effective mass of the electrons at the Fermi level with an increase in the carrier concentration [50]. It is found that with the inclusion of band non-parabolicity in a three band $\mathbf{k}\cdot\mathbf{p}$ calculation, an estimate of an increase in the the effective mass from $0{\cdot}023m_e$ at $2\times10^{15}\,\mathrm{cm}^{-3}$ to $0{\cdot}092$ at $4\times10^{19}\,\mathrm{cm}^{-3}$ can be made [51, 52]. The three band model describes the variation of the effective mass as a function of doping reasonably well for levels up to $10^{19}\,\mathrm{cm}^{-3}$ [29].

With an increase by a factor of four in the effective mass of the electron, and a decrease in the surface accumulation field, the signal is expected to drop significantly with an increase in the doping density for the n-type materials. For p-type materials however, the reverse is be expected. Although the scattering due to ionised impurities is expected to increase with increased doping , the effect of pushing up the Fermi level in p-type InAs is to increase the surface electric field due to the much greater degree of band-bending that is necessary because of the surface states. As can be seen with reference to Figure 3.14, the peak to peak amplitude of the signal reduces by a factor of $\sim$3 for an increase in the carrier concentration by a factor of $\sim$3, which is less than in the n-type materials, supporting the idea of the two competing processes.

As well as a decrease in the amplitude of the THz transients, the temporal width appears to decrease with increasing carrier concentration, certainly up to $1\times10^{17}\,\mathrm{cm}^{-3}$. This is supported by looking at the frequency spectra shown for the transients in Figure 3.13. However, the Fourier components of the transients for the most highly doped sample could not be calculated because the traces were too noisy to be able to produce a spectrum. The spectral weight of the signals appears to shift to higher frequencies with an increase in the carrier concentration. IC106 emits the largest amplitude transient but has a maximum $f_{0.1}$ bandwidth

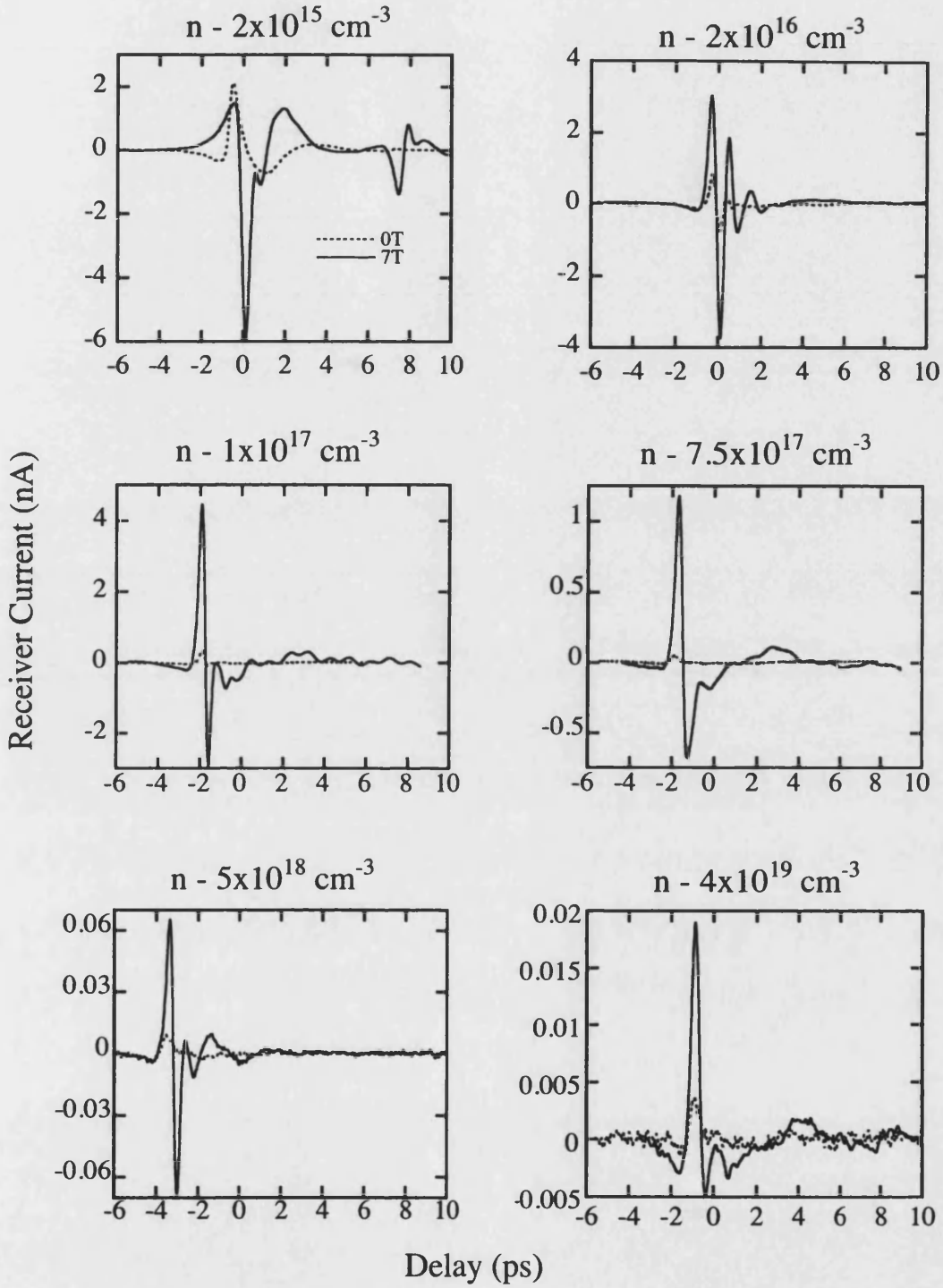

FIGURE 3.12: Time domain traces for the *n-type* samples with applied field strengths of 0 T and 7 T.

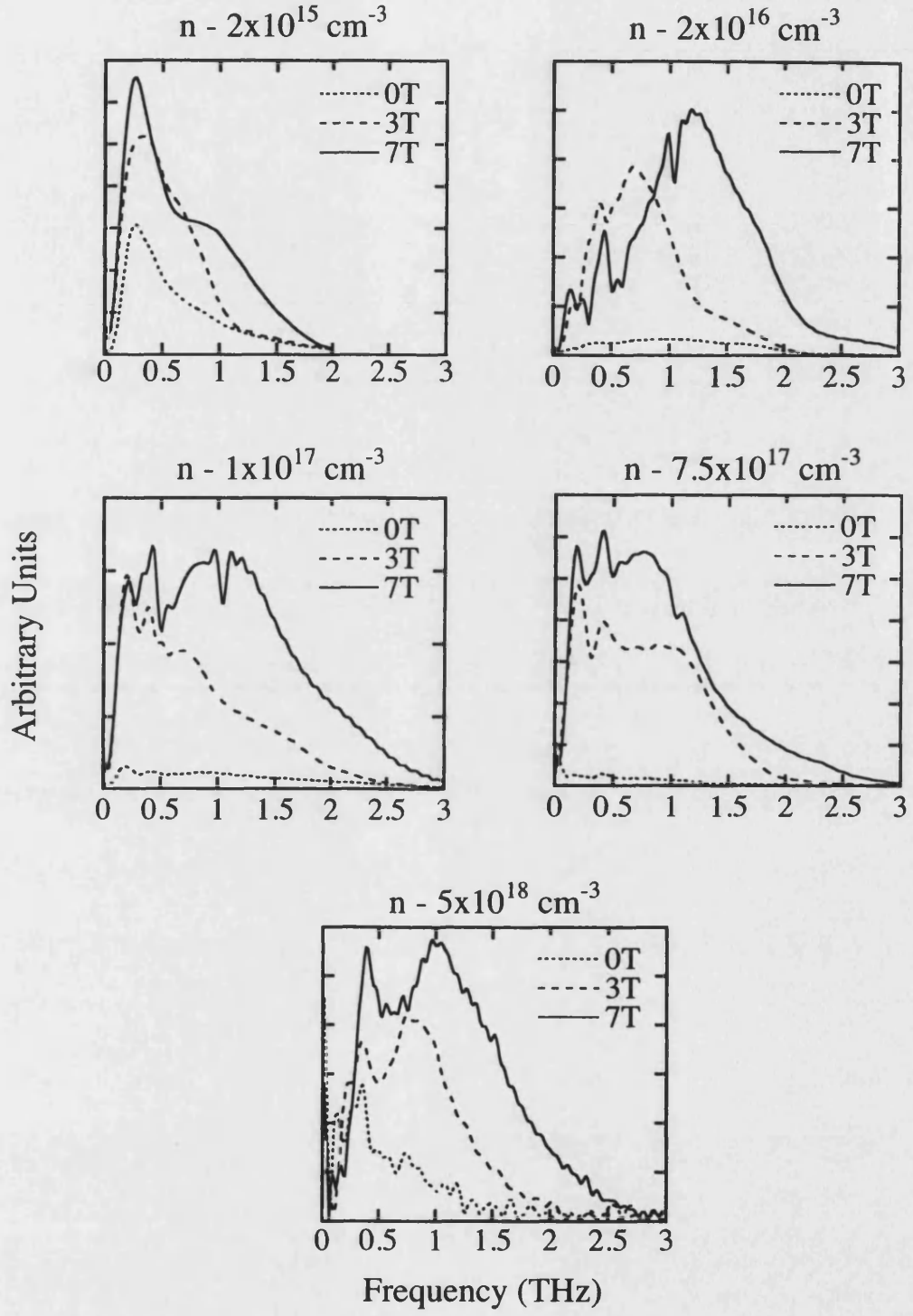

FIGURE 3.13: Fourier components of the time domain THz traces at 0 T, 3 T and 7 T for the n-type samples.

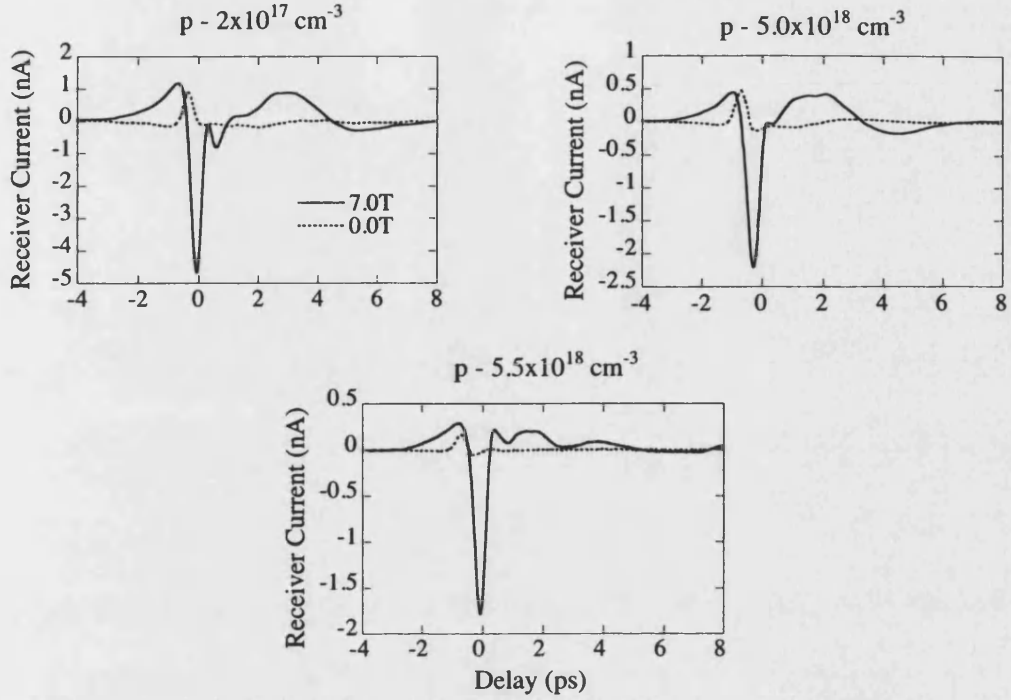

FIGURE 3.14: Time domain traces for the p-type samples with applied field strengths of 0 T and 7 T.

of 1·6 THz at 7 T, whereas the samples BK1 and IC311 have $f_{0.1}$ bandwidths of 2·3 THz and 2·6 THz respectively. The other n-type samples which are more heavily doped than IC311 have lower $f_{0.1}$ bandwidths.

The frequency spectra that are shown, are dependent on both the response of the receiver and the THz radiation that is incident on the dipole receiver. The receiver response, in terms of the finite detection bandwidth, is not thought to cause a significant problem, because the $f_{0.1}$ bandwidth observed when using the CPS transmitter with the receiver is greater at ~3·2 THz, and the bandwidth of the THz radiation generated in the InAs is less than this value.

The time domain traces of all the samples show that the zero magnetic field

transients are uni-polar and that signals from both the n- and p-type samples have the same polarity. A change in the signal polarity is not observed for an increase in the doping density across the range of samples, and thus it is concluded that the pinning energy at the surface of the samples might be larger than the Fermi energy in the most highly doped sample. If this is true then it implies that the pinning energy is greater than 0·6 eV, making the assumption that the polarity of the signal is determined by the direction of the surface field across the whole range of samples. However, this is only true if the current density is dominated by the drift current; the polarity of the surface field is irrelevant for a system dominated by a diffusion current, as discussed in §3.3.5.

A relative value for the power incident on the receiver can be calculated by integrating, over time, the square of the transient current generated in the receiver. This is possible because the current that is detected in the receiver is directly proportional to the electric field of the transient $\mathbf{E}_r(t)$ and so the instantaneous current generated in the receiver $I_r(\delta t)$ is directly proportional to the signal amplitude. Power is the square of the amplitude, and the summing of the squared instantaneous current over time results in the average relative power, thus

$$P_{av} = \int I_r^2(t)\,\mathrm{d}t \tag{3.12}$$

The integrations were performed carefully so as not to include any reflections and so as to ensure that the same portion of the total recorded trace was integrated for each sample. The value that is found is not an absolute measure of the power, but the variation of the average THz power emitted as a function of applied magnetic field can be compared with the results taken by the bolometric technique because the emitted THz radiation was of sufficient average power to

be detected by the Golay cell. Figure 3.15 shows the integrated receiver current for the p-polarised component of the emission, as a function of magnetic field for the range of n-type samples. For samples where the magnetic field dependence has been measured using the Golay cell, a comparison is made with the integrated receiver current, which serves to show that the detection bandwidth of the receiver is sufficient to detect the dominant frequency components. Unfortunately, the more highly doped samples were not studied using the bolometric technique, and so no comparison could be made for these samples. The conversion factor between the integrated receiver current and the incident power depends on the spectral content but a value typically in the range 10-20 $\mathrm{nA^2\,ps\,\mu W^{-1}}$ was found in these experiments.

It can be seen with reference to Figure 3.15 that the sample with a carrier concentration of $2\times10^{16}\,\mathrm{cm^{-3}}$ exhibits a maximum in the output power at a lower field than the other samples, there is also a subsequent significant decrease in the emission — this is contrary to the other samples studied, and the results of the model, shown previously in Figure 3.11. The other n-type InAs samples are in better agreement with the power variation predicted by the model, although the field at which the emitted power reaches saturation is higher for the experimental data, suggesting that the model is lacking an important feature related to the influence of the magnetic field.

The plots in Figure 3.16 show the the p-polarised component of the emitted power generated in the p-type InAs materials. The qualitative shape of the integrated receiver current and the Golay cell measurements agree well for the example where both methods were used and can be compared. The magnetic field dependence of the emitted power is similar to that observed for the 'mid-range' n-type materials.

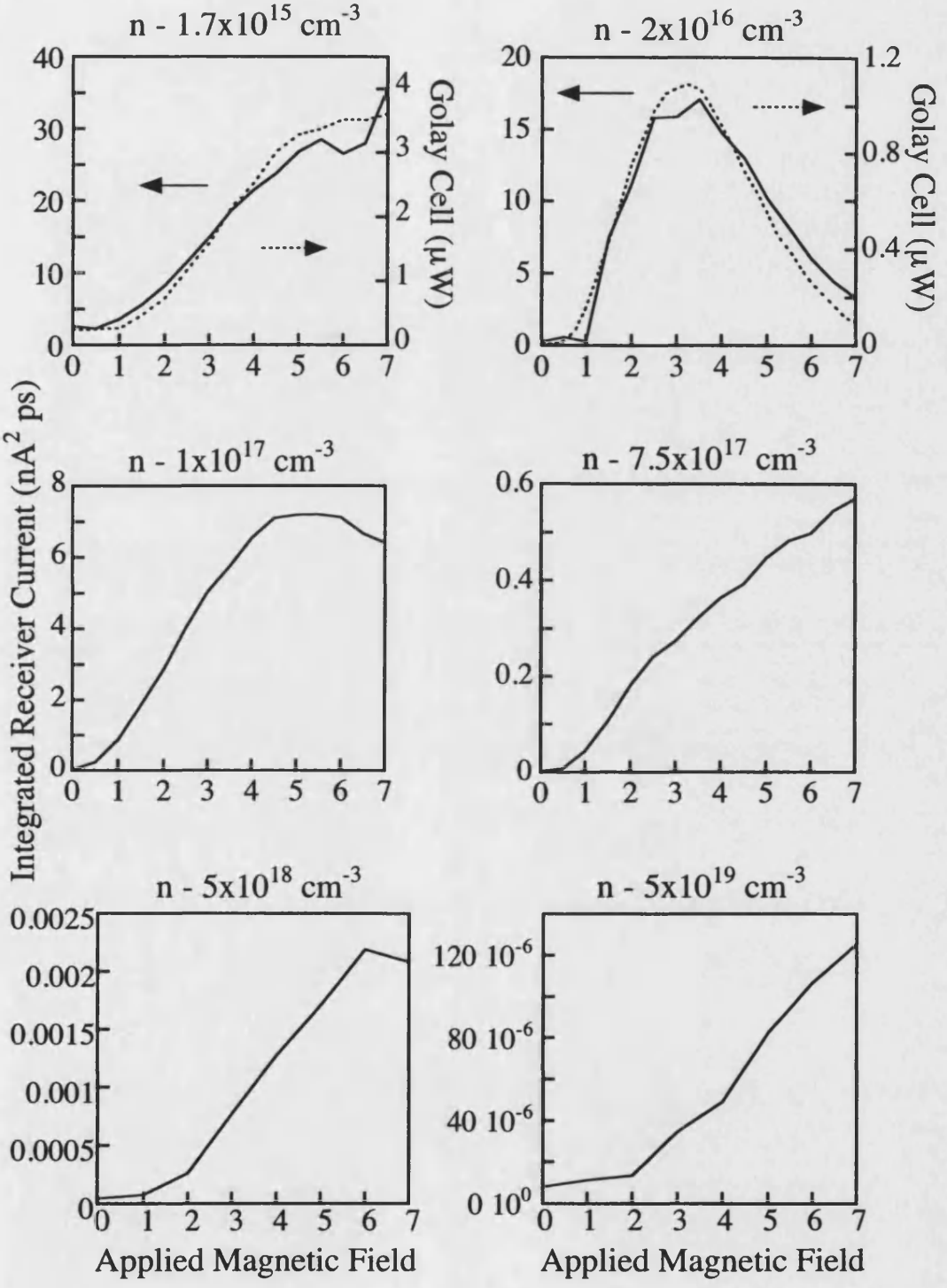

FIGURE 3.15: Integrated receiver current and measured average power of the p-polarised emission for all the n-type samples

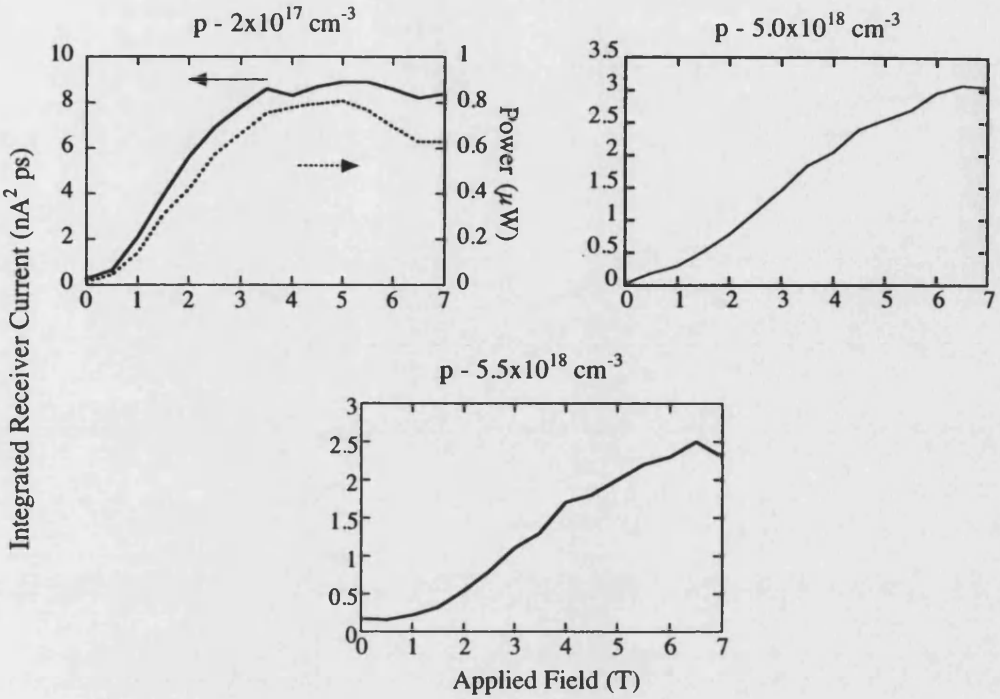

FIGURE 3.16: Integrated receiver current and measured average power for the p-type InAs samples in p-polarised emission.

A similar comparison is shown for the s-polarised component of the emission in Figure 3.17 for three n-type samples and one p-type sample. Again, comparing the Golay cell measurements with the integrated receiver for both of the lightly doped n-type samples shows good qualitative agreement, even for the anomalous 'double peak' structure mentioned previously.

The ratio of the maximum power measured to the zero applied field measured power, defined as the enhancement factor, in the p-polarised component is plotted in Figure 3.18 for both the p-type and n-type materials. The enhancement factor for the most lightly doped n-type material is found to be the same as that for the most heavily doped material, at $\sim$12, whereas the largest enhancement of $\sim$450 is found in the sample with a carrier concentration of $7{\cdot}5\times10^{17}\,\mathrm{cm}^{-3}$. Despite

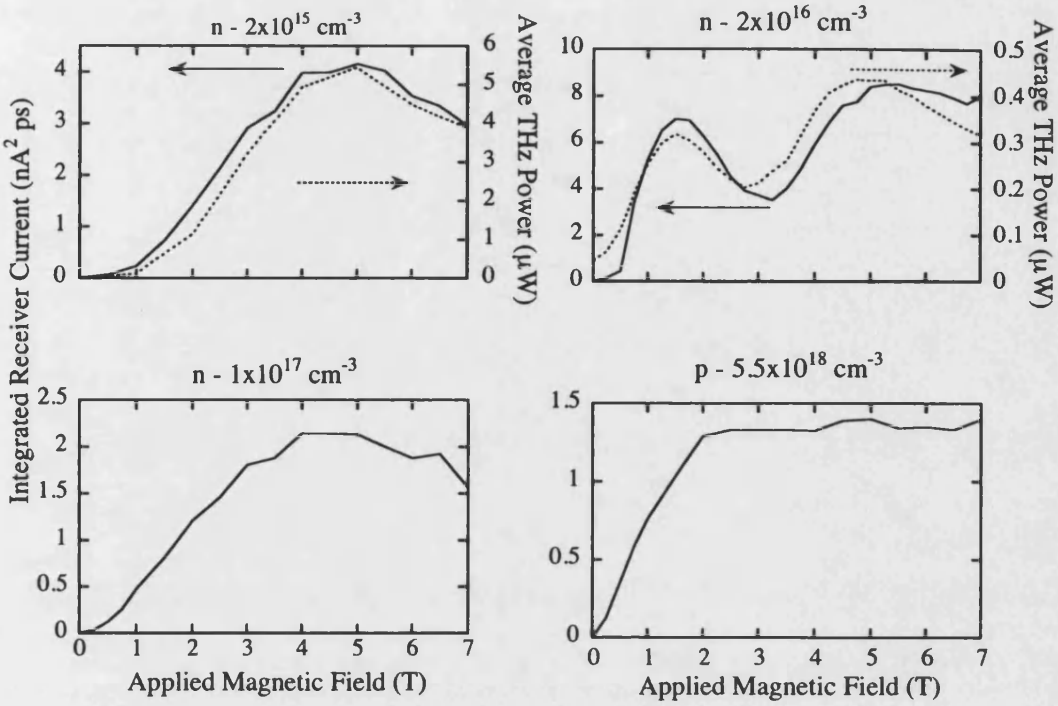

FIGURE 3.17: Integrated receiver current and measured average power for some n-type and p-type InAs samples in s-polarised emission

the large enhancement factor for the samples in the middle of the doping range, there is still a reduction in the overall generated power for an increase in the doping density. Figure 3.19 shows how the average THz power emitted in the p-polarisation, from the n-type InAs samples varies with doping. With zero applied field, the time integrated power varies approximately inversely with the doping concentration. However, with the application of a magnetic field the average power falls off less rapidly at lower doping levels, but then much more rapidly above $\sim 10^{18}\,\mathrm{cm}^{-3}$.

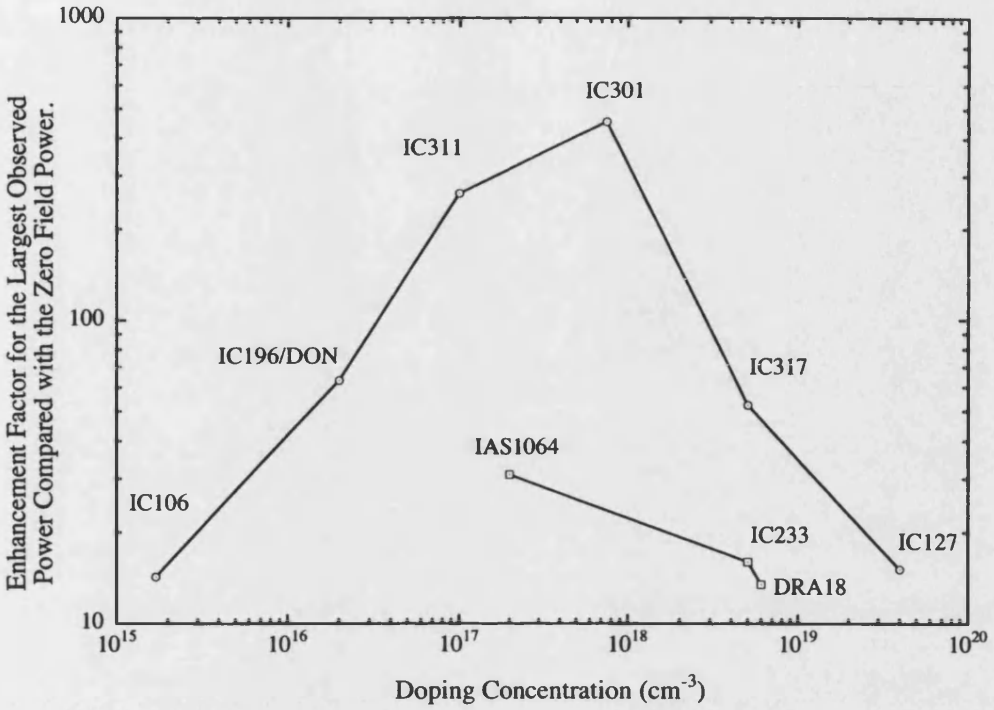

FIGURE 3.18: Power enhancement of the 7 T signal relative to the 0 T.

3.3.4 Coherent Plasma Oscillation Model

To try to develop a more sophisticated model than simply considering the ballistic motion of the charge carriers in crossed electric and magnetic fields, other considerations can be taken into account to try to explain some of the data observed. In this section the screening of the surface accumulation field by photoexcited carriers is accounted for, and this screening produces a driving field which excites cold plasma oscillations of the thermally excited carriers. With this assumption, a model that is essentially an extension of that proposed by Kersting *et al.* [44] to the case of a semiconductor in a magnetic field, is presented. Whilst taking the wide range of different measurements during the study, it was noticed that strong oscillations appeared after the initial transient, with frequencies charac-

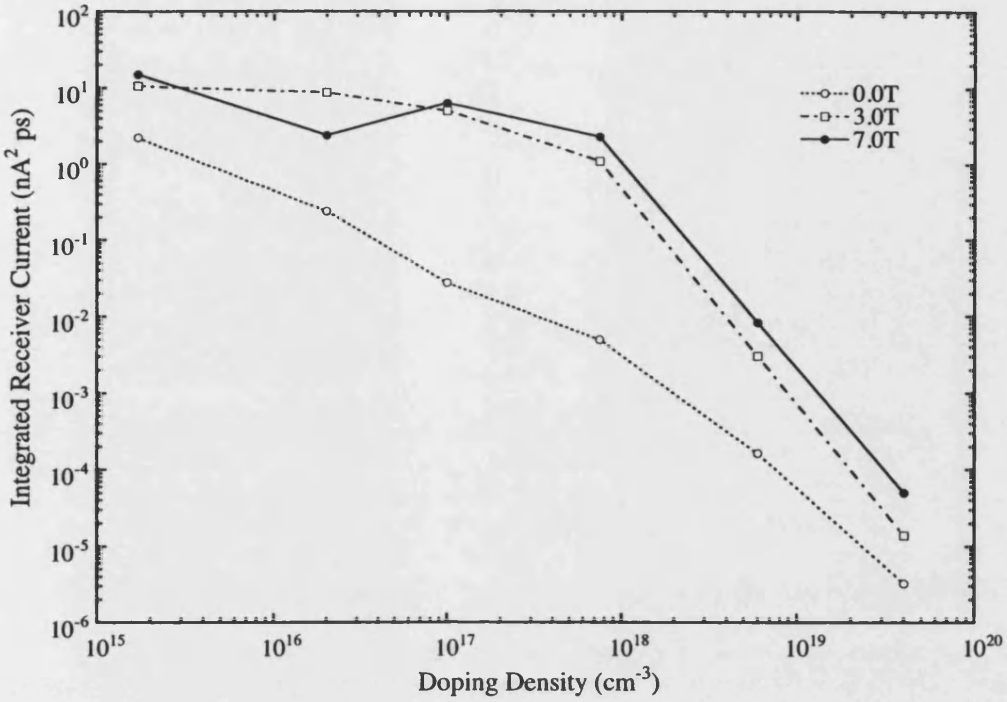

FIGURE 3.19: Integrated receiver current as a function of doping density for the n-type range of samples

teristic of plasma oscillations from the bulk material. Figure 3.20 shows a THz transient and the subsequent plasma oscillations emitted from an n-type sample, with a carrier density of $2\times10^{16}\,\mathrm{cm}^{-3}$, illuminated with near infrared radiation at a wavelength of 765 nm and at a power density of $2{\cdot}5\,\mathrm{W\,cm}^{-2}$. The oscillations have a decay time of less than a picosecond, and are more readily observed at these lower power densities than at the usual power density of $15\,\mathrm{W\,cm}^{-2}$. The fast decay time of less than one picosecond is in good agreement with the scattering times assumed for the ballistic model in the previous section.

It is assumed that the plasma oscillations can be described as a 'slab' of charge [53] with a displacement $\mathbf{x}$ perpendicular to the surface and relative to the crystal

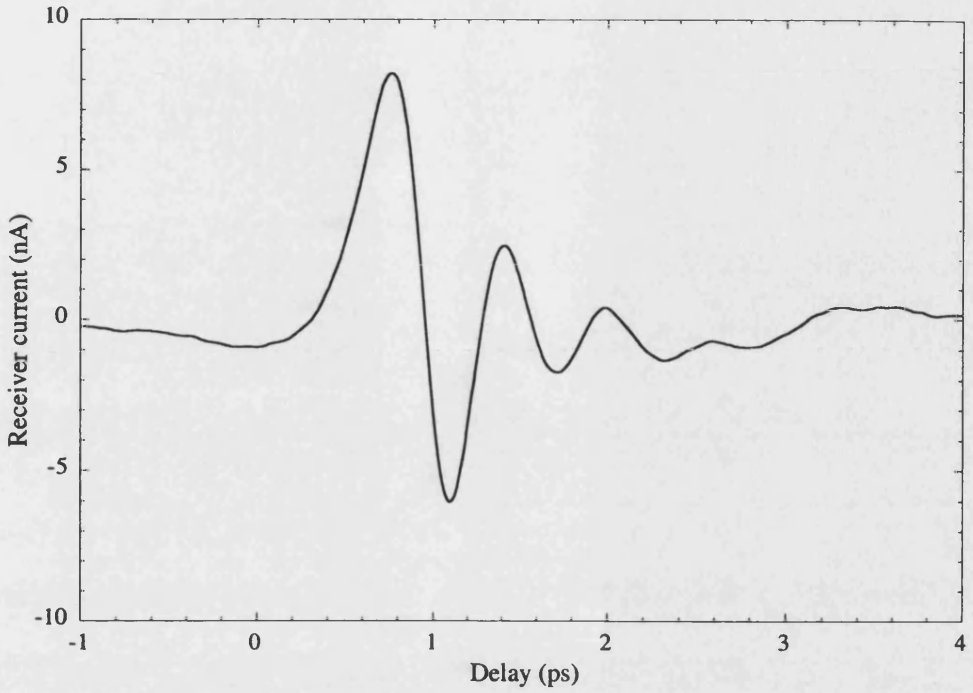

FIGURE 3.20: Bulk plasma oscillations observed from the BK1 n-type sample with a carrier density of $2\times10^{16}\,\mathrm{cm}^{-3}$ illuminated with an average power density of $2{\cdot}5\,\mathrm{W\,cm}^{-2}$ at 765 nm.

lattice. A transient current density can therefore be defined as,

$$\mathbf{j} = -N_s e \frac{\mathrm{d}\mathbf{x}}{\mathrm{d}t} \tag{3.13}$$

where N_s is the free carrier density. For frequencies below those of the optical phonons, the equation of motion of the radiative 'slab' plasmon is [44];

$$\frac{\mathrm{d}^2\mathbf{x}}{\mathrm{d}t^2} + \frac{1}{\tau_s}\frac{\mathrm{d}\mathbf{x}}{\mathrm{d}t} + \omega_p^2\mathbf{x} = \frac{e}{m^*}\left[\mathbf{E}(t) + \left(\frac{\mathrm{d}\mathbf{x}}{\mathrm{d}t} \times \mathbf{B}\right)\right] \tag{3.14}$$

In this equation, the range over which the plasmons are excited is assumed to be equal to the thickness of the epilayer, due to the plasmon wavelengths being

many tens of μm's. This is a valid assumption as the thickness of the epilayers in these samples is in the range $3\,\mu$m to $5\,\mu$m.

Although this model is physically quite different to the model presented in the previous section, Equation 3.14 is mathematically similar to that which is obtained when Equations 3.5-3.7 are solved to give Equation 3.8. The subsequent calculations were performed in a similar manner to that described in the previous section, including taking into account the terms described by Lukosz [48]. However, one change is made, Equation 3.6 is replaced with a phenomenological expression for the time dependent driving field which arises due to the screening in the accumulation layer,

$$E(t) = \Delta E(1 - e^{-t/\tau_e}) \tag{3.15}$$

where ΔE is the maximum change in the surface accumulation field and τ_e is the rise time of the photoexcited carriers [44]. The effect of these two parameters is only to change the absolute power scale, and for this study were assumed to be $10^5\,\mathrm{V\,cm^{-1}}$ and 0·3 ps respectively.

The advantage of this model is that the calculated THz transients have the correct polarity, whilst the magnetic field dependence of the time integrated signals remain similar to those shown earlier. Figure 3.21 shows the p -polarised THz transient traces obtained experimentally for IC106, compared with those predicted by the model with increasing magnetic field from 0 T to 3 T. Figure 3.22 shows the time resolved s-polarised component of the THz emission from IC106 compared with the prediction by the model — the small transient observed at 0 T in the s-polarised trace is considered to arise from polarisation leakage through the wire grid polariser, which has been measured to have a polarisation extinction

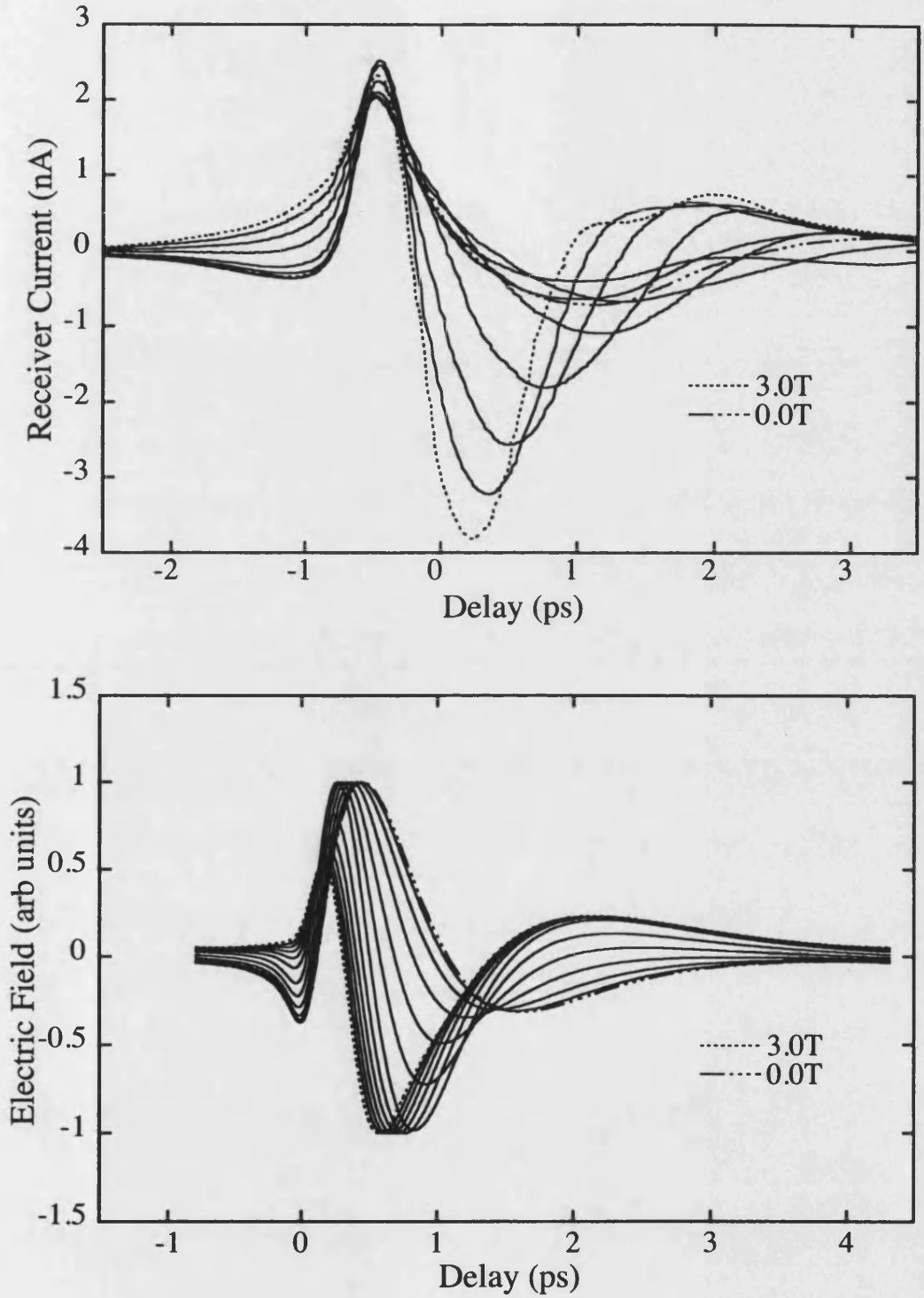

FIGURE 3.21: The p-polarised THz transients observed from IC106 compared with those predicted by the model

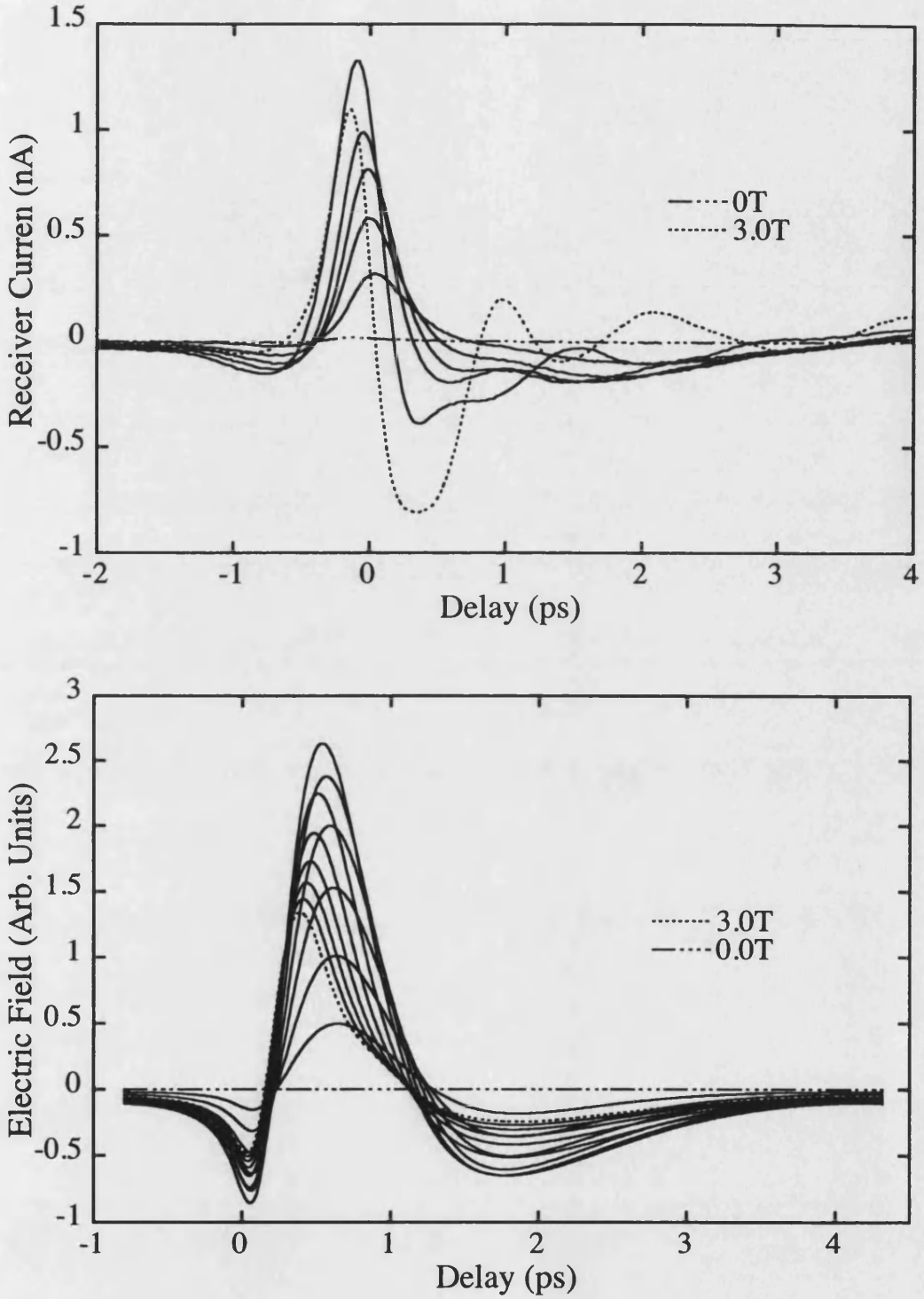

FIGURE 3.22: The s-polarised THz transients observed from IC106 compared with those predicted by the model

ratio of 10%.

This model has also been used to partly describe the zero magnetic field THz emission from n-doped GaAs [44]. However, the model predicts long-lived plasma oscillations that are expected to dominate the THz traces after the initial transient. Unfortunately, these plasma oscillations are not observed, except at low power densities, although there is only one sample with a natural plasma oscillation frequency within the detection bandwidth of the receiver, the sample with a carrier concentration of $2\times10^{16}\,\mathrm{cm}^{-3}$.

It is presumed in this model that the relevant scattering time can be assumed to be similar to that determining the electron mobility, as any electron-electron scattering will not destroy any macroscopic coherence of the plasma. At the low temperatures investigated here ($\leq 30\,\mathrm{K}$), the dominant scattering is by ionised impurities. To obtain good agreement between the predicted and measured THz transient traces, a scattering time of a few hundred femtoseconds is required for the more highly doped samples. Although this time is not expected for the bulk carriers by the inspection of the mobility alone, it is close to that seen in the accumulation layer, and it is possible that the plasmon dephasing time is determined by a coupling between the carriers in the surface accumulation layer and the bulk.

3.3.5 Comparison of the Different Models

The two models that have been presented to propose a mechanism for the generation, and the magnetic field enhancement, of the THz emission from optically excited InAs surfaces show relatively good agreement with the experimental data.

The hypothesis based on the coherent plasma oscillations appears to provide a better model to describe the time domain THz transients, but the more simplistic ballistic model gives similar and relatively good agreement with the experimental data for the time integrated measurements.

An extra feature that may need to be included in the future is to take into account the possible effects of diffusion of the photoexcited charge carriers as another potential mechanism for radiation. A report by Dekorsy *et al.* [54] suggests that a contribution by hot charge carriers can be significant in the emission of high frequency electromagnetic radiation. As has already been mentioned, the radiated electric field is proportional to the acceleration of the transient drift current, $\mathbf{j}$. However, a diffusion current $\mathbf{j}_D$ can be defined as,

$$\mathbf{j}_D = qD(\nabla \cdot N) \tag{3.16}$$

where N is the density of free carriers again, $\nabla(z)$ is the displacement from the surface and D is the diffusion coefficient defined in terms of the carrier temperature T, and the mobility μ,

$$D = \frac{k_B T}{e}\mu \tag{3.17}$$

The photogenerated electrons in InAs are created by a photon energy of 1·65 eV, and the low temperature energy band gap of InAs is 0·42 eV, thus the electrons are excited very high up into the energy band and the term for the carrier temperature is very large. In addition, because of the very large absorption coefficient, $2{\cdot}5\times10^5\,\mathrm{cm}^{-1}$, the partial spatial derivative of N is very large for InAs compared with other materials such as GaAs, where the absorption coefficient at 720 nm is

$4{\cdot}4\times10^4\,\mathrm{cm}^{-1}$ [54].

The diffusion current is therefore dominated by the carrier temperature and mobility along with the spatial dependence of the free carrier density. The temperature for an electron excited to an energy $\sim$1·2 eV above the valence band maximum is $\sim10^4$ K. The current flowing against the surface electric field can therefore be of the same order of magnitude, or larger, as the drift current flowing in the direction of the field when taking into account the high value of $\partial N/\partial z$. In fact the effect has been shown by Dekorsy *et al.* to be important for the subpicosecond carrier transport at GaAs surfaces with space-charge fields, despite the much lower value for the spatial derivative of the carrier density. The effect of the diffusion current on the radiated electric field is to give a large initial transient of the correct polarity, before the large radiative effect of the plasma oscillations, caused by the screening of the surface field by the drift current.

Other features may well need to be incorporated into the model as well, and by examining a range of different GaAs *p-i-n* structures in the future, some insight may be given into the carrier dynamics.

3.4 Variation of the Emitted THz Radiation with Incident Power Density

To investigate the dependence of the generation of the THz radiation in the InAs as a function of the power density of the near infrared pump beam, both the Golay cell and the dipole receiver were used. At very high pump power levels ($\geq$500 mW) the dipole receiver was not used because the full output power of the Ti:sapphire laser was required, hence there was no gating beam available for the receiver. In addition, when the full laser output was used, the dispersion compensation prisms were by-passed, and as such the pulse width will have broadened significantly in time, on passing through the dispersive elements in the optical path. The effect of this dispersion is to reduce somewhat the $f_{0.1}$ bandwidth of the emitted radiation, although this was not measured.

To determine the area of incidence of the pump beam on the samples, a beam profiler was used to measure the radii of the elliptical cross-section of the beam at half power. This measurement was performed with and without the presence of the prisms in the beam path. The lowest power density that was achieved was 0·5 W cm^{-2}, and the highest was $\sim$4 kW cm^{-2}. The measurements were performed with a static applied magnetic field of 3 or 5 T, so as to improve the SNR of the experiment by the enhancement of the generation of the THz radiation.

Initially, the power density of the incident near infrared radiation was changed to investigate the effect on the emitted THz transients. Measurements were made across several decades of increasing power density from $\sim$1 W cm^{-2} up to $\sim$2 kW cm^{-2} by changing both the power of the incident near infrared radiation, and by focusing the area of the incident beam. Two n-type samples (BK1 and

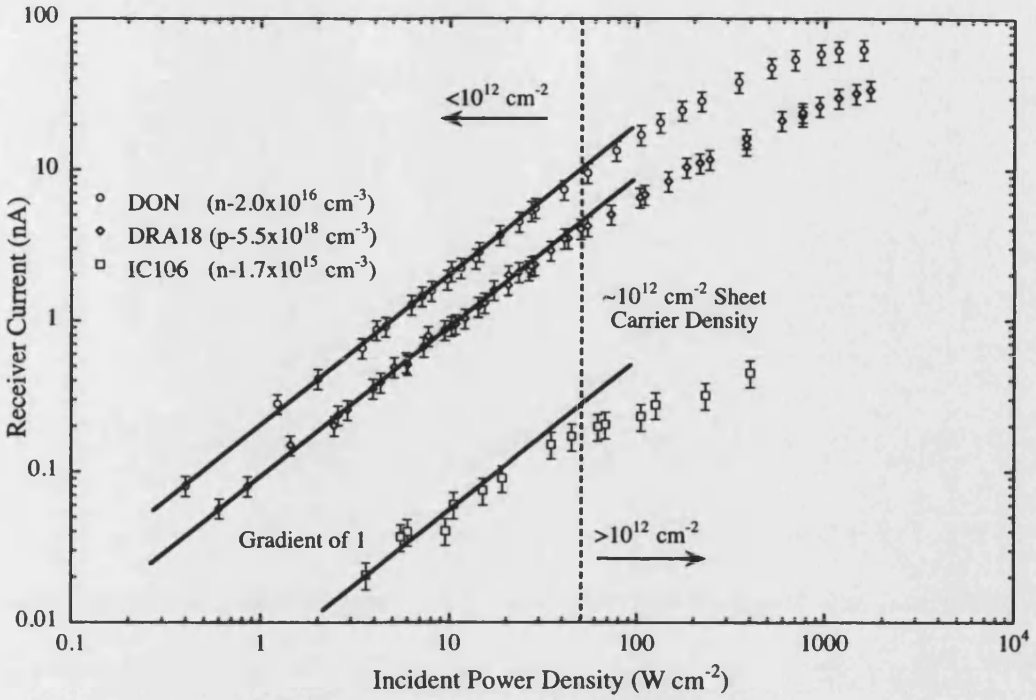

FIGURE 3.23: Plot showing the unitary power relationship between the incident power density and the generated THz radiation, and the subsequent saturation at high incident power densities.

IC106) and one p-type sample (DRA18) were investigated in this way at 30 K and 4 T, so as to increase the amplitude of the transient. Figure 3.23 shows a plot of the peak to peak amplitude of the THz transient as a function of the incident power density for the three samples. At low excitation densities ($\leq$50 W cm^{-2}), the amplitude of the emitted transient is proportional to the incident power, as is expected for coherent radiation; hence the gradient of one that is shown in Figure 3.23. At an average power density of 50 W cm^{-2} and a laser pulse repetition rate of 82 MHz, radiation of wavelength 765 nm creates approximately the same number of carriers as exist in the surface accumulation layer, $\sim 10^{12}$ cm^{-2}. These photoexcited carriers tend to screen the surface electric field, and the THz signal begins to saturate at average power densities in excess of 50 W cm^{-2}. The sample

was kept at a constant temperature of 10 K for the duration of the experiment, however it was found that a reasonable amount of sample heating due to the incident radiation occurred. It was observed that with the standard condition of 360 mW at 765 nm, the sample temperature rose by up to 7 K. The sample was returned to a stable temperature of 10 K before the next datum point was taken.

The Golay cell was used to measure the maximum average power that could be generated in InAs with this measurement system. The maximum average power available from the Ti:sapphire laser was measured to be 1·2 W at the cryostat, and this gave an average power density of 50 W cm^{-2}. Although a much greater power density could have been achieved, the emitted beam is very divergent and large losses are accrued when the pump beam is strongly focussed on to the sample. Figure 3.24 shows the measured average power for the two polarisation components and the sum for this geometry at 13 K as a function of magnetic field. The unpolarised emission of 30 μW is the largest average power observed in this study.

To ensure that any leakage of the wire grid polariser was not responsible for the large value of the sum of the two polarisations, the wire grid polariser was removed and the unpolarised emission measured with the Golay cell. Figure 3.25 shows the comparison of the sum of the two components of emission and the unpolarised emission. Subsequently, by using the TDTS with the CPS transmitter and dipole receiver, the extinction ratio of the polariser was measured more precisely to be 10%±2%.

The effect of changing the power density not only has the effect of saturating the emission at above ~50 W cm^{-2}, but when measuring the power with the Golay cell, the magnetic field at which the emission saturates is shifted to a higher value.

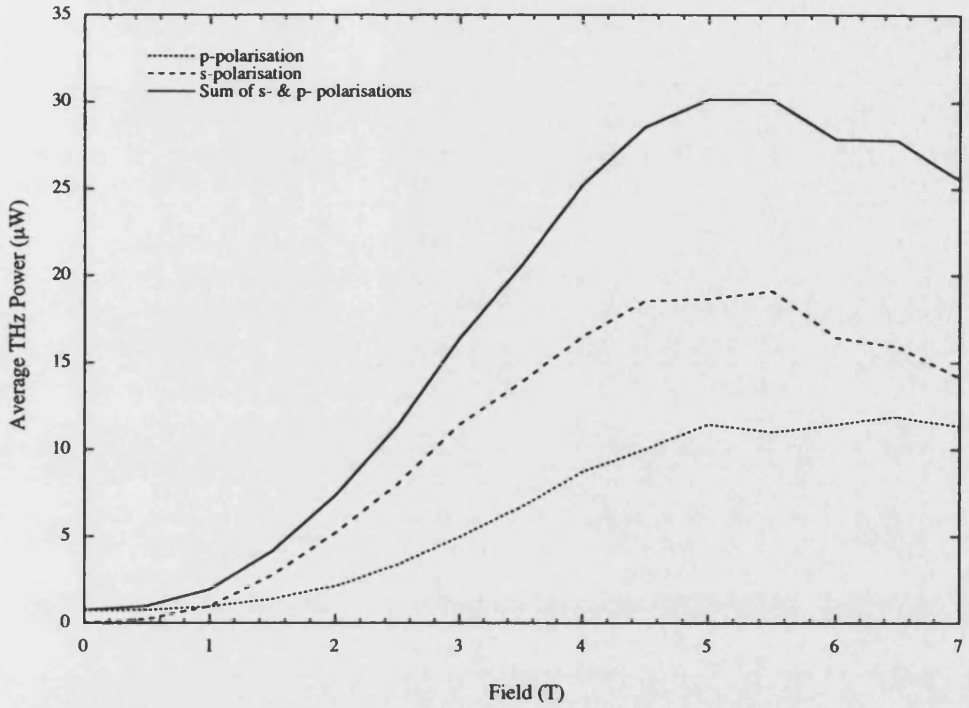

FIGURE 3.24: The maximum average THz power observed from an InAs sample, IC106, for an average pump power of 1.2 W at a temperature of 10 K.

Figure 3.26 shows the results for the n-type sample with a carrier concentration of $1{\cdot}7\times10^{16}\,\mathrm{cm}^{-3}$, at three different power densities. The saturation field for the emission is seen to shift from a value of $\sim$5 T to outside the range of the measurement system by increasing the power density by a factor of $\sim$50. A possible reason for this effect, is that at higher power densities, the density of the photoexcited carriers is increased, which leads to a reduction in the scattering parameter τ_s due to the Coulomb interaction between electrons and holes.

The effect of a decrease in τ_s is to decrease the overall emitted average power, and to shift the saturation field to a higher value. This effect is also seen when the screening parameter η is decreased, which is reasonable when considering higher power densities. The effect of a change in the incident power, but at a constant

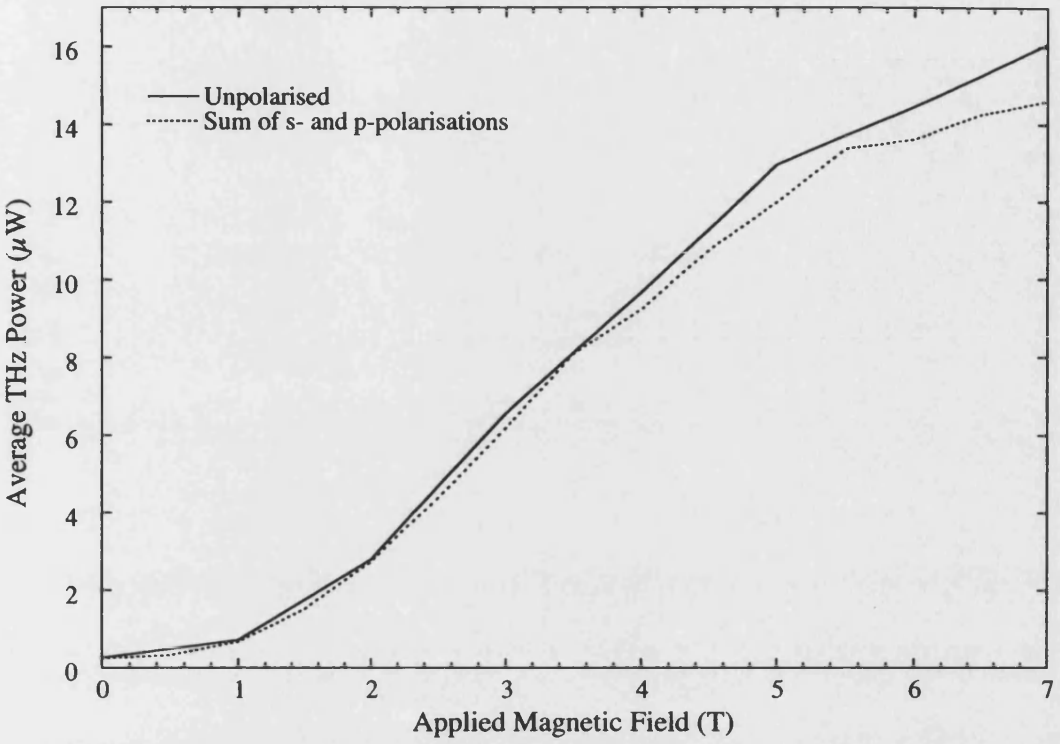

FIGURE 3.25: Unpolarised emission and sum of the two polarisation components for IC106

power density of $30\,\mathrm{W\,cm^{-2}}$ was also studied. In contrast to a change in the magnetic field dependence observed when the power density is changed, the field at which saturation is reached remains the same. The emitted average power at each applied magnetic field value is lower with decreasing incident power, as expected, but ratios of the emitted power at each field value is the same, as shown in Figure 3.27.

3.5 Summary

The THz radiation that is generated in InAs by optical pumping with short pulses has been studied, and the effects of temperature, magnetic field, optical

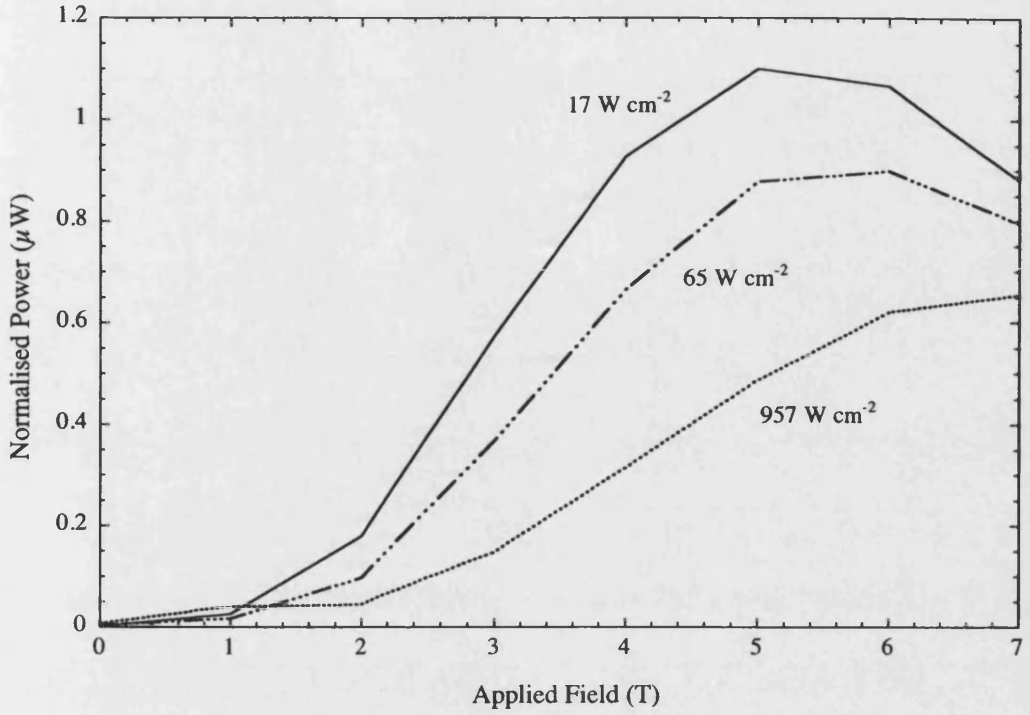

FIGURE 3.26: The magnetic field dependence of an n-type sample at different power densities

pump power, doping density and the majority carrier type have been investigated. Both a bolometric technique, using a Golay cell, and a time resolved coherent detection technique using a dipole receiver in a TDTS system have been used to detect the emitted radiation for the many different conditions of the samples. Two, mathematically similar, but physically different models have been proposed to attempt to assist in the further understanding of the complex origins of the THz radiation, in particular the large enhancement of the emitted power by the application of a magnetic field.

A maximum emitted power of $\sim 30\,\mu$W of unpolarised radiation was observed for the n-type sample with a carrier concentration of $1{\cdot}7 \times 10^{15}\,\mathrm{cm}^{-3}$ at a temperature of 10 K and at a magnetic field strength of 3 T applied at 45° to the sample

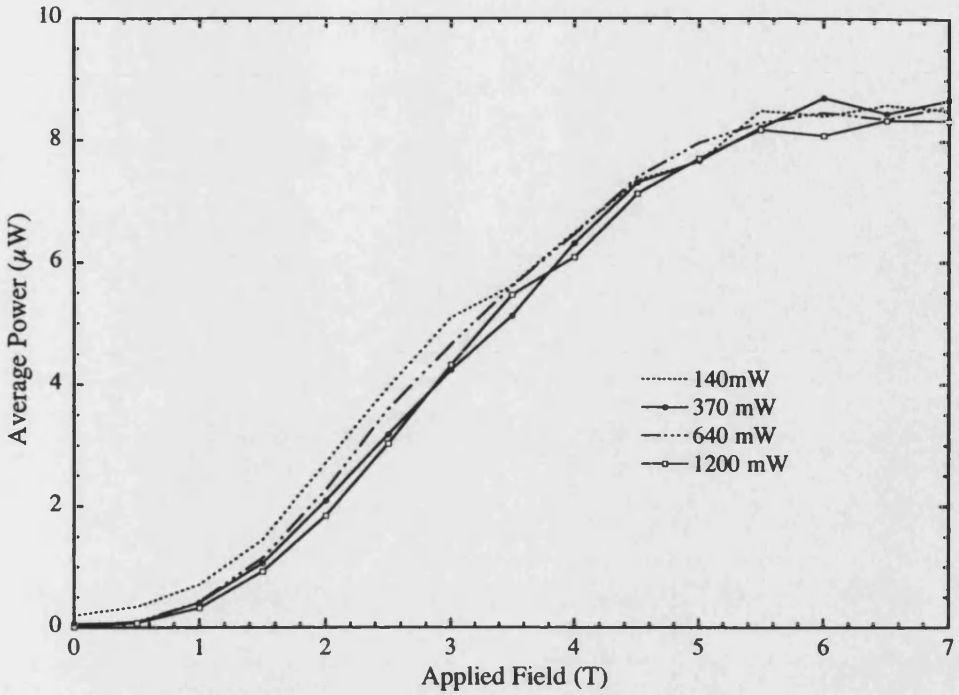

FIGURE 3.27: The magnetic field dependence of an n-type sample at different pump powers, but a constant power density.

surface and the direction of propagation of the incident light. Due to the careful, and multiple, calibrations of the Golay cell sensitivity, this value of $\sim 35\,\mu$W is considered reliable and can be seen to be much smaller than that observed in the first report by Sarukura *etal.* [6].

The motivation for these studies has been to investigate the possible future use of InAs as a coherent THz source. However, the power levels that are generated in InAs are lower than those that can be achieved with a biased CPS transmitter at room temperature and with no applied magnetic field. The power from a CPS transmitter used in the TDTS presented in this thesis, has been measured to in excess of $45\,\mu$W. In addition, a CPS transmitter is a more broad-band THz source than InAs, with the $f_{0.1}$ bandwidth of a CPS transmitter more than

0·5 THz greater.

It is thus the conclusion of this study that InAs offers no obvious advantage over the CPS transmitter, and the use of InAs as a coherent THz source is severely limited.

References

[1] X.-C. Zhang, B.B. Hu *et al.*
'Generation of Femtosecond Electromagnetic Pulses from Semiconductor Surfaces.'
Applied Physics Letters, pp. 1011–1013, **56**(11), 12^{th} March 1990.

[2] X.-C. Zhang, J.T. Darrow *et al.*
'Optically Induced Electromagnetic Radiation from Semiconductor Surfaces.'
Applied Physics Letters, pp. 2228–2230, **56**(22), 28^{th} May 1990.

[3] X.-C. Zhang & D.H. Auston
'Optoelectronic Measurement of Semiconductor Surfaces and Interfaces with Femtosecond Optics.'
Journal of Applied Physics, pp. 326–338, **71**(1), 1^{st} Jan. 1992.

[4] X.-C. Zhang, Y. Jin *et al.*
'Magnetic Switching of THz Beams.'
Applied Physics Letters, pp. 2003–2005, **62**(17), 26^{th} Apr. 1993.

[5] X.-C. Zhang & D.H. Auston
'Optoelectronic Measurement of Semiconductor Surfaces and Interfaces with Femtosecond Optics.'
Journal of Applied Physics, pp. 326–338, **71**(1), 1^{st} Jan. 1992.

[6] N. Sarukura, H. Ohtake *et al.*
'High Average-Power THz Radiation from Femtosecond Laser-Irradiated InAs in a Magnetic Field and its Elliptical Polarization Characteristics.'
Journal of Applied Physics, pp.654–656, **84**(1), 1^{st} July 1998.

[7] S. Izumida, S. Ono, N. Sarukura *et al.*
'Intense THz-Radiation Sources using Semiconductors Irradiated with Femtosecond Laser Pulses in a Magnetic Field.'
Journal of Nonlinear Optical Physics & Materials, pp. 71–87, **8**(1), 1999.

[8] R. McLaughlin, A. Corchia *et al.*
'Enhanced Coherent Terahertz Emission from Indium Arsenide in the Presence of a Magnetic Field.'
Applied Physics Letters, pp. 2038–2040, **76**(15), 10th April 2000.

[9] G. Meinert, L. Bányai *et al.*
'Theory of THz Emission from Optically Excited Semiconductors in Crossed Electric and Magnetic Fields.'
Physical Review — B, pp. 5003–5009, **62**(8), 15th Aug. 2000.

[10] J. Shan, C. Weiss *et al.*
'Origin of Magnetic Field Enhancement in the Generation of Terahertz Radiation from Semiconductor Surfaces.'
Optics Letters, pp. 849–851, **26**(11), June 2001.

[11] C. Weiss, R. Wallenstein *et al.*
'Magnetic Field Enhanced Generation of Terahertz Radiation in Semiconductor Surfaces.'
Applied Physics Letters, pp. 4160–4162, **77**(25), 18th Dec. 2000.

[12] Z. Liu, S. Ono, N. Sarukura *et al.*
'Efficient Terahertz Radiation Generation from a Bulk InAs Mirror as an Intracavity Terahertz Radiation Emitter.'
Japanese Journal of Applied Physics, pp. L366–L367, **39**, Part 2, No. 4B, 15th Apr. 2000.

[13] S. Ono, T. Tsukamoto, N. Sarukura *et al.*
'Compact THz-Radiation Source Consisting of a bulk Semiconductor, a Mode-Locked Fiber Laser, and a 2T Permanent Magnet.'
Review of Scientific Instruments, pp. 554–556, **71**(2), Feb. 2000.

[14] T. Kondo, M. Sakamoto *et al.*
'Terahertz Radiation from ⟨111⟩ InAs Surface using 1·55 μm Femtosecond Laser Pulses.'
Japanese Journal of Applied Physics, pp. L1035–L1037, **38**, Part 2, No. 9A/B, 15th Sep. 1999.

[15] C.A. Mead & W.G. Spitzer,
'Fermi Level Position at Semiconductor Surfaces.'
Physical Review Letters, pp. 471–472, **10**(11), 1st June 1963.

[16] H.-U. Baier, L. Koenders & W. Mönch
'Oxidation of Cleaved InAs(110) Surfaces at Room Temperature: Surface Band-Bending and Ionization Energy.'
Solid State Communications, pp. 327–331, **58**(5), 1986.

[17] H. Yamaguchi & Y. Horikoshi
'Surface-Defect Formation on Heavily Doped InAs and GaAs Layers Studied by Scanning Tunnelling Microscopy.'
Physical Review B, pp.4565–4569, **53**(8), 15th Feb. 1996;
E. Yamaguchi
'Electron Subbands and Transport Properties in Inversion Layers of InAs and InP.'
Physical Review B, pp. 5280–5288, **32**(8), 15th Oct. 1985.

[18] V.Yu. Aristov, G. Le Lay *et al.*
'Giant Band-Bending Induced by Ag on InAs(110) Surfaces at Low Temperature.'
Physical Review B, pp. 2138–2145, **47**(4), Jan. 1993.

[19] L.Ö. Olsson, M.C. Håkansson *et al.*
'Charge Accumulation at InAs Surfaces.'
Physical Review Letters, pp. 3626–3629, **76**(19), 6th May 1996.

[20] D.C. Tsui
'Landau-Level Spectra of Conduction Electrons at an InAs Surface.'
Physical Review B, pp. 5739–5748, **12**(12), 15th Dec. 1975.

[21] Y. Chen, J.C. Hermanson *et al.*
'Coupled Plasmon and Phonon in the Accumulation Layer of InAs(110) Cleaved Surfaces.'
Physical Review — B, pp. 12 682–12 687, **39**(17) 15th June 1989.

[22] H. Reisinger & F. Koch
'Spectroscopy of InAs Subbands.'
Solid State Communications, pp. 429–431, **37**, 1981.

[23] C.B.M. Andersson, J.N. Andersen *et al.*
'Bulk and Surface Electronic Structure of InAs(110).'
Surface Science, pp. 395–406, **398**, 1998.

[24] S.G. Lachenmann, Th. Schäpers *et al.*
'Suppression of the Surface-Inversion Layer of p-type InAs.'
Journal of Applied Physics, pp. 8242–8246, **85**(12), 15th June 1999.

[25] J.R. Sites & H.H. Wieder
'Surface and Bulk Charge Carrier Transport in InAs Epilayers.'
CRC Critical Reviews in Solid State Sciences, pp. 385–389, Oct. 1975.

[26] H.A. Washburn *et al.*
'Electronic Profile of n-InAs on Semi-Insulating GaAs.'
Journal of Applied Physics, pp. 4872–4878, **50**(7), July 1979.

[27] H.S. Kärlsson, R. Viselga & U.O. Karlsson
'Electron Accumulation at the InAs(110) Cleavage Surface.'
Surface Science, pp. L687–L692, **407**, 1998.

[28] L. Canali, J.W.G. Wildöer *et al.*
'Low Temperature STM on InAs(110) Accumulation Surfaces.'
Applied Physics A, pp. S113–S116, **66**, 1998.

[29] P.D. Wang, S.N. Holmes *et al.*
'Electrical and Magneto-Optical Studies of MBE InAs on GaAs.'
Semiconductor Science and Technology, pp. 767–786, **7**, 1992.

[30] V.A. Skripkin, V.N. Lange & B.P. Kotrubenko
'Effective Electron Mass in Strongly Doped InAs.'
Translated from: Izvestiya Vysshikh Uchebnykh Zavedenii Fizika, pp. 140–143, **1**, Jan. 1973.

[31] Z.V. Chizhova, R.A. Radchenko & I.I. Taubkin
'Absorption Coefficient of n-Type Indium Arsenide at Various Doping Levels.'
Soviet Physics — Semiconductors, pp. 792–794, **4**(5), Nov. 1970.

[32] Landolt-Börnstein
'Physics of Group IV Elements and III-V Compounds.'
Springer-Verlag, Berlin, Volume 17(a)
ISBN: 0387106103

[33] Y.B. Li, R.A. Stradling *et al.*
'Infrared Reflection and Transmission of Undoped and Si-Doped InAs Grown on GaAs by Molecular Beam Epitaxy.'
Semiconductor Science and Technology, pp. 101–111, **8**, 1993.

[34] C.C. Phillips, Y.B. Li *et al.*
'Picosecond Saturable Absorption Measurements on Thin Film Single-Crystal InAs Layers Grown by MBE.'
Journal of Physics **D** : Applied Physics, pp. 437–440, **24**, 1991.;
K.L. Vodopyanov, C.C. Phillips *et al.*
'Extrinsic Recombination Processes in proton Irradiated InAs/GaAs Heterostructures Grown by Molecular Beam Epitaxy'
Journal of Applied Physics, pp. 627–632, **73**(2), 15^{th} Jan. 1993.

[35] K.L. Vodopyanov, C.C. Phillips *et al.*
'Picosecond Carrier Dynamics and Studies of Auger Recombination Processes in Indium Arsenide at Room Temperature.'
Physical Review **B**, pp. 13194–13200, **46**(20), 15^{th} Nov. 1992.

[36] M. Noguchi, K. Hirakawa *et al.*
'Intrinsic Electron Accumulation layers on Reconstructed Clean InAs⟨100⟩ Surfaces.'
Physical Review Letters, pp.2243–2246, **66**, No.17, 29^{th} Apr. 1991.

[37] R.E. Williams
'GaAs Processing Techniques.'
Artech House Publishers, NY, 1990
ISBN: 0890063435

[38] H. Oigawa, J-F. Fan *et al.*
'Universal Passivation Effect of $(NH_4)_2S$ Treatment on the Surface of III–V Compound Semiconductors.'
Japanese Journal of Applied Physics, pp. L322–L325, **30**(3A), Mar. 1991.

[39] I.A. Fomin, L.V. Lebedeva *et al.*
'Investigation of the Carrier Lifetime in Epitaxial n-Type InAs.'
Soviet Physics — Semiconductors, pp. 851–852, **14**(7), July 1980.

[40] R. M^{c}Laughlin, Q. Chen *et al.*
'Enhanced Coherent Terahertz Emission from Indium Arsenide.'
Journal of Modern Optics, pp. 1847–1856, **47**(11), 2000.

[41] H. Ohtake, S. Ono *et al.*
'Enhanced THz Radiation from Femtosecond Laser Pulse Irradiated InAs Clean Surface.'
Japanese Journal of Applied Physics, pp. L1186–L1187, **38**, 1999.

[42] S. Kono, P. Gu *et al.*
'Temperature Dependence of Terahertz Radiation from n-type InSb and n-type Surfaces.'
Applied Physics B, Rapid Communication, pp. 901–904, **71**, 2000.

[43] H. Ohtake, S. Ono, N. Sarukura *et al.*
'Saturation of THz-Radiation Power from Femtosecond-Laser-Irradiated InAs in a High Magnetic Field.'
Applied Physics Letters, pp. 1398–1400, **76**(11), 13^{th} March 2000.

[44] R. Kersting, J.N. Heyman *et al.*
'Coherent Plasmons in n-doped GaAs.'
Physical Review B, pp. 4553–4559, **58**(8), Aug. 1998.

[45] P. Uhd-Jepsen, R.H. Jacobsen *et al.*
'Generation and Detection of THz pulses from Biased Semiconducting Antennas.'
Journal of the Optical Society of America B — Optical Physics, pp.2424–2436, **B 13**(11), Nov. 1996.

[46] K.L. Sala, G.A. Kenney-Wallace *et al.*
'CW Autocorrelation Measurements of Picosecond Laser Pulses.'
IEEE Journal of Quantum Electronics, pp.990-996 **QE-16**(9), Sept. 1980

[47] Peter Y. Yu, Manuel Cardona
'Fundamentals of Semiconductors — Physics and Materials Properties.'
Springer-Verlag, Berlin, 1996.
ISBN: 3–540–58307–6

[48] W. Lukosz & R.E. Kunz
'Light Emission by Magnetic and Electric Dipoles Close to a Plane Interface. I. Total Radiated Power.'
Journal of the Optical Society of America, pp. 1607–1614, **67**(12) Dec. 1977.
W. Lukosz & R.E. Kunz
'Light Emission by Magnetic and Electric Dipoles Close to a Plane Interface. II. Radiation Patterns of Perpendicular Oriented Dipoles.'
Journal of the Optical Society of America, pp. 1615–1619, **67**(12) Dec. 1977.
W. Lukosz
'Light Emission by Magnetic and Electric Dipoles Close to a Plane Interface. III. Radiation Patterns of Dipoles with Arbitrary Orientation.'
Journal of the Optical Society of America, pp. 1495–1503, **69**(11) Nov. 1979.

[49] H.A. Washburn
'Multilayer Model of Indium Arsenide.'
Thin Solid Films, pp. 135–140, **45**, 1977.

[50] H.J. Lee & Y.S. Park
'Semi-Insulating GaAs Examined Using a Three-Band Model.'
Journal of Applied Physics, pp. 402–405, **55**(2), Jan. 1984.

[51] Calculations performed by Dr. S.R. Andrews of the University of Bath.

[52] R.P. Howson & V. Malina
'Related optical and Electrical Properties of Thin Films of Indium Arsenide.'
Journal of Physics D : Applied Physics, pp. 854–862, **3**,1970.

[53] K. Victor, H.G. Roskos & C. Waschke
'Efficiency os Submillimetre-Wave Generation and Amplification by Coherent Wave-Packet Oscillations in Semiconductor Structures.'
Journal of the Optical Society of America B, pp. 2470–2479, **11**(12) Dec. 1994.

[54] T. Dekorsy, T. Pfeifer *et al.*
'Subpicosecond Carrier Transport in GaAs Surface-Space-Charge Fields.'
Physical Review B, pp. 3842–3849, **47**(7), Feb. 1993.

Chapter 4

THz Cyclotron Resonance in Optically Excited High Resistivity Silicon

4.1 Introduction

In this chapter, a description of the investigation into the origins of the oscillations mentioned previously in Chapter 3 is presented. The long lived oscillations were observed in the time domain traces whilst measuring the emission of THz radiation from optically excited InAs in a magnetic field. The oscillations were originally thought to be a feature of the InAs samples themselves. In the exploration of this hypothesis several experiments were performed, including investigations into the dependence of the frequency and amplitude of the oscillations as a function of the sample doping, the magnetic field dependence, the orientation of the sample to the magnetic field, the temperature dependence and a 'double-pump' single probe experiment using the coplanar stripline (CPS) transmitter. Despite the large variation in the experiments, the same frequencies for the oscillations were found. It was subsequently discovered that the oscillations were

due to the absorption of the THz radiation by the electron cyclotron resonance in the silicon 'cold window' of the cryostat.

Once the origins of the oscillations had been discovered, experiments were performed using an InAs sample as a source of coherent THz radiation to probe the cyclotron resonance in the high resistivity ($\varrho \geq 10^4\,\Omega\,\mathrm{cm}$ at 300 K) ⟨100⟩ silicon windows. Although there is one previous publication on the use of optically excited InAs as a THz source [1], this is believed to be be the first reported use of optically excited InAs to provide coherent THz emission for pump-probe spectroscopy on an optically excited material. Initially the magnetic field dependence of the cyclotron resonance was investigated to determine the carriers involved, and then the incident power density dependence was studied to confirm the process was absorption. Finally the temperature dependence of the cyclotron resonance was measured over the range 5 K to 80 K.

Cyclotron resonance in semiconductors was first observed in Germanium at 77 K by Dresselhaus *et al.* in 1953 [2]. The experiment was based on the suggestion of the possible application of cyclotron resonance to solids by Dorfmann in 1951 [3], and the work by Dingle in 1952 [4] when he proposed the quantum theory of cyclotron resonance of a free particle. It was not until 1953, however, that Shockley [5] gave a solution to the problem of cyclotron resonance for an ellipsoidal energy surface — as is the case in both silicon and germanium. Dresselhaus *et al.* reported the first observation of cyclotron resonance in silicon [6] and germanium [7], at a temperature close to 4 K, the characteristics of which were explained in terms of the model proposed by Shockley [5].

Since these early reports, cyclotron resonance has been used extensively to investigate properties of materials. In particular the effective mass of carriers involved

in the cyclotron motion and to estimate a lower limit for the carrier scattering time from the homogenous broadening of the observed resonance peaks [8]. The measurement of the cyclotron resonance effect was also the first method by which the effective mass of carriers could be determined directly [9], and as such proved to be a very powerful tool in the study of solid state materials, in particular semiconductors[10].

The separate components of the TDTS (time domain terahertz spectrometer), which was used to measure cyclotron resonance in silicon, are discussed fully in Chapter 2 and the characteristics of the InAs sample used as the THz source is discussed in Chapter 3. The experimental configuration used was the same as that shown in Figure 3.1 in Chapter 3, where the InAs sample used to generate the THz radiation was the n-type sample designated as BK1 in Table 2.1, which was illuminated by near infrared radiation of wavelength 765 nm, with an average power of 360 mW at the sample surface, with the sample surface at 45° to both the incident light and the axis of the magnetic field. The cold exit window of the cryostat was used as the silicon sample. A fraction of the near infrared light was reflected from the InAs surface onto the silicon window, thus creating electron hole pairs in the window, crucially along the axis of emission of the THz radiation from the InAs sample. The use of the optically excited InAs as a source for the THz radiation overcomes one of the difficulties in using the TDTS in the usual optical pump, THz probe configuration, that of aligning the optical pump and the far infrared probe beams such that they are colinear within the sample.

4.1.1 Properties of Silicon

The properties of silicon have been studied extensively in the past, and today silicon is one of the most well understood materials [11]. Much of the work performed to further the understanding of the properties of silicon was stimulated by the electronics industry [12, 13]. The need to increase the density of transistors on silicon chips [14], the fabrication of different types of transistor [15] and other devices [16] all resulted in the need for more information about the material. Silicon and germanium were studied extensively from the 1930's onwards, but it wasn't until the late 1940's and early 1950's that single crystals of sufficient purity were able to be fabricated [17]. The growth of pure crystals of these group IV elements enabled their semiconducting properties to be investigated, without domination of the observed processes by impurities.

Silicon forms a diamond structure unit cell with each atom tetrahedrally surrounded by four nearest neighbours, and is an indirect band gap material with a minimum energy band gap of 1·15 eV at 4·2 K [18]. The constant energy surfaces at the bottom of the conduction band are located on the orthogonal ⟨100⟩ axes, as shown in Figure 4.1. The electrons in silicon are distributed amongst the six equivalent energy valleys; the so-called 'many-valley' model [9]. This is in stark contrast to the direct band gap materials such as GaAs, where the constant energy surface is a sphere located at the centre of the Brillouin zone [19]. It can be shown that the effective mass is isotropic for the spheroidal energy surface and that the effective mass tensor can be expressed as [20];

$$\frac{1}{m_{xy}} = \frac{1}{\hbar^2}\frac{\partial^2 E(k)}{\partial k_x \partial k_y} \tag{4.1}$$

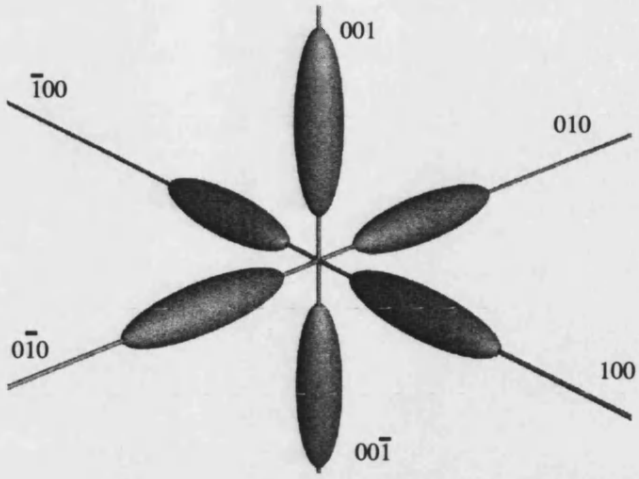

FIGURE 4.1: The ellipsoidal constant energy surfaces for silicon.

In silicon, however, the electron effective mass is anisotropic because the constant energy surface is ellipsoidal [9];

$$E(k) = \hbar \left[\frac{(k_x - k_{0x})^2 + (k_y - k_{0y})^2}{2m_\perp} + \frac{(k_z - k_{0z})^2}{2m_\parallel} \right] \tag{4.2}$$

where the x- and y-axes are defined as the minor (transverse) axis of the ellipsoid and the major (longitudinal) axis respectively. The band edge exists at intermediate points $k_{0x,y,z}$ along the $\langle 100 \rangle$ axes of the Brillouin zone. The electron effective masses defined as the transverse effective mass, $m_\perp$, and the longitudinal effective mass, $m_\parallel$, correspond to the effective mass of an electron travelling along the minor and major axes of the ellipsoid respectively. Only in the transverse direction is the electron effective mass found to be isotropic.

The presence of the anisotropy of the electron effective mass is especially important to note in the experiments presented in this chapter, because of the direct way in which the carrier effective mass is determined by cyclotron resonance experiments. With reference to Figure 4.1, it can be seen that the application of a

magnetic field along, say, a particular ⟨100⟩ axis results in two cyclotron frequencies. It is also clear that there will be a dependence of the observed frequencies on the angle, θ, of the application of the magnetic field to the ⟨100⟩ crystallographic axes. The observed cyclotron frequency can be expressed as [9];

$$\omega_c^2 = \omega_\perp^2 \cos^2\theta + \omega_\perp \omega_\parallel \sin^2\theta \tag{4.3}$$

and thus the observed effective mass is,

$$\frac{1}{m^{*2}} = \frac{\cos^2\theta}{m_\perp^2} + \frac{sin^2\theta}{m_\perp m_\parallel} \tag{4.4}$$

4.2 Experimental Results

Figure 4.2 shows an example of the cyclotron oscillations that appear after the main THz transient in the *s*-polarised emission from the *n*-type InAs sample BK1 (n-$2{\cdot}10^{16}\,cm^{-3}$) under a magnetic field of 5 T. As can be seen the oscillations extend just beyond 30 ps after the main THz transient, and the peak to peak amplitude of the oscillations at the maximum is 0·35 nA compared with the main transient amplitude of ~7 nA. By integrating over time the intensity of the oscillations and the main transient separately, a value for the relative powers can be calculated. It is found that the power in the oscillations is equivalent to 5% of that contained within the main transient. An FFT was performed on the data to extract the frequency of the oscillations, as shown in Figure 4.3. Two distinct absorption features occur at ~0·34 THz and ~0·74 THz. The linewidth taken from the FFT was used to calculate a $1/e$ decay time for the oscillations of ~22 ps.

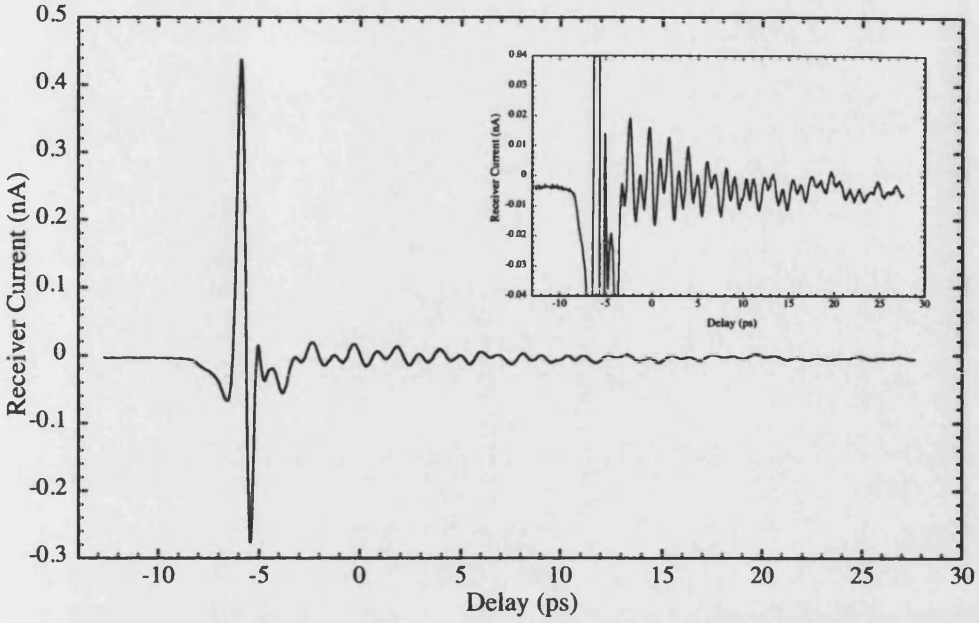

FIGURE 4.2: The long lived oscillations present in the p-polarised component of the detected electric field transient. The transient shows a closeup of the oscillations to outline the exponential decay.

4.2.1 Magnetic Field Dependence

The oscillations were measured at various applied magnetic field strengths as shown in Figure 4.4(a), together with the associated FFT's for a range of magnetic fields from 0 T to 7 T. It is clear that the frequencies associated with the absorption increase with increasing magnetic field. The linear relationship between the absorption frequency and magnetic field, shown in Figure 4.5 suggests cyclotron resonance of carriers with masses of $0{\cdot}19m_e$ and $0{\cdot}41m_e$.

From Equation 4.4 it can be deduced that the 45° experimental geometry results in the predicted masses of $m_\perp$=$0{\cdot}19m_e$ and $\sqrt{m_\parallel m_\perp}$=$0{\cdot}41m_e$, thus the longitudinal mass is found to be $m_\parallel$=$0{\cdot}90m_e$. These values give good agreement when compared with the published data [21] and so it is concluded that the oscillations

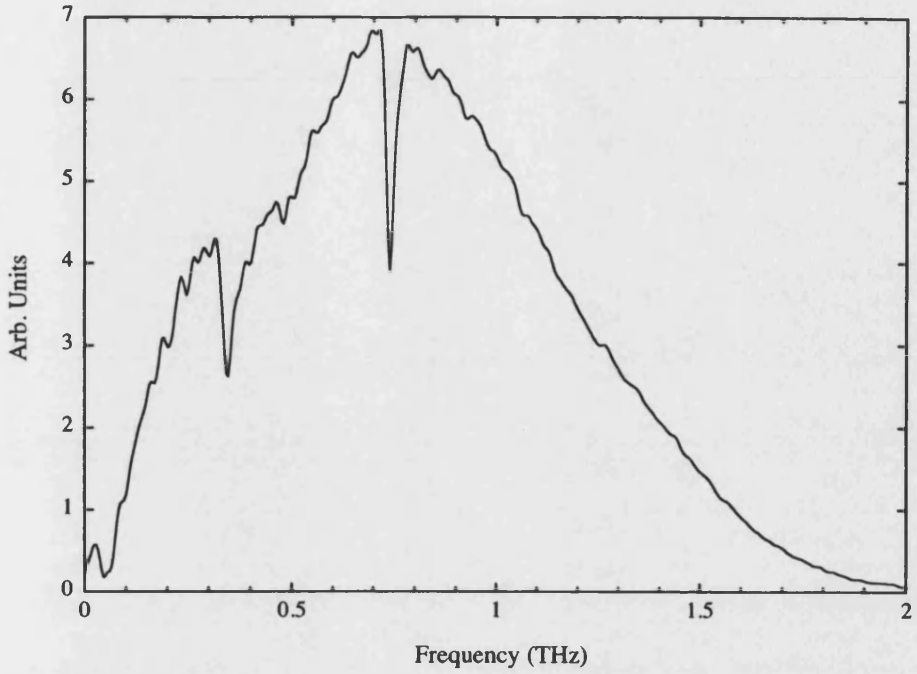

FIGURE 4.3: Fourier transform of the time domain trace shown in Figure 4.2. The two frequencies that are absent from the spectrum are ~0·34 THz and ~0·74 THz.

are a feature of the cyclotron motion of the electrons in high resistivity silicon.

4.2.2 Power Density Dependence

To determine that the detected cyclotron resonance was an absorption feature, the power density of the incident near infrared pump beam was changed to observe how the amplitude of the oscillations changed. In this experimental geometry, the amplitude of the THz radiation emitted from the InAs sample is proportional to the average power density of the incident near infrared radiation, and so is the number of photoexcited free carriers created in the silicon. For an absorption process, the amplitude of the oscillations is therefore proportional to the square

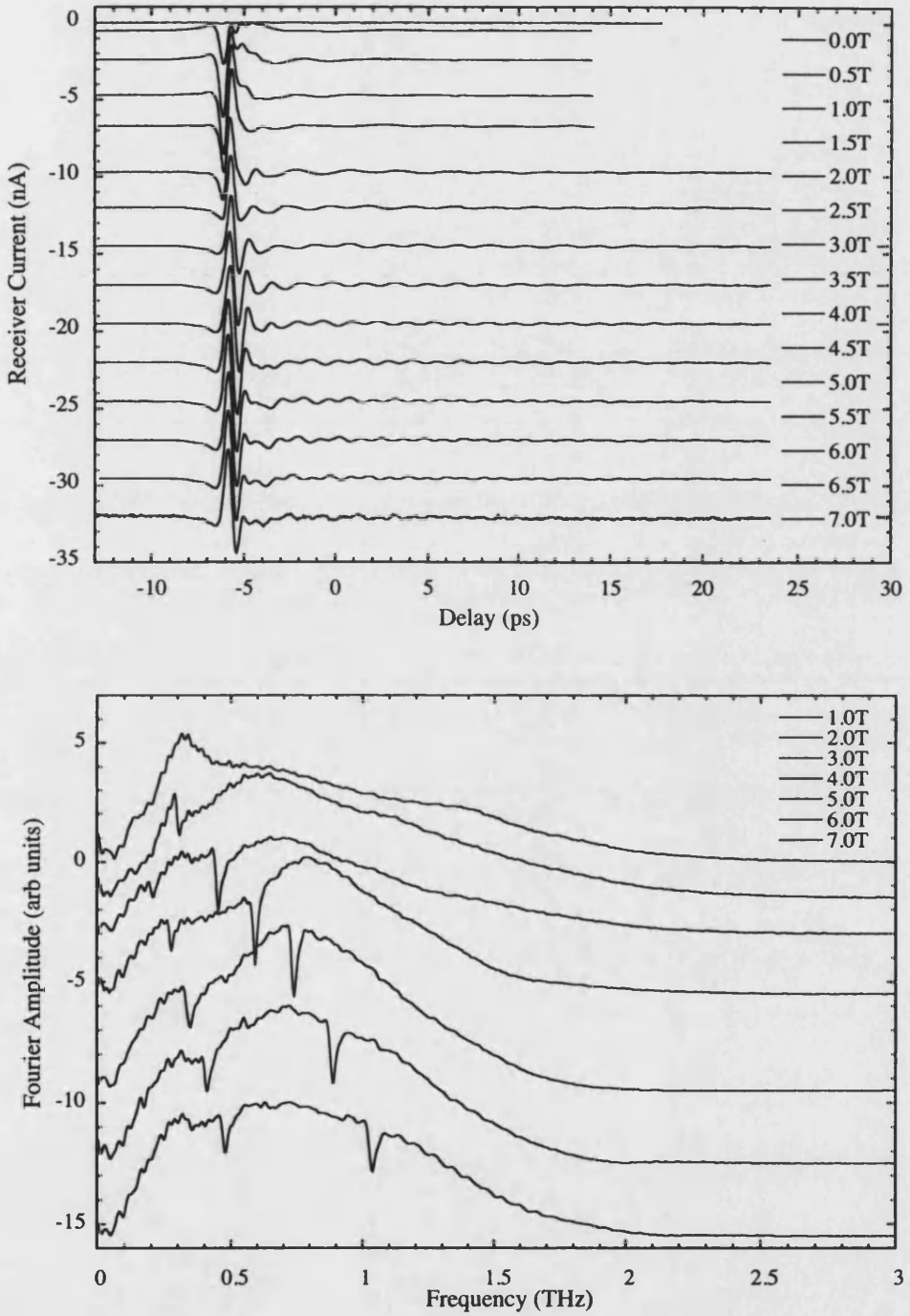

FIGURE 4.4: The magnetic field dependence of the oscillations (top) showing the two frequency components, and the associated Fourier transforms (bottom), showing the absorption features.

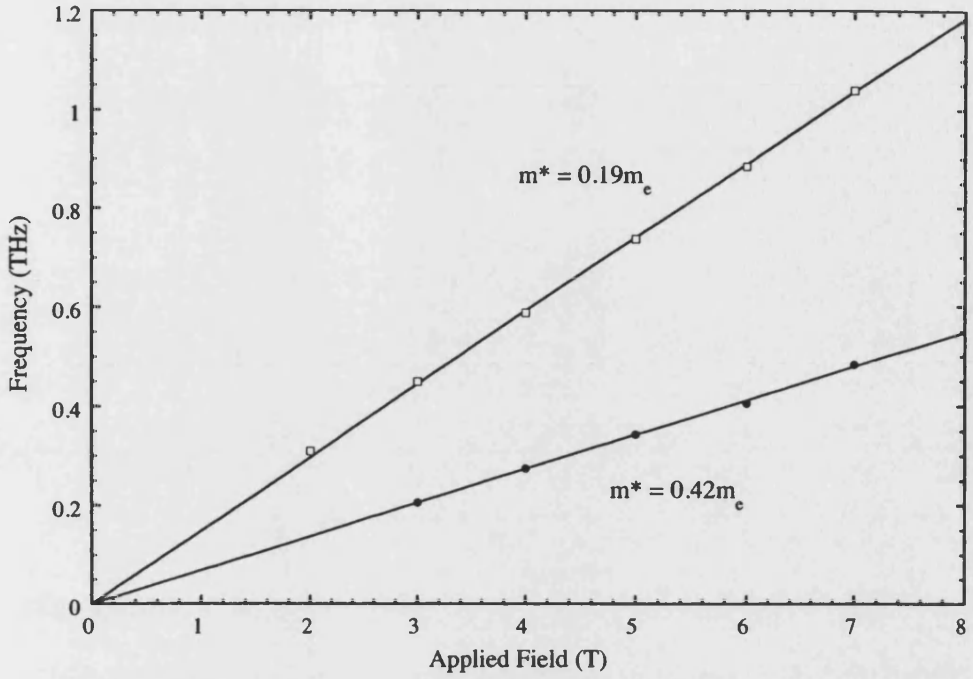

FIGURE 4.5: Absorption frequencies at different magnetic fields, together with a fit using $\omega_c = eB/m_e^*$

of the incident average power density of the near infrared radiation. By performing an experiment where the incident power density was increased over several decades, including into the regime where the THz emission is saturated, with a static magnetic field, the amplitude of the initial transient and the oscillations could be recorded. Figure 4.6 shows the result of this experiment, and there is evidence to support the idea that the oscillations arise due to cyclotron absorption of the THz radiation emitted by the InAs sample.

4.2.3 Temperature Dependence

The temperature dependence of optically excited cyclotron resonance in silicon was studied between 5 K and 80 K. Figure 4.7 shows the measured temperature

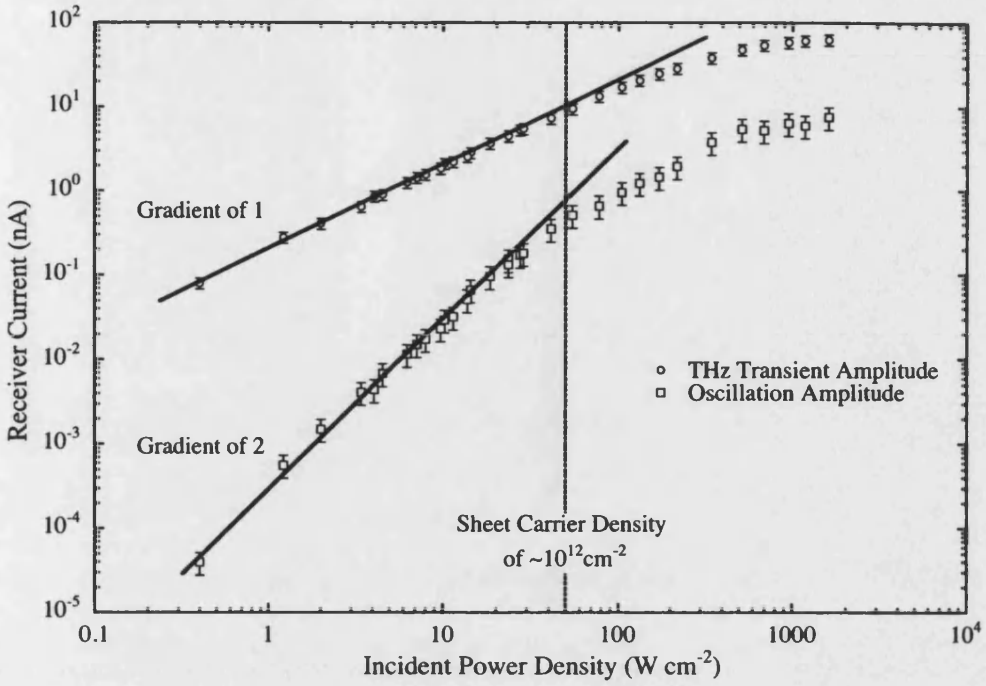

FIGURE 4.6: Plot to show the peak to peak amplitude of the main THz electric field transient and the peak to peak amplitude of the oscillations, as a function of the pump beam power density.

dependence for the cyclotron oscillation amplitude for three different power densities of $15\,\mathrm{W\,cm^{-2}}$, $74\,\mathrm{W\,cm^{-2}}$ and $227\,\mathrm{W\,cm^{-2}}$ of the near infrared radiation pump beam.

Above the peak at ~30 K the dominant electron scattering process is the interaction of the electrons with the acoustic phonons [22], and at temperatures above 80 K the optical phonons would be expected to begin to dominate and the coherence time of the cyclotron motion would be expected to be even shorter [22]. The significant drop in the amplitude of the oscillations below ~30 K was not expected, although in many semiconductors, the electron mobility begins to plateau at these temperatures [23]. It has been shown that in very pure samples impu-

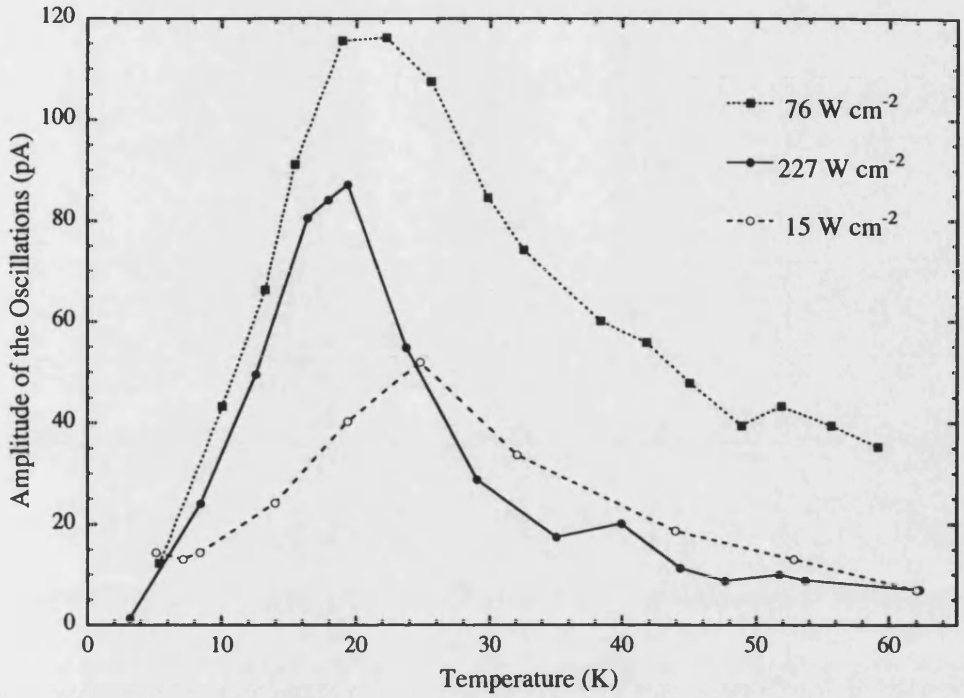

FIGURE 4.7: The temperature dependence of the amplitude of the observed cyclotron resonance oscillations at different power densities.

rity scattering can dominate and can cause the mobility to drop by an order of magnitude below 20-30 K [24].

A fit can be made to the temperature dependent data based on electron scattering dominated by interactions with the acoustic phonon below ~80 K such that the mobility of the electrons $\mu_e \propto T^{-3/2}$ [25]. Below 30 K the interaction is dominated by interaction with the impurities, both the ionised and the neutral, where the electron mobility $\mu_e \propto T^{3/2}$ [26, 27]. Figure 4.8 shows qualitative agreement in trend for the case where the silicon was illuminated by a power density of 227 W cm^{-2}

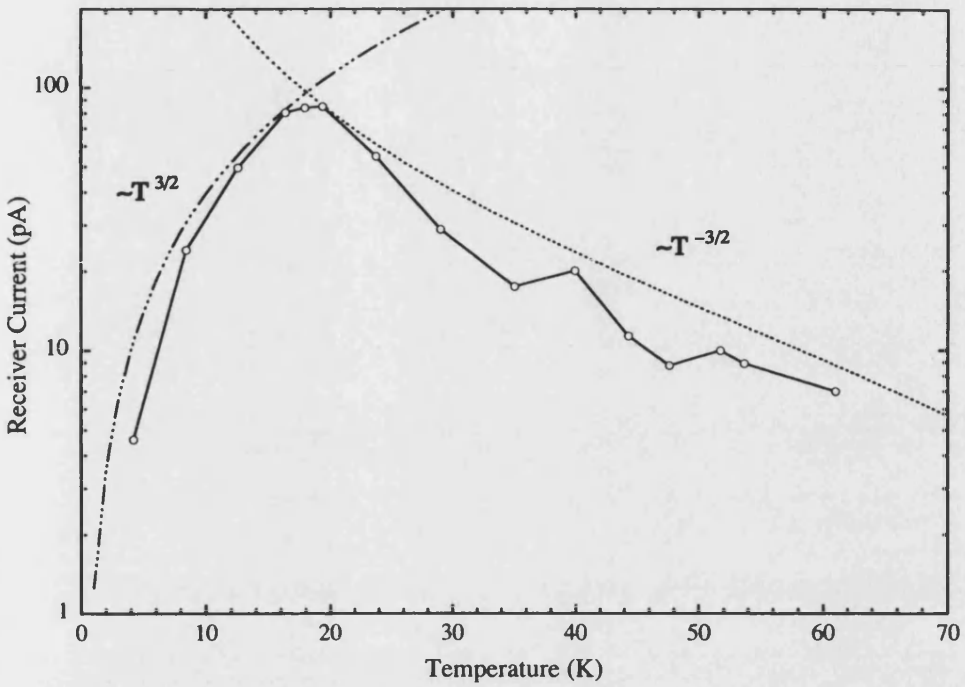

FIGURE 4.8: The temperature dependence of the amplitude of the cyclotron resonance oscillations at a magnetic field of 5 T and a pump power density of 227 W cm^{-2}.

4.3 Summary

The first reported practical use of an InAs sample as a source of coherent THz radiation in pump probe spectroscopic measurements has been presented. The THz spectroscopy measurements were performed on the cyclotron resonance of photoexcited carriers in high resistivity silicon. The temperature dependence of the oscillations was measured, and explained in terms of scattering by acoustical phonons and neutral impurity scattering.

The use of an InAs source provides a means by which the optical excitation beam and the generated THz beam can be directed colinearly on to the subject sample

with greater ease than when using the TDTS in the usual configuration, however the fact that the time delay between the optical pulse and the THz electrical transient cannot be changed limits the usefulness of the technique.

References

[1] *'Terahertz-Time Domain Spectroscopic Measurement of Moderately-Doped Silicon Using InAs Emitter Under Magnetic Field.'*
Japanese Journal of Applied Physics, pp. 867–872, **40**(1)No.2A, Feb. 2001.

[2] G. Dresselhaus, A.F. Kip and C. Kittel
'Observation of Cyclotron Resonance in Ge Crystals.'
Physical Review, Letters to the Editor, pp. 827, **92**, 1953.

[3] J. Dorfmann
Doklady Acad. Sci. (USSR), pp. 765–, **81**, 1951.

[4] R.B. Dingle
Ph.D. thesis, Cambridge University, 1951; Proceedings of the International Conference on Very Low Temperatures, edited by R. Bowers, pp. 165, Oxford, England Aug. 1951; Proceedings of the Royal Society, pp. 38–, **A212**, 1952.

[5] W. Shockley
'Cyclotron Resonances, Magnetoresistance and Brillouin Zones in Semiconductors.'
Physical Review, Letters to the Editor, pp. 491–492, **90**, 1953.

[6] R.N. Dexter, H.J. Zeiger & B. Lax
'Anisotropy of Cyclotron Resonance of Holes in Ge.'
Physical Review, Letters to the Editor, pp. 557–558, **95**, 1954.

[7] G. Dresselhaus, A.F. Kip and C. Kittel
'Cyclotron Resonance of Electrons and Holes in Silicon and Germanium Crystals.'
Physical Review, pp. 368–384, **98**(2), Apr. 15^{th} 1955.

[8] M. Asche & O.G. Sarbei
'Electron–Phonon Interaction in n-Si.'
Review Article for Phys. Stat. Sol. B, pp. 11–49, **103**(11), 1981

[9] C. Kittel
'Solid State Physics.'
John Wiley & Sons, 5^{th} Edition, 1990.

[10] C. Jacoboni, C. Canali *et al.*
'A Review of Some Charge Transport Properties of Silicon.'
Solid State Electronics, pp. 77–89, **20**, 1977

[11] S.M. Sze
'Physics of Semiconductor Devices.'
John Wiley & Sons, 1981.

[12] R.R. Scaller
'Moore's Law, Past, Present and Future.'
IEEE Spectrum, pp. 52–59, **34**(6), June 1997.

[13] T.A.C.M. Claasen
'High Speed: Not the Only Way to Exploit the Intrinsic Computational Power of Silicon.'
1999 International IEEE Solid State Circuits Conference Digest of Technical Papers, ISSCC 1^{st} Edition, pp. 22-25, 1999.

[14] R. Borkar
'Obeying Moore's Law Beyond 0·18 micron Microprocesor Design.'
Proceedings of the 13^{th} Annual IEEE International ASIC/SOC Conference, pp. 26-31, 2000.

[15] G.E. Moore
'Lithography and the Future of Moore's Law.'
Proceedings of SPIE–The International Society for Optical Engineering, pp. 2–17, **2440**, 1995.

[16] A.G. Milnes
'Semiconductor Devices and Integrated Electronics.'
Van Nostrand Rheinhold Co., 1980.

[17] N.B. Hannah
'Semiconductors.'
Rheinhold Publishing Corp., 1960.

[18] T.P. M^{c}Lean
'Progress in Semiconductors', Vol. 5, Edited by A.F. Gibson
Heywood, London 1960.

[19] I.M. Tsidilkovski, Translated by R.S. Wadhwa
'Band structure of semiconductors.'
Oxford, Pergamon Press, Vol.**19** (International Series in the Science of the Solid State) 1982

[20] M.L. Cohen J.R. Chelikowsky, *'Electronic Structure and Optical Properties of Semiconductors.'*
Springer-Verlag, Berlin, 1988.

[21] C.J. Rauch, J.J. Stickler *et al.*
'Millimeter Cyclotron Resonance in Silicon.'
Physical Review Letters, pp. 64–66, 4(2), Jan. 1960.

[22] P.Y. Yu & M. Cardona
'Fundamentals of Semiconductors; Physics and Materials Properties.'
Springer-Verlag, Berlin, 1996.
ISBN: 3–540–58307–6

[23] P. Norton, T. Braggins & H. Levinstein
'Impurity and Lattice Scattering Parameters as Determined from Hall and Mobility Analysis in n-type Silicon.'
Physical Review B, pp. 5632–5653, 8(12), Dec. 1973.

[24] F.J. Morin & J.P. Maita
'Electrical Properties of Silicon Containing Arsenic and Boron.'
The Physical Review, pp. 28–35, **96**(1), Oct. 1^{st} 1954.

[25] D. Long
'Scattering of Conduction Electrons by Lattice Vibrations in Silicon.'
Physical Review, pp. 2024–2032, **120**(6), Dec. 1960.

[26] L. Solymar & D. Walsh
'Lectures on the Electrical Properties of Materials.'
Oxford Science Publications, 3^{rd} Edition, 1984.

[27] E. Conwell & V.F. Weisskopf
'Theory of Impurity Scattering in Semiconductors.'
Physical Review, pp. 388–390, **77**(3), Feb. 1950.

Chapter 5

Observation of Ferromagnetic Resonance in the Time Domain

Over the past 15 to 20 years there has been considerable interest in probing the magnetic properties of materials by using magneto-optic measurement techniques, in particular methods which probe the surface region down to 20 to 40 nm. This has been prompted by the advances in high density and high speed magnetic recording media [1, 2] and the ease and cost-effectiveness with which a magneto-optic Kerr effect (MOKE) or Faraday rotation measurement system can be constructed. The low cost of the MOKE technique has some distinct advantages over other more expensive techniques. The MOKE is not sensitive to the impurities that are always present in the substrate upon which the sample film is situated, and the region probed is of a very small area, and is thus relatively insensitive to edge effects.

Numerous examples of the use of the MOKE to characterise the magnetic properties of thin films down to sub-monolayer thicknesses and the surface region of magnetic materials exist and there are many review articles [3, 4, 5]. Some materials have been engineered to give a large Kerr rotation — such as the TbFeCo

(terbium iron cobalt) compounds, which are currently used in most of the MO (magneto-optic) recording materials [6].

The surface magneto-optic Kerr effect (SMOKE) was first presented by E.R. Moog *et al.* [7], whereby the ferromagnetic hysteresis loops of monolayer films of iron were investigated under ultrahigh vacuum conditions. Following this work thin films of other ferromagnetic materials such as nickel and cobalt deposited on single crystal substrates have been investigated. Additionally, multilayer structures comprising two or more ferromagnetic layers in proximity or separated by an intervening layer, as well as ferromagnetic thin films sandwiched between non-magnetic materials, have often been investigated using the MOKE measurement technique [8]. More recently, the MOKE has been used to show how the local ion-irradiation of Co/Pt ultrathin film structures can be used to pattern the magnetic properties down to the sub-micron scale [9, 10]; this technique has been proposed to be used in the design of new ultrahigh density magnetic storage media.

As well as knowing the magnetic characteristics of a material in terms of the coercivity, saturation magnetisation, etc., it is becoming increasingly important to understand the dynamics of the processes involved in high speed magnetisation reversal. High speed reversal is essential for the fast writing of logical 'bits' in ultra-high density magnetic storage media, and so picosecond magnetisation dynamics of micro- and nano-structured ferromagnets has therefore generated a great deal of interest [11, 12]. High speed magnetic switching is also under investigation in magnetic random access memory (MRAM) devices [13, 14] and will also be necessary for the development of spin-injection devices [15] and other applications in spintronics [16].

Down to the nanosecond range, magnetisation reversal is dominated by the do-

main wall motion [17], whilst picosecond reversal is dominated by the precessional motion of the magnetisation. The damping mechanisms required for picosecond reversal are not yet understood and the dependence of the reversal on the size, shape and magnetic anisotropy have yet to be studied [19].

Time-resolved optical pump-probe techniques are well suited to investigate such high speed characteristics, and such a technique was presented by Johnson *et al.* [18] in 1996 to study the spin lattice relaxation time in gold. It was then extended in 1997 to study fast magnetic properties in thin film ferromagnetic alloys [20]. It is an experimental technique based on this original work that is described in §5.3.

In this chapter, a brief discussion in terms of the microscopic theory of the magneto-optic effect is given, and is followed by an extended overview within the context of the macroscopic dielectric theory. Results of the characterisation of the in-plane magnetisation by the use of a standard quasi-static MOKE measurement technique are presented. A discussion of the time resolved MOKE measurement technique is given, and results are presented for the optical detection of small amplitude ferromagnetic resonance (FMR) oscillations, which are shown to agree well with the established FMR theory. Although the measurement of the time revolved MOKE in permalloy and iron has been presented previously, the work on cobalt is novel, and the construction of the system will allow future investigations into such materials as magnetic semiconductors as well as patterned micro-fabricated ferromagnetic structures.

5.1 The Magneto-Optic Kerr Effect

Magneto-optics have been used extensively ever since the discovery by Michael Faraday in 1845 [21] that a piece of glass placed in a magnetic field changed the optical polarisation of a light wave propagating through it. The corresponding effect in reflection, the magneto-optic Kerr effect, was subsequently discovered by the Rev. John Kerr in 1876 [22], after the observation of the reflection of a light beam on the polished pole piece of a magnet. It wasn't until 1932 that the microscopic theory was completed by Hulme [23], who stated that the effect is caused by the coupling between the electric field of the propagating radiation and the electron spin in an applied magnetic field, due to the spin-orbit interaction. This interaction couples the magnetic moment of the electron with its motion, and thus connects the magnetic and optical properties of a ferromagnet. For nonmagnetic materials, this effect is weak, because the equal number of spin-up and spin-down electrons cancels any macroscopic nette effect and results in the rotation of the polarisation of the light being directly proportional only to the external applied field. For ferromagnetic materials, however, the imbalance in the number of up- and down-spins does give rise to a nette effect, and this results in the polarisation rotation being directly proportional to the sample magnetisation, and not the external applied field [24].

5.1.1 Macroscopic Theory of the MOKE

Macroscopically, the magneto-optic Kerr effect arises from the antisymmetric, off-diagonal elements in the dielectric tensor [5, 25]. Linearly polarised light can be thought of as being comprised of two circularly polarised components, left circular

polarisation and right circular polarisation. It is clear that when these two modes propagate in a medium, the different electric fields will interact with the electrons to produce left circular motion and right circular motion respectively. Assuming an isotropic and non-magnetised medium, the radius of electron orbit for the left and the right circular motion will be the same, and since the electric dipole moment is proportional to the radius of orbit, there will be no difference in the dielectric constants for the left or right circularly polarised light. However, when a magnetic field is applied, an additional Lorentz force acts on each electron. This force will alter the radius of the electron orbit differently for the two modes, and give rise to the asymmetry in the dielectric constant as experienced by the two circularly polarised modes. Thus, macroscopically, it is the Lorentz force that generates the magneto-optic effect, through the dielectric tensor.

If $\mathbf{E}$ is a periodic electromagnetic field with an angular frequency of ω, then an appropriate definition is $\mathbf{E} = \mathbf{E}_o e^{-\jmath\omega t}$. Assuming that the magnetic susceptibility of the medium is near zero at visible light frequencies due to the fact that spin-precession frequencies are several order of magnitude lower, that there is no static electric charge ($\varrho = 0$) and that the medium is homogeneous, then the relevant Maxwell equation can be expressed as,

$$\nabla \times \mathbf{H} = \left(\varepsilon_o + \tilde{\alpha}_{ij} + \frac{\jmath}{\omega}\tilde{\sigma}_{ij}\right)\frac{\partial \mathbf{E}}{\partial t} \tag{5.1}$$

and by comparison with Equation 5.2 [26], the generalised dielectric tensor can therefore be defined as that shown in Equation 5.3,

$$\nabla \times \mathbf{H} = \varepsilon\frac{\partial \mathbf{E}}{\partial t} + \mathbf{j} \tag{5.2}$$

$$\tilde{\varepsilon}_{ij} = \varepsilon_o + \tilde{\alpha}_{ij} + \frac{\jmath}{\omega}\tilde{\sigma}_{ij} \tag{5.3}$$

The nine elements of the dielectric tensor can be defined as below, where it can be shown that $\varepsilon_{ij} = \varepsilon_{ji}$, which means that when $i = j$, then ε_{ij} is simply defined as ε, due to the Hermiticity of the tensor.

$$\tilde{\varepsilon}_{ij} = \begin{pmatrix} \varepsilon & \varepsilon_{12} & \varepsilon_{13} \\ \varepsilon_{12} & \varepsilon & \varepsilon_{23} \\ \varepsilon_{13} & \varepsilon_{23} & \varepsilon \end{pmatrix} \tag{5.4}$$

For an isotropic material with no magnetisation, the off diagonal terms reduce to zero, and the dielectric tensor can be considered a scalar such that $\tilde{\varepsilon}_{ij} \equiv \varepsilon$,

$$\tilde{\varepsilon}_{ij} = \begin{pmatrix} \varepsilon & 0 & 0 \\ 0 & \varepsilon & 0 \\ 0 & 0 & \varepsilon \end{pmatrix} \tag{5.5}$$

The expression in Equation 5.5 is the dielectric constant of the material, $\varepsilon = \varepsilon_o\varepsilon_r$, and these diagonal tensor elements are unaffected by the application of a magnetic field or by the presence of the magnetisation of the material to the first order in H and M. With the application of a magnetic field, or considering a magnetised material, the off diagonal tensor elements become non-zero, and it can be shown [25] that $\tilde{\varepsilon}_{ij}(\mathrm{M}) = \tilde{\varepsilon}_{ji}(-\mathrm{M})$, and hence,

$$\tilde{\varepsilon}_{ij} = \begin{pmatrix} \varepsilon & \varepsilon_{12} & \varepsilon_{13} \\ -\varepsilon_{12} & \varepsilon & \varepsilon_{23} \\ -\varepsilon_{13} & -\varepsilon_{23} & \varepsilon \end{pmatrix}$$

In a medium having an arbitrary magnetisation, the general dielectric tensor can be expressed in terms of Q_v, the Voigt parameter [27], (sometimes referred to as the complex magneto-optic coupling factor).

$$\tilde{\varepsilon}_{ij} = \varepsilon \begin{pmatrix} 1 & -\jmath Q_v M_z & \jmath Q_v M_y \\ \jmath Q_v M_z & 1 & -\jmath Q_v M_x \\ -\jmath Q_v M_y & \jmath Q_v M_x & 1 \end{pmatrix} \tag{5.6}$$

The terms M_x, M_y and M_z refer to the direction cosines of the magnetisation vector $\mathbf{M}$, in a cartesian coordinate system as shown in Figure 5.1.

When a plane polarised optical wave propagates through this magnetised medium, the right (R) and left (L) circularly polarised components experience different refractive indices due to the asymmetric dielectric tensor. The different refractive indices can be expressed in terms of the Voigt vector, $\mathbf{Q_v} = \hat{\mathbf{m}} Q_v$ as, $n_L{=}n(1 - \frac{1}{2}\mathbf{Q_v} \cdot \hat{\mathbf{k}})$ and $n_R{=}n(1 + \frac{1}{2}\mathbf{Q_v} \cdot \hat{\mathbf{k}})$, where $n{=}\sqrt{\varepsilon}$ is the average refractive index and $\hat{\mathbf{k}}$ is the unit vector along the direction of light propagation. There is therefore a difference in the refractive index as experienced by the two circularly polarised modes, and a phase difference is introduced. The complex rotation of the polarisation plane of the light is given below in Equation 5.7, where the real part gives the Kerr rotation and the imaginary part gives the Kerr ellipticity.

$$\theta = (n_L - n_R) = -n\mathbf{Q_v} \cdot \hat{\mathbf{k}} \tag{5.7}$$

The measurement of the Kerr effect is obviously related to the state of the reflected light from the sample, and so it is more convenient to define the rotation in terms of the complex reflection coefficients. Figure 5.1 defines the typical MOKE

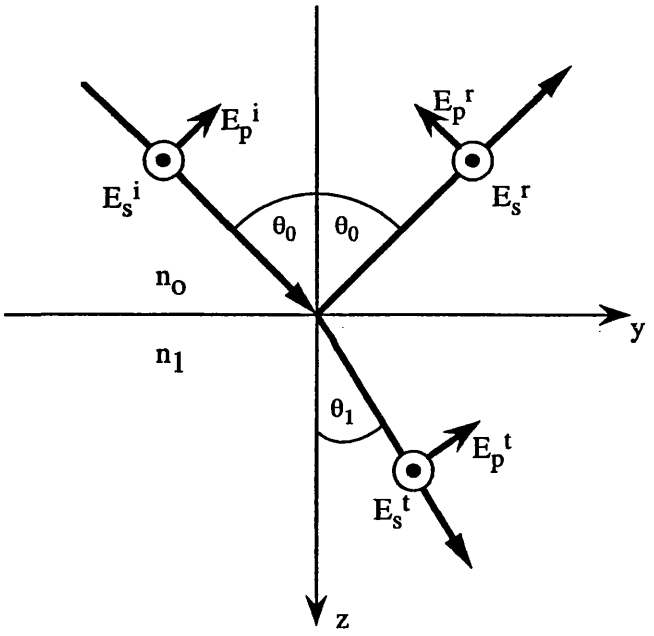

FIGURE 5.1: The geometry of the electric field and direction of propagation of the light wave in a standard MOKE experiment.

optical geometry for probing an interface between a non-magnetic material of refractive index n_o and a magnetic material of index n. By taking the relevant Jones matrix formalism [28], the reflected electric field can be expressed as shown in Equation 5.8 below where r_{pp}, r_{ss}, r_{ps} and r_{sp} represent the complex Fresnel coefficients which contain terms proportional to the Voigt parameter, as shown in Equations 5.9–5.12.

$$\begin{pmatrix} E_p^r \\ E_s^r \end{pmatrix} = \begin{pmatrix} r_{pp} & r_{ps} \\ r_{sp} & r_{ss} \end{pmatrix} \begin{pmatrix} E_p^i \\ E_s^i \end{pmatrix} \tag{5.8}$$

$$r_{ss} = \frac{n_1 \cos\theta_o - n_o cos\theta_1}{n_1 \cos\theta_o + n_o cos\theta_1} \tag{5.9}$$

$$r_{pp} = \frac{n_1 \cos\theta_o - n_o cos\theta_1}{n_1 \cos\theta_o + n_o cos\theta_1} + \frac{2jQ_v n_o n_1 \cos\theta_o \sin\theta_1 u_y}{(n_1 \cos\theta_o + n_o cos\theta_1)^2} \tag{5.10}$$

$$r_{ps} = -\frac{\jmath Q_v n_o n_1 \cos\theta_o \left(\sin\theta_1 u_x - \cos\theta_1 u_z\right)}{\cos\theta_1 \left(n_o \cos\theta_o + n_1 \cos\theta_1\right)\left(n_1 \cos\theta_o + n_o \cos\theta_1\right)} \tag{5.11}$$

$$r_{sp} = \frac{\jmath Q_v n_o n_1 \cos\theta_o \left(\sin\theta_1 u_x + \cos\theta_1 u_z\right)}{\cos\theta_1 \left(n_o \cos\theta_o + n_1 \cos\theta_1\right)\left(n_1 \cos\theta_o + n_o \cos\theta_1\right)} \tag{5.12}$$

In the above expressions, n_0 and n_1 are the refractive indices of the non-magnetic material and the magnetic material respectively. The angle θ_o is the angle of incidence and θ_1 is the complex refractive angle.

Simple MOKE measurement configurations are obtained for incident light that is s-polarised ($E_p^i = 0$) or p-polarised ($E_s^i = 0$). As any Kerr rotation will involve a component of the polarisation rotating from say the s-polarised state to the p-polarised state, the Kerr rotation can be expressed as [29] the real part of the quotient,

$$\theta_k = -\Re\left(\frac{r_{ps}}{r_{ss}}\right) \tag{5.13}$$

By taking the expressions from Equations 5.9 and 5.11, the Kerr rotation can be expressed for the longitudinal Kerr configuration as [30, 31],

$$\theta_k = -\Re\left[\frac{\cos\theta_o \tan\theta_o}{\cos(\theta_o - \theta_1)} \cdot \frac{\jmath n_o n_1 Q_v}{(n_1^2 - n_o^2)}\right] \tag{5.14}$$

For an arbitrary magnetisation direction, the longitudinal Kerr rotation is dominated by the direction cosines of the magnetisation M_y and M_z, and Equation 5.14 can be expressed as [32, 33],

$$\theta_k = -\Re\left[\frac{\cos\theta_o (M_z - M_y \tan\theta_o)}{\cos(\theta_o - \theta_1)} \cdot \frac{\jmath n_o n_1 Q_v}{(n_1^2 - n_o^2)}\right] \tag{5.15}$$

The Kerr effect is thus expressed as the product of two terms: the term on the left is simply a function of the optical parameters of the medium and the incident angle of the light, the term on the right is the polar Kerr effect for light at normal incidence [32, 33].

5.2 Quasi-Static MOKE

From a general point of view the Kerr rotation and Kerr ellipticity can be measured independently. However, to measure the Kerr rotation three standard MOKE configurations are generally used. These are commonly referred to as the 'polar', 'longitudinal' and 'transverse' or 'equatorial' geometries. The geometrical differences between these configurations are outlined in Figure 5.2. In the polar Kerr configuration (Figure 5.2a), the light propagates along the magnetisation direction, which is perpendicular to the plane of the sample. This configuration yields the strongest signal of all the configurations, and is sensitive to the perpendicular component of the sample magnetisation. In the longitudinal case (Figure 5.2b), the magnetisation lies both in the plane of the sample and the plane of incidence. This configuration is sensitive to the in-plane component of the magnetisation. For the transverse Kerr effect (Figure 5.2c), the magnetisation is still oriented in the plane of the sample, but perpendicular to the plane of incidence of the light. In this last case, there is no rotation of the plane of polarisation of the light, nor is there any ellipticity. This can be seen by examination of Equation 5.7, where the rotation is proportional to the dot product of the vectors $\mathbf{Q_v}$ and $\hat{\mathbf{k}}$. In the transverse case the angle between the two is 90°. However, a change in the reflectivity can be detected, and provides a measure of the magnetisation perpendicular to the plane of incidence.

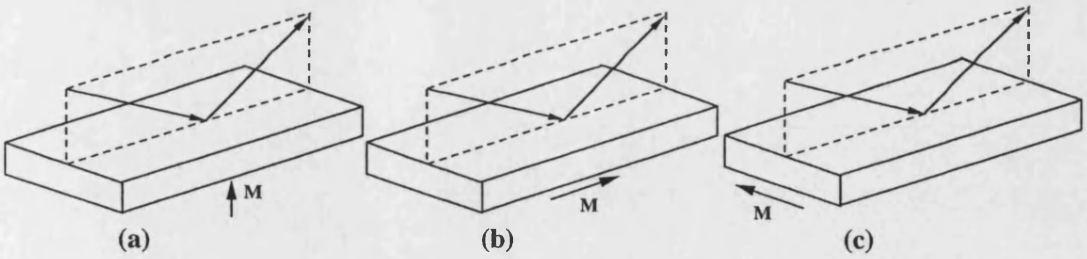

FIGURE 5.2: Schematic to show the three standard different experimental geometries used to measure the magneto-optic Kerr effect; **(a)** polar, **(b)** longitudinal and **(c)** transverse (equatorial).

5.2.1 Experimental System: Quasi-Static Measurements

In this case, the longitudinal MOKE configuration was chosen to measure the hysteresis loops of thin magnetic films before the subsequent investigation by use of the time resolved measurement technique. The longitudinal geometry was used in the following experiments due to the need to measure the Kerr rotation directly, and by the constraints imposed by the experimental system. A schematic of this measurement system is shown in Figure 5.3.

After reflection by a ferromagnetic thin film, the rotation of the polarisation of the probing light is of the order $\sim 90\,\mu$rad, and so a light source with a SNR better than 1 part in 10^6 was considered desirable, hence different light sources were tested during the development of the quasi-static measurement system. These light sources consisted of a HeNe laser, an ultrabright LED and a laser diode. The mode-hopping and long-term drift in the output of the HeNe ($\sim$2% over 1 minute) with an average output of 10 mW at 632·8 nm, made the measurement of the Kerr rotation incredibly difficult. The ultrabright LED [34] had the best SNR of all three sources, but the collimated beam had insufficient power for the system; the LED only having a power output of 1 mW at 830 nm. The best

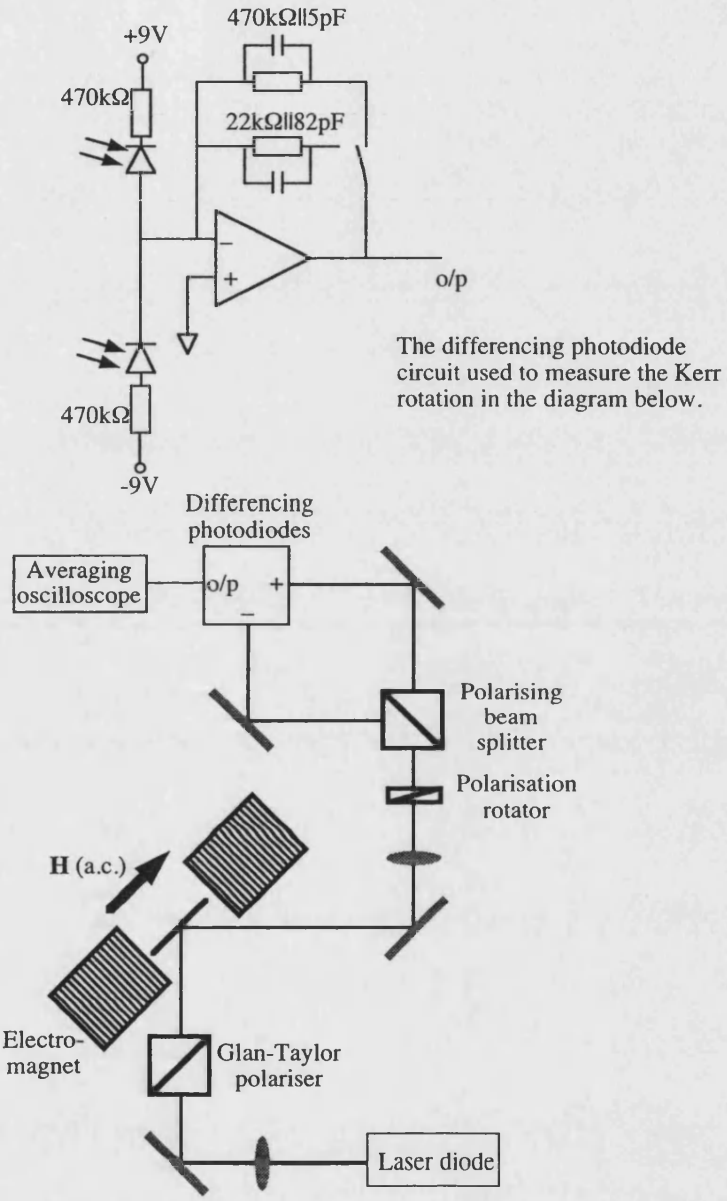

FIGURE 5.3: The experimental setup of the standard longitudinal MOKE measurement system.

overall light source was found to be the laser diode with a SNR of 1 part in 10^6 and a maximum output power at 670 nm of 3 mW. Different light sources for magneto-optic work have been compared with one another, and the best SNR is found for laser diodes [36].

The extinction ratio of the polarisation of the laser diode was insufficient to define the linear polarisation to greater than 1 part in 50 [35], and so the output from the laser diode was steered via a focusing lens through a Glan-Taylor polariser [37]. The Glan-Taylor polariser defined the light as *s*-polarised, TE relative to the sample in this geometry. The extinction ratio was measured to be greater than 1 part in 1 part in 10^5. The beam was incident on the sample at $\sim 10°$ to the surface normal and the reflected beam was guided via another lens through a polarisation rotator, which rotated the polarisation to $\sim 45°$, so that when the beam passes through the polarising beam splitter, the two orthogonally polarised beams are of equal intensity. The polarising beam splitter was a Glan-Taylor style beam splitter, in which the *s*-polarised component of the beam is transmitted and the *p*-polarised component is reflected at 90° to the direction of propagation. Each of the orthogonally polarised beams is then separately guided onto one of two photodiodes [38]. The photodiodes were both reverse biased with 9 V and connected to a differencing current amplifier circuit, as shown in Figure 5.3.

The photodiodes have a sensitivity of 0·5 A/W and the differencing circuit has an adjustable gain and bandwidth. The sensitivity of the differencing photodiode circuit as a whole can be changed from 0·23 V/μW with a -3 dB bandwidth of 68 kHz, to 11 kV/μW with a -3 dB bandwidth of 88 kHz. The differencing diode circuit consists of an OP-27 low noise bipolar operational amplifier chip, arranged as in a negative feedback voltage amplifier configuration. The circuit produces

an output proportional to the difference in the two signals from the different photodiodes. In this way, any random short term fluctuations in the laser output power is removed from the signal. The output from the differencing amplifier is then passed through a buffer amplifier of unity gain and into an averaging oscilloscope, where typically 500 averages were taken to improve the SNR by a factor of $\sim$50.

The application of the quasi-static magnetic field was achieved by using an electromagnet consisting of two multiturn copper coils with a series impedance of $6\,\Omega$ — matched to the output impedance of a high power current amplifier. The current amplifier is capable of producing an alternating current of 7 A peak to peak through the coils, and with the iron pole pieces separated by $\sim$2·5 cm, the maximum attainable field was found to be $\sim$5 kOe. The field was typically modulated at 10-12 Hz and was measured by a commercial Hall sensor mounted on the sample stick, equidistant between the pole pieces. An averaging oscilloscope was then used to record and store the magnetic field and the output from the differencing diode circuit together.

With zero applied field, the polarisation rotator is adjusted so that the the intensity in the orthogonally polarised beams becomes equal and the output from the differencing circuit is balanced to zero. The d.c. signal from a single photodiode was of the order $\sim$1 V. With an a.c. field applied the MOKE causes a small rotation in the polarisation of the light about the balanced d.c. level and thus the two orthogonally polarised arms change relative to one another, one increasing, the other decreasing.

The change in the signal intensity from the balanced state is given by the differ-

ence between the measured intensities ΔR,

$$\Delta R = I_o \left[\cos^2(\alpha + \theta_k) - \sin^2(\alpha + \theta_k)\right] \tag{5.16}$$

where θ_k is the Kerr rotation and α is the balance angle. If the d.c. level of the system, i.e. the measured intensity in of one of the orthogonally polarised beams is given by R,

$$R = I_o \cos^2(\alpha) \tag{5.17}$$

then dividing Equation 5.16 by Equation 5.17,

$$\frac{\Delta R}{R} = \frac{\cos^2(\alpha + \theta_k) - \sin^2(\alpha + \theta_k)}{\cos^2(\alpha)} \tag{5.18}$$

By re-arranging and simplifying Equation 5.18,

$$\frac{\Delta R}{R} = \frac{2\cos^2(\alpha + \theta_k) - 1}{\cos^2(\alpha)} \tag{5.19}$$

Assuming θ_k to be small and taking the balance angle to be $\pi/4$ radian,

$$\cos^2(\alpha + \theta_k) \approx \frac{1}{2}\left(1 - \frac{1}{2}\theta_k^2 - \theta_k\right)^2 \approx \frac{1}{2}(1 - 2\theta_k) \tag{5.20}$$

then by combining Equation 5.19 and Equation 5.20 we get an equation relating directly the Kerr rotation to the measured $\Delta R/R$ signal,

$$\frac{\Delta R}{R} = -4\theta_k \tag{5.21}$$

This equation is equivalent to the expression given in equation 5.13. This treatment yields the Kerr rotation, but by the insertion of a quarter wave plate the ellipticity can also be measured.

5.2.2 Sample Characterisation

The quasi-static MOKE measurements were performed on permalloy ($Ni_{0.8}Fe_{0.2}$), cobalt and iron films deposited on glass microscope slides. The ferromagnetic metals were thermally evaporated onto the microscope slides at the same time as the time-resolved MOKE devices were fabricated, as discussed in §5.3 Sample Fabrication. The films each consisted of a 500±100 Å thick film of the ferromagnetic material, on top of a 50 Å thick film of NiCr, the wetting agent. The field applied by the electromagnet was ramped up to achieve saturation of the hysteresis loop, and 500 averages of the loop were recorded; Figure 5.4 shows results from all three samples.

For the purposes of characterising the samples for use in the time resolved MOKE measurement system, the important details to note in Figure 5.4 are the coercive field and the overall Kerr rotation. For permalloy, Figure 5.4(a) ,the coercive field is found to be 3 Oe, whilst in iron and cobalt the coercivity is found to be 10 Oe and 15 Oe respectively. These values are highly dependent on the film thickness, material purity, substrate and many other factors, so they cannot be reliably compared with published data. It was found during the course of this study that the different methods by which the films can be deposited also made a big difference to the coercivity of the films. It seems that both the sputter deposition and thermal evaporation of permalloy, for example, give rise to films

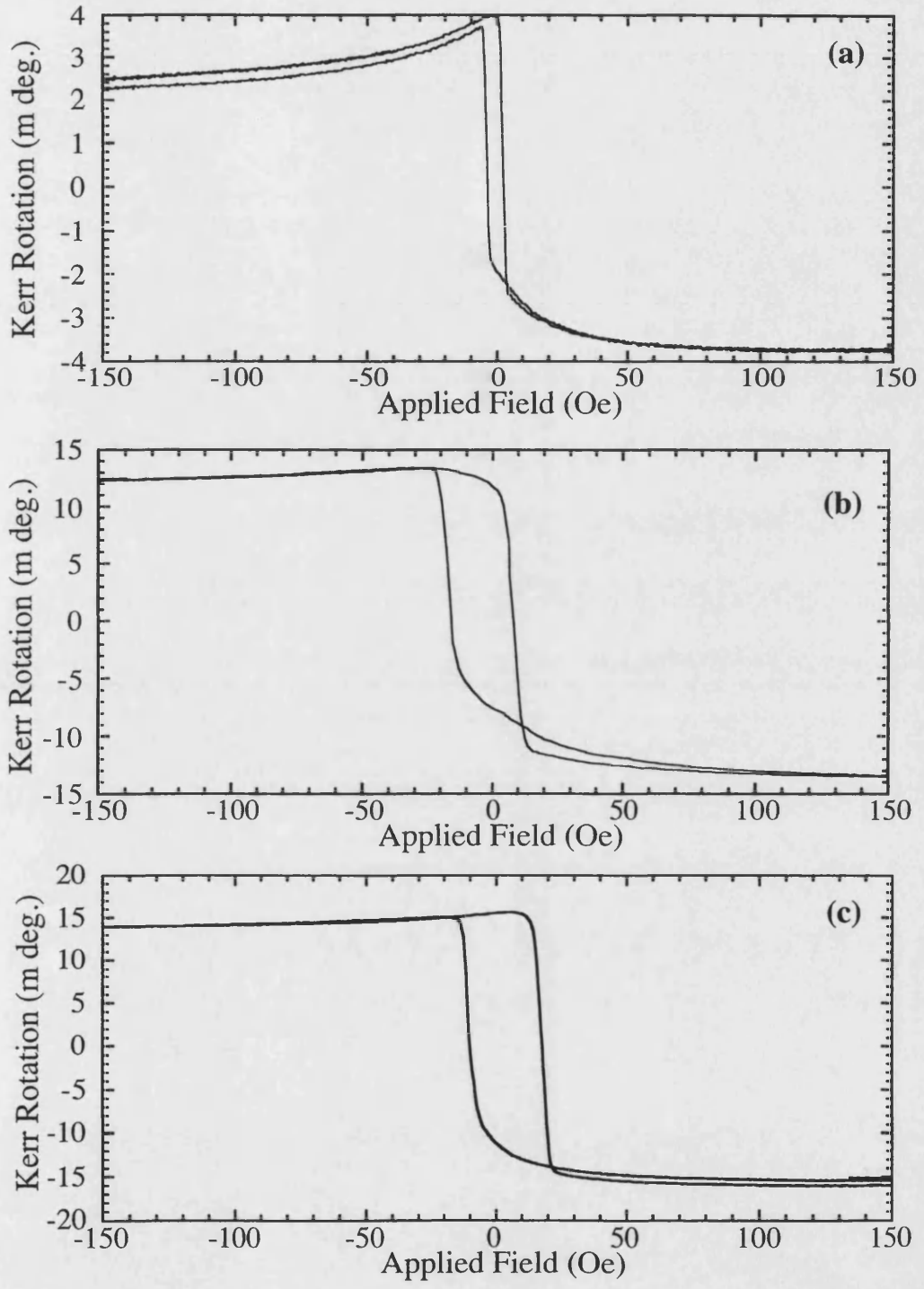

FIGURE 5.4: The Kerr rotation loops for the in-plane magnetisation as measured by the longitudinal MOKE experimental setup for **(a)** permalloy, **(b)** cobalt and **(c)** iron.

with a much lower coercivity than when the alloy is e-beam evaporated. In fact the coercive field in e-beam evaporated permalloy was found to be 4-5 times larger. The overall shape of the Kerr loop was much more square, hinting at much more isotropy in the magnetisation, and possibly the domains.

The Kerr rotation itself, however, can be compared with previously published results. The Kerr rotations measured here compare favourably with previously measured rotations [39], where permalloy displays a Kerr rotation of 3 m deg. The measured Kerr rotation for iron and cobalt were measured to be 15 m deg and 12 m deg respectively.

5.3 Time Resolved MOKE

Similarly to the quasi-static MOKE measurement technique outlined previously, the time resolved MOKE measures the transient Kerr rotation from the near surface region of a ferromagnetic film. The time resolved MOKE technique uses similar technology to that described in Chapter 2. An optical pump pulse gates an electrically biased photoswitch on a coplanar stripline, which gives rise to an electrical transient. The transient current subsequently gives rise to a transient magnetic field. Between the tracks of the stripline the generated magnetic field is perpendicular to the plane of the thin ferromagnetic film, and the thin ferromagnetic film is also under an in-plane d.c. applied field.

The generated magnetic transient induces a precession of the magnetic moments within the ferromagnetic thin film situated on top of the tracks separated by a thin insulating layer. Initially, a point equidistant between the tracks was illuminated

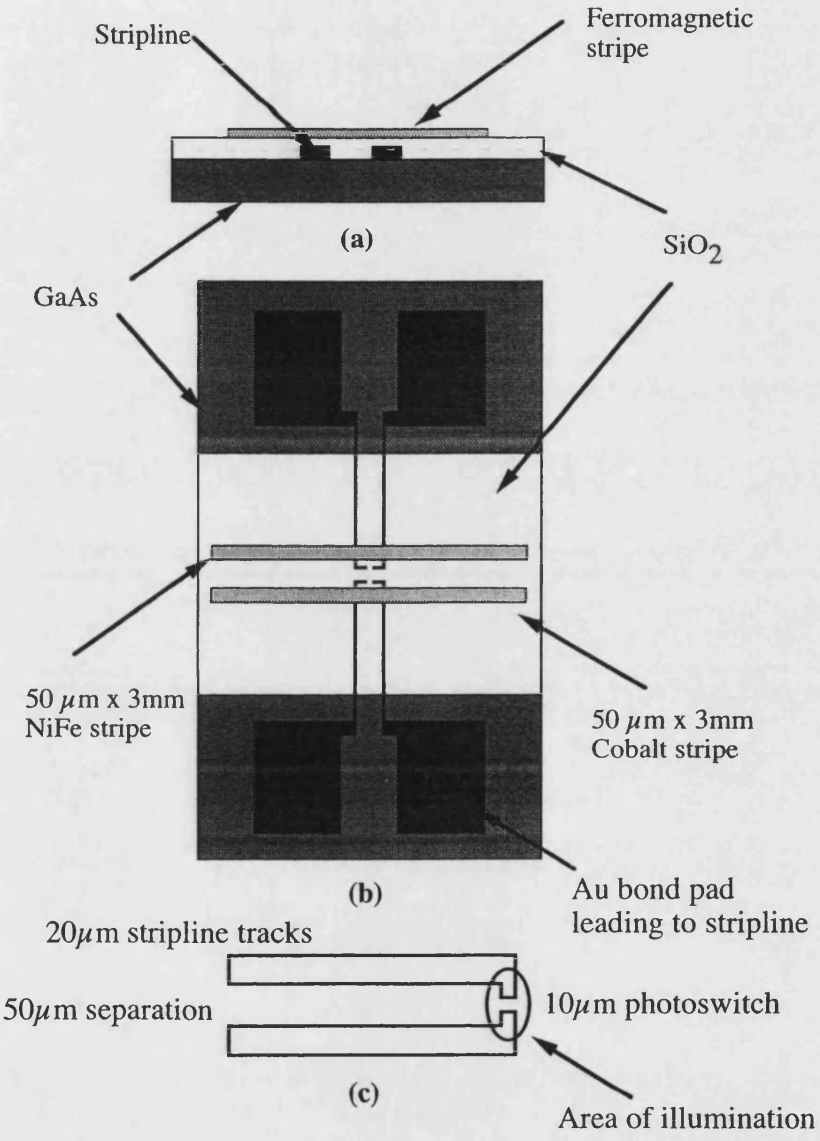

FIGURE 5.5: The structure of the MOKE time domain device in **(a)** cross-section and **(b)** plan views. Part **(c)** shows a closeup view of the 10 μm photoswitch.

by the focussed plane polarised probe beam, and a transient Kerr rotation was measured. The Kerr rotation is sensitive to both the in-plane (longitudinal) and the out of plane (polar) components of the magnetisation since the propagation vector of the light is not normal to the film surface.

Sample Fabrication

The time resolved MOKE device including, the ferromagnetic thin film sample, was fabricated using standard processing techniques as outlined in §2.2 Samples. However, a brief summary is given here for completeness. Initially the Ti/Au tracks were thermally evaporated onto the clean GaAs surface to achieve a thickness of 100 Å and 2000 Å respectively. The stripline consisted of two 20 μm wide, ~1 cm long tracks, separated by 50μm. The photoswitch on the stripline consisted of a $10\,\mu \times 10\,\mu$m gap, patterned by optical lithography. The drift velocity of GaAs can reach $\sim 10^7\,\mathrm{cm\,s^{-1}}$, and so for this size photoswitch the sweep out time for the photoexcited electrons could be as low as 100 ps. This may go someway to explain the good temporal resolution that is achieved in the results, which are shown later, when making a comparison with the previously published reports. For a sweep out time of 100 ps, the peak current in the device can reach a value of ~100 mA, and this value is used in the model to predict the form of the magnetic field shown later, which yields a peak field of ~5,Oe.

A thin film of SiO_2, 500 Å, was sputtered on to the surface of the chip as an insulating layer, and to provide a small amount of physical protection for the stripline. A long, thin, stripe of a ferromagnetic metal, either cobalt, permalloy ($Ni_{0.8}Fe_{0.2}$) or iron was then thermally evaporated onto the SiO_2 perpendicular to the long axis of the stripline tracks, as is shown in Figure 5.5. The 500 Å thick

ferromagnetic stripes were deposited after a wetting layer of $\leq$100 Å of nickel chromium ($Ni_{0.8}Cr_{0.2}$) which improved the adhesion properties of the films. To enable the quasi-static MOKE measurements to be performed more easily, a glass microscope slide was placed in the thermal evaporator, on to which the metals were also thermally evaporated.

To attempt to measure the magnetic field that was produced by the current in the stripline, a device was fabricated whereby the field produced by one of the striplines was detected by measuring the current induced in another stripline. The substrate between the striplines was cleaved so that no electrical cross-talk was detected. The experiment used the pump-probe technique, whereby a pump laser pulse excited the carriers in the photoswitch of the biased emitting stripline, and a probe laser pulse, delayed in time relative to the pump, then probed the photoswitch on the detection stripline. A high gain amplifier was used to detect the induced current and the output fed into a LIA. Although a signal was measured which gave a pulse duration of 40 ps at FWHM, the result is not considered definitive, and as such the 40 ps value has been treated with some scepticism.

5.3.1 Ferromagnetic Resonance

When a ferromagnetic material is placed in an applied static magnetic field, the magnetic moments of each atom will precess about the direction of the applied field. The precession frequency of the magnetic moment is proportional to the applied magnetic field and can be expressed classically by the application of the torque equation, where $\mathbf{m}$ is the atomic magnetic moment, $\mathbf{T}$ is the torque on

the moment and $\gamma = -g\mu_B/\hbar$ is the gyromagnetic ratio.

$$\frac{\mathrm{d}\mathbf{m}}{\mathrm{d}t} = -|\gamma|\mathbf{T} \tag{5.22}$$

In a thin film if there is no applied magnetic field perpendicular to the plane of the film, the degrees of freedom of the precession of the magnetic moment are reduced, and the magnetic moments are all in-plane. If the sample is magnetised in the direction of the applied effective field, $\mathbf{H}_{\text{eff}}$, then the magnetisation per unit volume, $\mathbf{M} = N\mathbf{m}$ taking N as the number density per unit volume, can be inserted into Equation 5.22,

$$\frac{\mathrm{d}\mathbf{M}}{\mathrm{d}t} = -|\gamma|\mathbf{T}_{tot} \tag{5.23}$$

where $\mathbf{T}_{tot} = \mathbf{M} \times \mathbf{B}$ is the torque on the total magnetic moment and so Equation 5.23 can be expressed as below, taking $\mathbf{B} = \mu_0\mathbf{H}$

$$\frac{\mathrm{d}\mathbf{M}}{\mathrm{d}t} = -|\gamma|\mu_0\left[\mathbf{M} \times \mathbf{H}_{\text{eff}}\right] \tag{5.24}$$

For convenience, γ_0 can be defined as $\gamma_0 = \gamma\mu_0$. It can be seen that if a magnetisation $\mathbf{M}$ is displaced from the applied field $\mathbf{H}_{\text{eff}}$, then it will continue to precess with a frequency equal to the Larmor frequency, $\omega_L = |\gamma_0|H_{\text{eff}}$, indefinitely, if it were not for some damping process. In general, losses in magnetism can have many origins: eddy currents, macroscopic discontinuities (*e.g.* Barkhausen jumps), diffusion and the re-orientation of lattice defects, or spin-scattering mechanisms can all introduce irreversibilities and losses. Appropriate damping terms have been presented by Landau and Lifshitz [25], Gilbert [40] and also by Bloch and Bloembergen [41]. Here, the Gilbert form has been chosen, but it should be noted that it

is essentially a modification of the original Landau-Lifshitz formalism [42]; Equation 5.25 being another representation of the Landau-Lifshitz equation and it is possible to convert between the Landau-Lifshitz and the Landau-Lifshitz-Gilbert equations [43].

$$\frac{\partial \mathbf{M}}{\partial t} = -|\gamma_0|\mathbf{M} \times \mathbf{H}_{\text{eff}} + \frac{\alpha}{M}\left(\mathbf{M} \times \frac{\partial \mathbf{M}}{\partial t}\right) \tag{5.25}$$

The second term on the right characterises the Gilbert damping [40] by introducing a dimensionless empirical damping factor α, which is used to describe unspecified local or quasi-local dissipative effects, like the relaxation of magnetic impurities or the scattering of spin waves on lattice defects. The damping turn allows the magnetisation to turn towards the effective field until both vectors are parallel in the static solution.

To reach the resonant frequency, thereby producing the effect known as ferromagnetic resonance (FMR), a relatively small a.c. magnetic field applied perpendicular to the larger d.c. is required. The frequencies normally required are in the r.f. range and so ordinarily a microwave source is used to pump a thin film of a magnetic material placed in a microwave cavity in a d.c. applied field [44]. However, the technique presented here uses the broadband magnetic field pulse, to stimulate the precession. Additionally the time resolution of the technique, <1 ps, yields very accurate information about the FMR oscillations and the damping rate of the precession itself.

5.3.2 Experimental System

A schematic of the experimental system is shown in Figure 5.6. At the heart of the time resolved MOKE measurement system is the Ti:sapphire laser and the near infra-red optics. This part of the measurement system has already been described fully in Chapter 2. The important points to state are that the laser produces pulses of light at 765 nm with a pulse width of 70 fs at FWHM, at a rate of 82 MHz. After the dispersion compensation prisms, the light is split into two beams in the ratio 95:5 — the 95% reflected beam is the probe beam and the transmitted 5% is the pump beam.

The pump beam was *p*-polarised and directed via a beam compressor through a $\times 10$ microscope objective lens of numerical aperture 0·3. The beam was focussed down to a size of $\sim 15\,\mu$m at FWHM, on to the biased photoswitch. The average power of the pump beam was measured to be 30 mW, hence a pulse energy of 0·36 nJ. The probe beam, however, was steered via a retroreflector mounted on a stepper motor to enable the relative delay between the pump and probe pulses to be varied. The stepper motor was incremented to give 1 ps steps in the relative time delay between the pump and probe pulses, over an 800 ps range. The beam was then directed via a separate beam compressor, and passed through a Glan-Taylor polariser. The Glan-Taylor polariser polarised the light in the *s*-polarised sense — opposite to that of the pump beam to prevent any optical cross-talk between the beams being detected further down the optical path. The Glan-Taylor polariser defined the polarisation to greater than 1 part in 10^5. The probe beam was then steered through the microscope objective lens and reflected back from the ferromagnetic sample on the device through the same lens. The angle of incidence of the probing light is 25° to the sample surface normal. A mirror

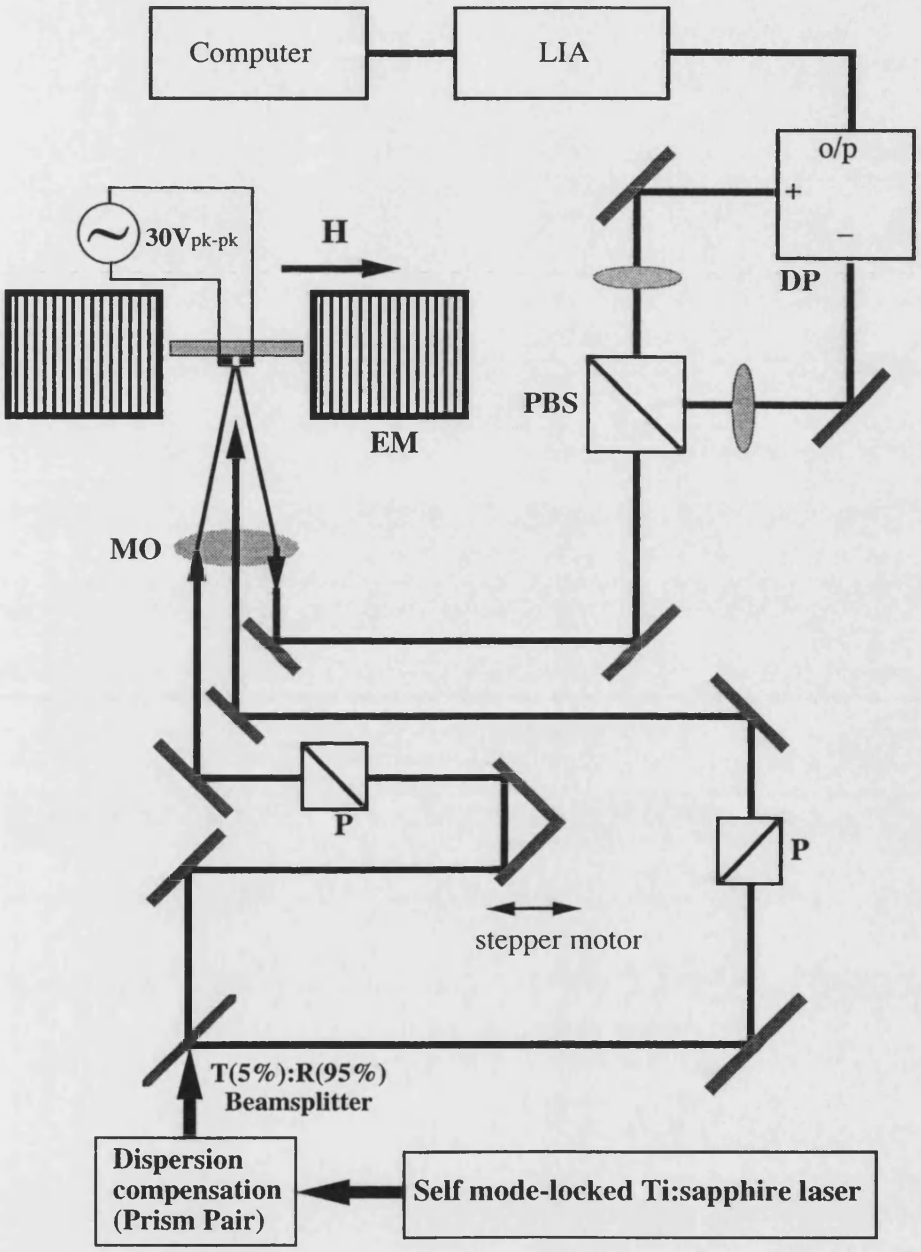

FIGURE 5.6: Schematic of the time domain MOKE experimental system. Definitions: electromagnet (EM), polarising beam splitter(PBS), differencing photodiodes (DP), microscope objective (MO), Glan-Taylor polariser (P), lock-in amplifier (LIA).

picked-off this reflected beam and directed it through a lens and subsequently a polarisation rotator.

A polarising beam splitter then splits the beam such that the s-polarised and p-polarised components are transmitted and reflected respectively. The polarisation rotator is used to rotate the d.c. polarisation such that the intensity in both the orthogonally polarised beams is equal. Two photodiodes detect the two orthogonally polarised beams, and the output of the two photodiodes is fed into a differencing circuit; a schematic of which is shown in Figure 5.3.

The photoswitch on the stripline was biased with an a.c. voltage of 20 V peak to peak, such that the average r.m.s. current flowing was $\sim$1 mA when illuminated by the pump beam. This enabled the use of a lock-in amplifier (LIA) to detect the Kerr rotation signal and thus an improvement in the SNR was achieved. With a time constant of 100 ms the LIA recorded 10 successive values at each time interval, the results were then averaged and stored on a computer.

The electromagnet was used to apply an in plane d.c. magnetic field from 50 Oe up to the maximum of 4 kOe; this field aligns the magnetic moments along the direction of the field. The pump beam causes a short across the biased photoconductive switch and so a magnetic field transient is generated perpendicular to the sample plane. This induces a change in the magnetisation of the sample and thus a Kerr rotation is detectable, similar to that described in §5.2.

5.4 Time Resolved FMR Results

The results for the time resolved Kerr measurements are presented here for permalloy, cobalt and iron. As expected, the observed time resolved Kerr rotation is smaller than that observed in the quasi-static measurements for the same film. This is despite the detected signal being dominated by the polar Kerr rotation, which is stronger than the longitudinal Kerr rotation. The small a.c. field was limited by the current in the stripline, which was restricted to $\sim$1 mA to increase the lifetime of the device. This resulted in a relatively small a.c. field which was smaller than the coercive field required to change the polarity of the magnetisation, as shown in the quasi-static measurements.

The oscillations that are observed in the time domain Kerr rotation traces are explained in terms of a ferromagnetic resonance model taken from the established model. The results for which are presented in §5.4.2.

5.4.1 Kerr Rotation

The time domain Kerr rotation traces are shown in Figures 5.7 ,5.8 and 5.9 for permalloy, iron and cobalt respectively. The largest measured Kerr rotation was 115 μdeg for permalloy at a field of 4 kOe and 291 μdeg for iron at a field of 4 kOe. For cobalt, however, the largest Kerr rotation of 283 μdeg was observed at an applied d.c. field of 2 kOe. These values are significantly smaller than the Kerr rotations observed in the quasi-static measurements, where the applied field was significantly larger than the coercive field. In the case of the time resolved Kerr measurements, the transient field has been calculated to be $\sim$5 Oe perpendicular

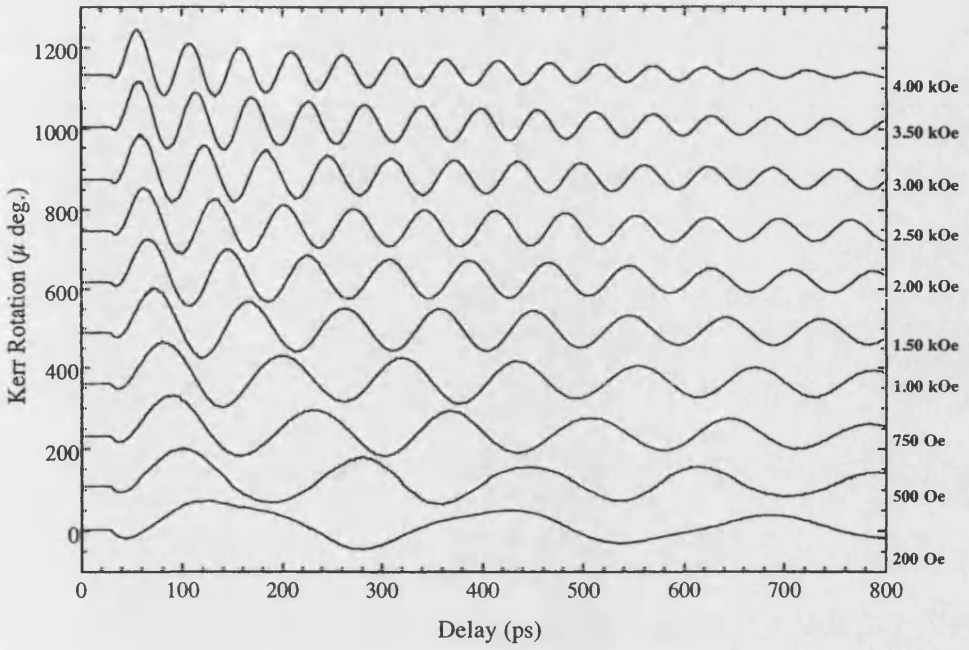

FIGURE 5.7: The time resolved MOKE for a 500 Å thin film of permalloy at different d.c. applied fields.

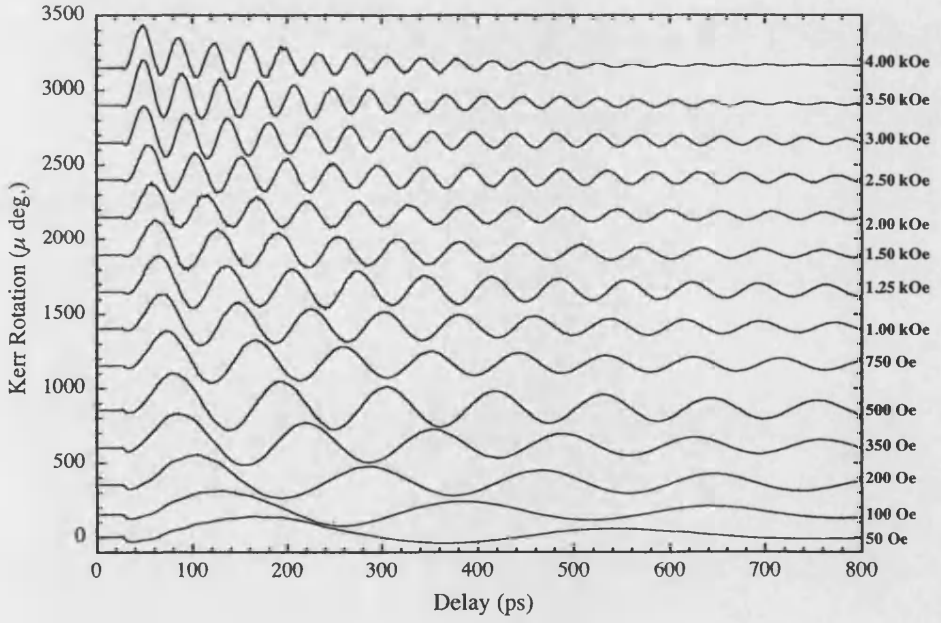

FIGURE 5.8: The time resolved MOKE for a 500 Å thin film of iron at different d.c. applied fields.

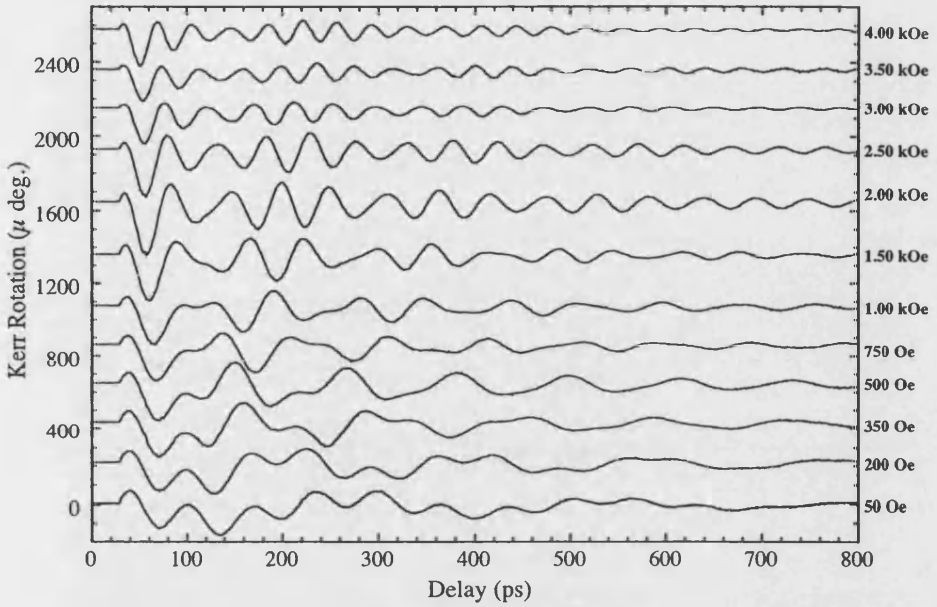

FIGURE 5.9: The time resolved MOKE for a 500 Å thin film of cobalt at different d.c. applied fields.

to the sample surface. Figure 5.10 shows a cross-section of the field distribution around the stripline.

In all three Figures 5.7, 5.8 and 5.9, there is more than frequency present in each trace; this is most clearly seen in the case of cobalt in Figure 5.9. To obtain the decay rates for the different frequency components, a fit of the form given below was used.

$$\vartheta_k = A_0 \cos(\omega_0 t + \phi_0) \exp(-t/\tau_0) + A_1 \cos(\omega_1 t + \phi_1) \exp(-t/\tau_1)$$

where τ_0 and τ_1 are the decay times of the two dominant frequency components, ω_0 and ω_1 found by performing an FFT on the data. Figure 5.11 shows the fit together with the experimental results for the three materials at a static field

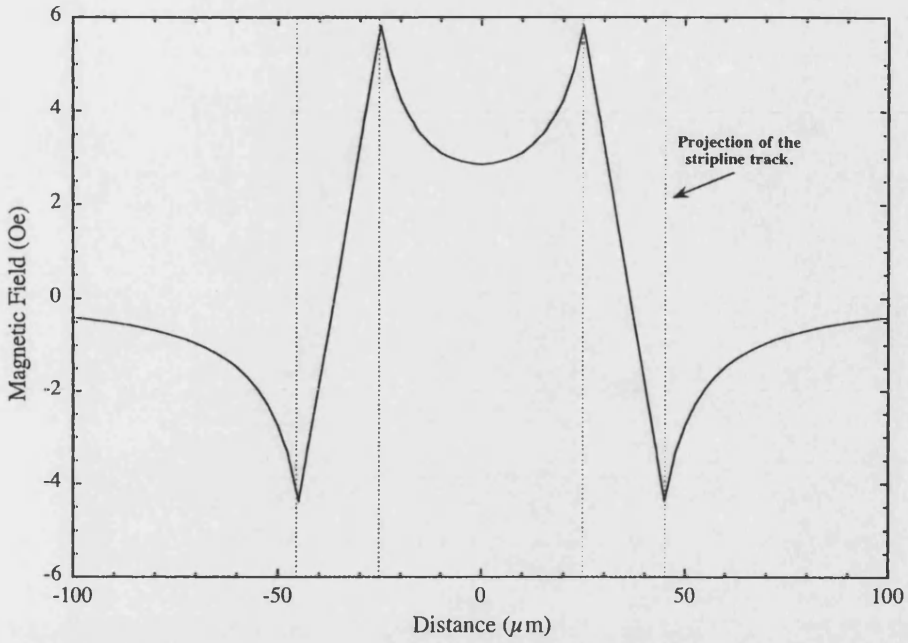

FIGURE 5.10: Cross-section of the predicted average magnetic field created by the current pulse in the stripline.

value of 4 kOe.

For the dominant frequency component the decay time was found to be 417±8 ps for iron, 415±24 ps for cobalt and 618±16 ps for permalloy. These times give an indication of the spin-spin dephasing time which is determined by the inhomogeneities of the samples, and any impurities that may be present, in addition to electron-phonon interactions which destroy the coherent precession of the magnetic moments. For the second frequency component that is seen in the traces, the fit yields exponential decay times of 142±17 ps in cobalt, 54±12 ps in iron and 20±8 ps in permalloy. In the thin film limit, cobalt exists as two different crystal structures. At thicknesses $\geq$40 Å cobalt has a b.c.c. crystal structure and the magnetisation tends to lie in-plane, whereas at thicknesses $\leq$40 Å the structure is f.c.c. and the magnetisation out of plane [45]. It is possible that because the

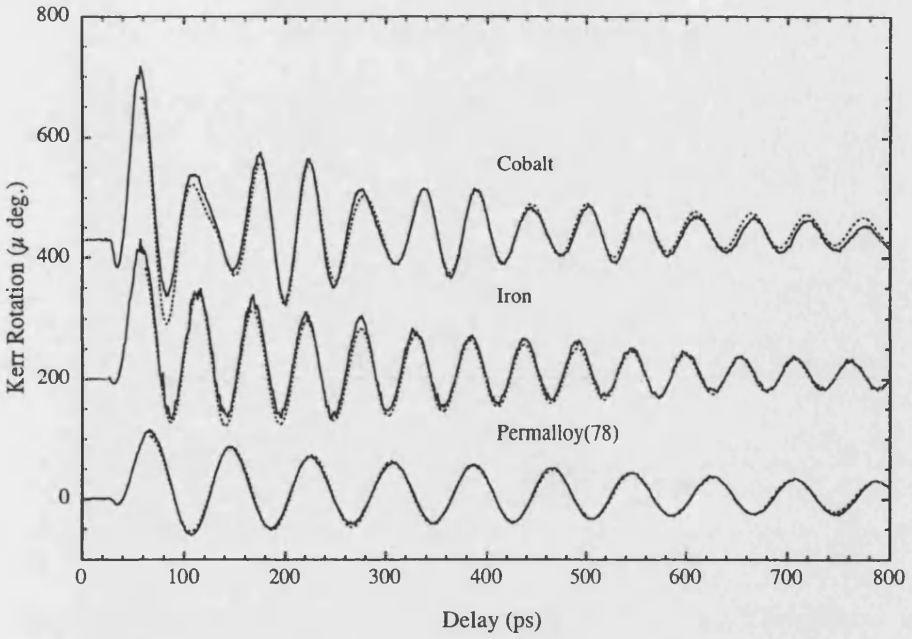

FIGURE 5.11: The time resolved Kerr rotation traces for iron, cobalt and permalloy at 4 kOe (solid lines), together with a fit (dashed lines) to the oscillations to determine the relaxation time.

film thickness of the samples studied were 500±100 Å then there may be a large anisotropy of the magnetisation in the sample.

It is clear that by adjusting the point of illumination of the probe beam on the ferromagnetic sample, the different in plane and out of plane components will contribute differently to overall measured Kerr rotation. At the centre point between the tracks for example, almost all the a.c. pump field is oriented perpendicular to the sample surface, whereas directly above the tracks, the field is likely to be in plane. This is one advantage of using the measurement system where both the polar Kerr components and the longitudinal Kerr components are measured together. The differences in the Kerr rotation across the permalloy strip can be seen in Figure 5.12, and it is clear that the largest field is achieved between the tracks.

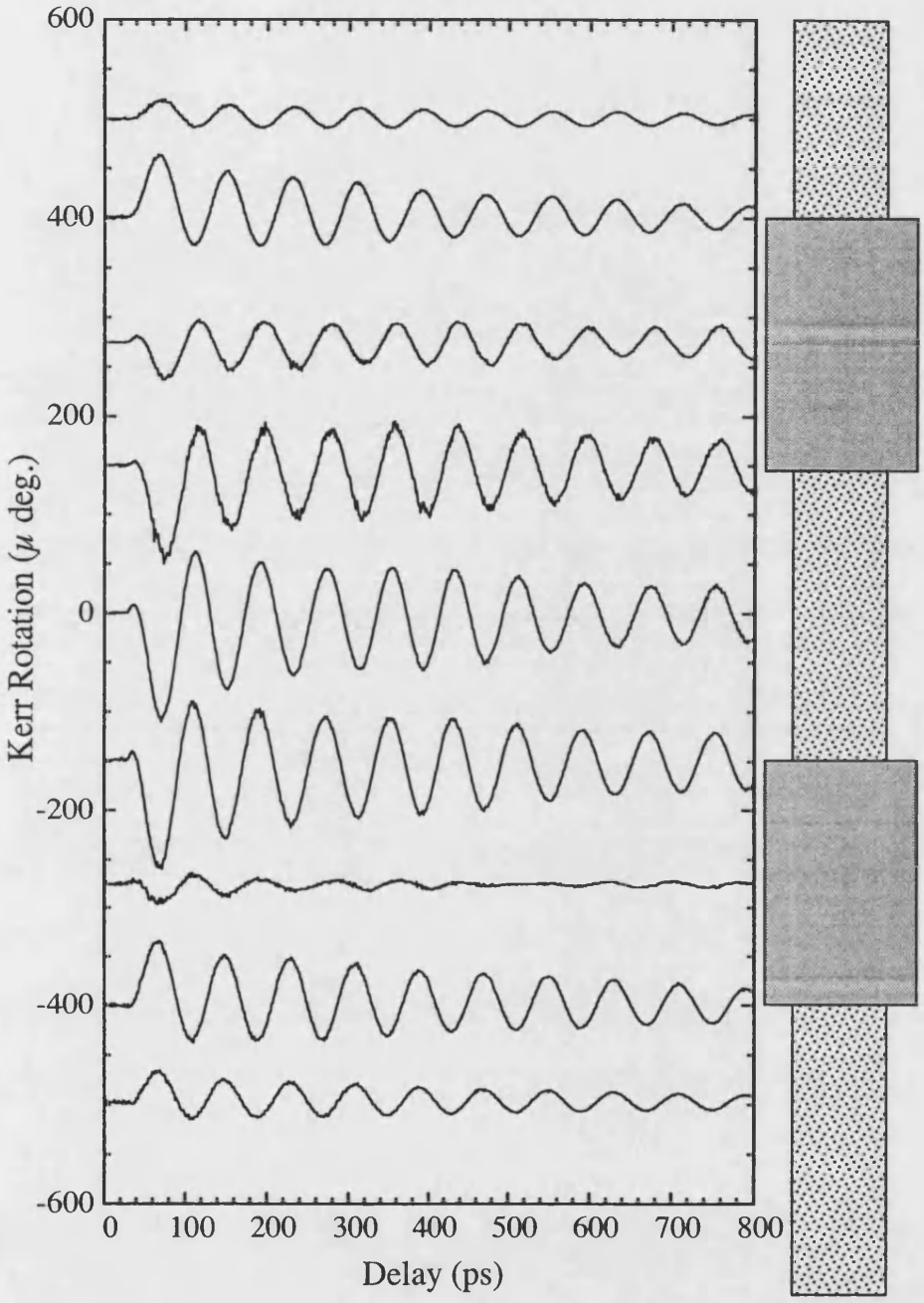

FIGURE 5.12: Dependence of the Kerr rotation of a 500 Å thick permalloy(78) film across the stripline, showing a measurement of the magnetisation distribution. The schematic on the right shows the position of the permalloy thin film under that of the two horizontal tracks of the stripline.

5.4.2 Ferromagnetic Resonance

The small amplitude oscillations that are present in the time resolved Kerr rotation traces in the previous section are able to be discussed in terms of the established theory on the ferromagnetic resonance state [20, 19, 46]. The dominant frequencies in the traces were extracted from the data by use of a FFT program, and plotted together with a fit using Equation 5.26 [42] to compare the modal frequencies observed with the ferromagnetic resonance frequency, f_{FMR}. Figure 5.13 shows the observed frequencies as a function of the in-plane d.c. applied field.

$$f_{\mathrm{FMR}} = \frac{\gamma}{2\pi}\sqrt{H\left(H + 4\pi M_s\right)} \tag{5.26}$$

The gyromagnetic ratio, γ, was taken to be $1{\cdot}76\times10^{7}\,\mathrm{s^{-1}\,Oe^{-1}}$ for permalloy, $1{\cdot}84\times10^{7}\,\mathrm{s^{-1}\,Oe^{-1}}$ for iron and $1{\cdot}91\times10^{7}\,\mathrm{s^{-1}\,Oe^{-1}}$ for nickel, where the value of the g-factor for each material was taken from the literature [47]. Values for the saturation magnetisation were also taken from the literature [39], so that $4\pi M_s$=9·5 kOe for permalloy, 18·5 kOe for cobalt and 21·5 kOe for iron. Good agreement between this simple model and the experimental data, suggests a weak damping effect [44], and is supported by the relatively long decay times extracted by fitting the time resolved Kerr rotation traces.

5.4.3 Spin Wave Resonance

The dominant frequency is predicted by the simple FMR Kittel equation, however the higher frequency that is observed can be described in terms of spin wave

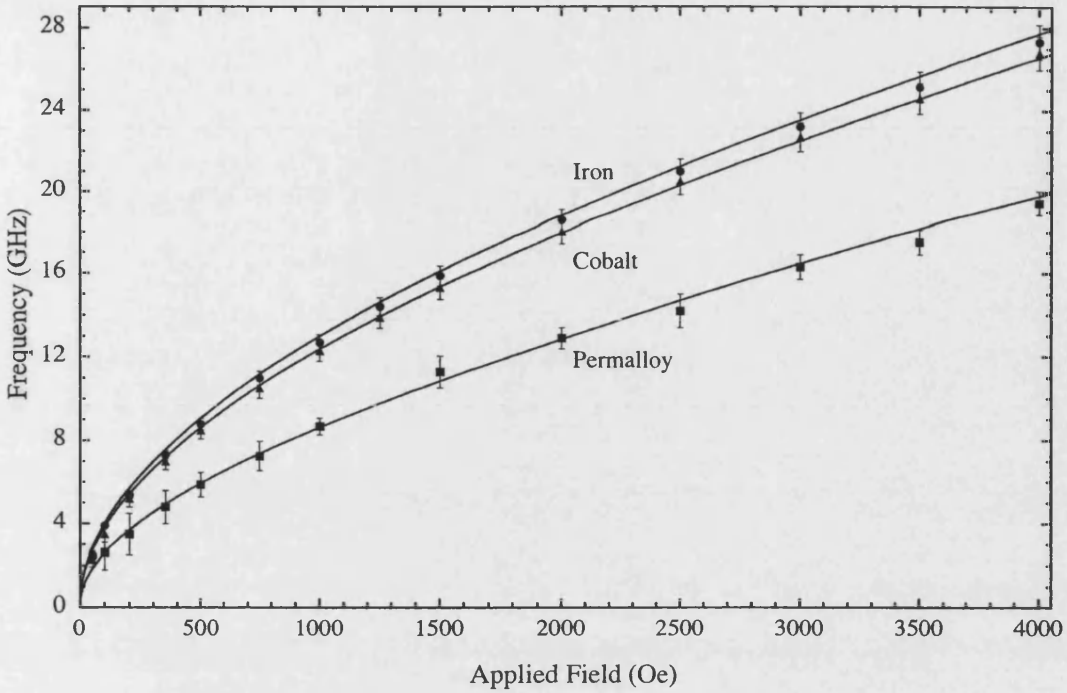

FIGURE 5.13: Dependence of the FMR oscillation frequency as a function of applied field for iron (dots), cobalt (triangles) and permalloy (squares); and a fit to the data using the FMR frequency equation (solid lines), with values for the saturation magnetisation $4\pi M_s$, of 21,500 Oe, 18,500 Oe and 9,500 Oe for iron, cobalt and permalloy respectively.

resonance. If the electron spins at the surface of a thin magnetic film experience different anisotropy fields than the electron spins in the bulk, then long wavelength spin waves can be excited. Effectively, the surface spins can be pinned, and the transient magnetic field applied perpendicular to the film plane can excite spin waves with an odd number of half-wavelengths. By adding a term [48] to the Kittel equation, Equation 5.26, that includes the spin wave exchange constant $D = 2A/M_s$, where A is the exchange stiffness constant [42], and the spin wave wavevector $q = n\pi/d^2$ where n is the mode of the spin wave and d is the film thickness, the frequency of the spin wave resonance that is observed can be

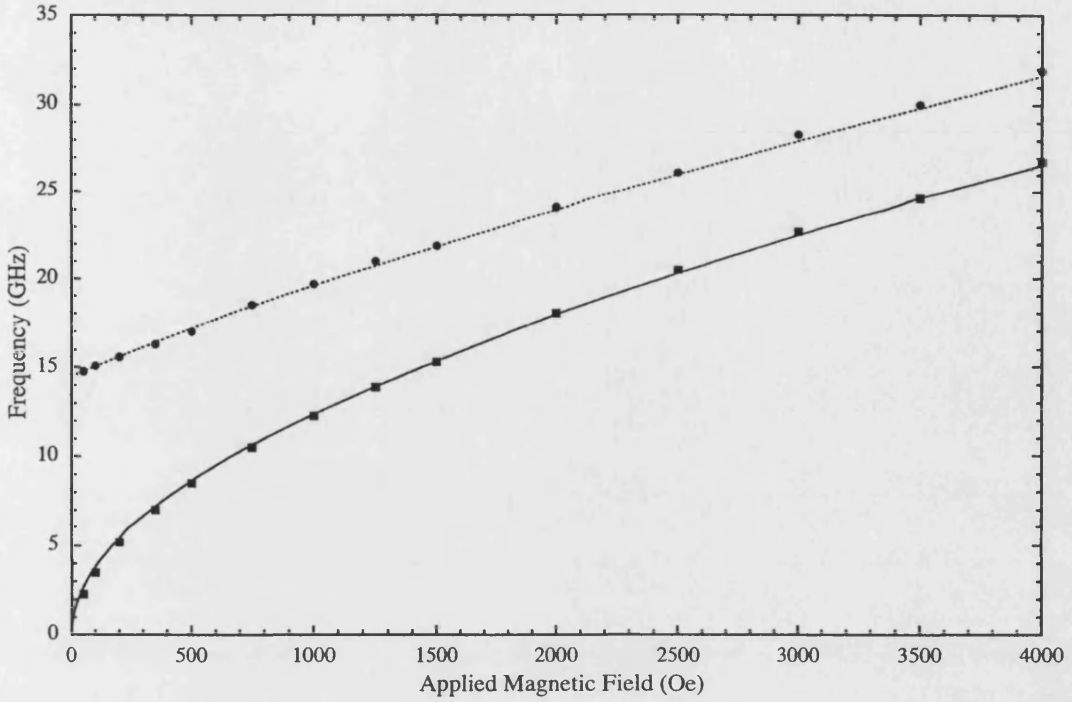

FIGURE 5.14: The FMR frequencies for cobalt (squares), with a fit using a value for the saturation magnetisation $4\pi M_s$ of 18,500 Oe (solid line), together with frequencies for the surface pinned spin waves in cobalt (circles) with a fit (dashed line) including the extra term Dq^2 to account for the spin wave.

predicted for the first frequency mode, $n = 1$.

$$f_{\mathrm{SW}} = \frac{\gamma}{2\pi}\sqrt{(H + Dq^2)\,(H + Dq^2 + 4\pi M_{\mathrm{s}})} \tag{5.27}$$

The spin wave stiffness constant is a phenomenological constant, and is significantly larger for cobalt than it is for either permalloy(78) or iron [42]. For cobalt $A = 1{\cdot}1{\times}10^{-6}\,\mathrm{erg\,cm^{-1}}$, which results in a value of $1{\cdot}49{\times}10^{-9}\,\mathrm{erg\,cm^2}$ for D. Figure 5.14 shows a plot of the bias field dependence of the ferromagnetic resonance and the surface pinned spin wave resonance.

5.5 Summary

The time resolved measurement of the MOKE has been achieved in various ferromagnetic materials. In addition, small amplitude FMR oscillations have been observed and have been shown to agree well with a simple model taken from the established theory, including the contribution by surface pinned spin waves.

In the future this technique could be extended to the observation of the time resolved Kerr rotation by such materials as MnAs for example. By the use of the epitaxial lift-off technique described in §2.2.1, a stripline can be manufactured on, for example, sapphire with a small, $\sim 300\,\mu m^2$, chip of GaAs epilayer underneath the photoswitch. By this method, non-metallic ferromagnetic materials can be investigated by laying the sapphire device side down on to the surface of the sample. The photoswitch is gated, and the sample probed, through the sapphire substrate. This provides a non-destructive method by which the magnetic properties of a material may be investigated. The fabrication of this device was attempted over some time, but the required levels of atmospheric cleanliness were found to be superior to those available.

The fact that the technique yields information about spin dynamics and spin-spin interactions, is also of possible use in the future. For some materials there are no lasers of the correct energy to tune to the band-gap and thus detailed investigation of some electron properties, in particular those associated with spin, are very difficult to achieve. This technique offers a way by which the spin-lattice relaxation time may be measured without the need for a light source tuned to the band gap of the material.

References

[1] M. Mansuripur
'The Physical Properties of Magneto-optical Recording.'
Cambridge University Press, Cambridge 1995.
ISBN:0521634180

[2] M.H. Kryder
'Ultrahigh Density Recording Technology.'
MRS Bulletin pp. 17–19, **21**(9), 1996.

[3] S.D. Bader, G. Prinz *et al.*
'Surface, Interface and Thin-Film Magnetism.'
Journal of Material Research, pp. 1299–1341, **5**(6), June 1990.

[4] Z.Q. Qiu & S.D.Bader
'Surface Magneto-Optic Kerr Effect'
Review of Scientific Instruments, pp. 1243–1255, **71**(3), March 2000.

[5] M.J. Freiser
'A Survey of Magneto-Optic Effects.'
IEEE Transactions on Magnetics, pp. 152–161, **MAG-4**(2), June 1968.

[6] H. le Gall, R. Sbiaa *et al.*
'Present and Future of Magneto-optic Recording Materials and Technologies.'
Journal of Alloys and Compounds, pp. 677–687, **275**, 1998.

[7] E.R. Moog & S.D. Bader
'SMOKE signals from Ferromagnetic Monolayers: p(1×1) Fe/Au(100).'
Superlattices and Microstructures, pp. 543–552, **1**(6), 1985.

[8] M. Nylvt, J. Ferré *et al.*
'Magneto-Optic Effects in a Stack of Magnetic Multilayer Dielectric Films.'
Journal of Magnetism and Magnetic Materials, pp. 175–176, **156**(1–3), April 1996.

[9] C. Chappert, H. Bernas, J. Ferré *et al.*
'Planar Patterned Magnetic Media Obtained by Ion Irradiation.'
Science, pp. 1919–1922, **280**, 19^{th} June 1998.

[10] T. Devolder, C. Chappert *et al.*
'Sub-50 nm Planar Magnetic Nanostructures Fabricated by Ion Irradiation.'
Applied Physics Letters pp. 3383–3385, **74**(22), 31^{st} May 1999.

[11] A full issue dedicated to magnetoelectronics.
Physics Today **48**(4), 1993.

[12] W. Wernsdorfer, K. Hasselbach *et al.*
'Dynamical Measurement of Domain Wall Nucleation and Annihilation in Individual Amorphous Co Particles.'
Physics Review B, pp. 3341–3347, **53**(6), 1^{st} Feb. 1996.

[13] R.H. Koch, J.G. Deak *et al.*
'Magnetisation Reversal in Micron Sized Magnetic Thin Films.'
Physical Review Letters, pp. 4512–15, **81**(20), 16^{th} Nov. 1998.

[14] M. Bauer, R. Lopusnik *et al.*
'Suppression of Magnetic Field Pulse Induced Magnetization Precession by Pulse Tailoring.
Applied Physics Letters, pp. 2758–2760, **76**(19), 8^{th} May 2000.

[15] G. Meier & T. Matsuyama
'Magnetic Electrodes for Spin-Polarized Injection into InAs.'
Applied Physics Letters, pp. 1315–1318, **76**(10), 6^{th} March 2000.

[16] S.Gardelis, E.H. Linfield it et al.,
'Spin-Valve Effects in a Semiconductor Field Effect Transistor: A Spintronic Device.'
Physical Review B, pp. 7764–7767, **60**(11), 15^{th} Sept. 1999.

[17] S. Lemerle, J. Ferré *et al.*
'Domain Wall Creep in an Ising Ultrathin Magnetic Film.'
Physical Review B, pp. 849–852, **80**(4), 26^{th} Jan. 1998.

[18] M. Johnson, A. Y. Elezzabi & M.R. Freeman
'Direct Measurement of the Conduction Electron Spin-Lattice Relaxation Time T_1 in Gold.'
Physical Review Letters, pp. 3220–3223, **77**(15), 7^{th} Oct. 1996.

[19] J. Wu, J.R. Moore *et al.*
'Optical Pump-Probe Studies of the Rise and Damping of Ferromagnetic Resonance Oscillations in a Thin Fe Film.'
Journal of Magnetism and Magnetic Materials, pp. 189–198, **222**, 2000.

[20] W.K. Hiebert, A. Stankiewicz & M.R. Freeman
'Direct Observation of Magnetic Relaxation in a Small Permalloy Disk by Time-Resolved Scanning Kerr Microscopy.'
Physical Review Letters, pp. 1134–1137, **79**(6), 11^{th} Aug. 1997.

[21] M. Faraday
'On the Magnetisation of Light and the Illumination of Magnetic Lines of Force.'
Philosophical Transactions of the Royal Society (London), pp. 1–20, **136**, 1846.

[22] J. Kerr
'On Rotation of the Plane of Polarisation by Reflection from the Pol of a Magnet.'
Philosophical Magazine, pp. 321–343, **3**, 1877; *ibid.* pp. 161, **5**, 1878.

[23] H.R. Hulme
Proceedings of the Royal Society (London), pp. 237 Series A, **135**, 1932.

[24] P.N. Argyres
'Theory of the Faraday and Kerr Effects in Ferromagnetics.'
Physical Review, pp. 334–345, **97**(2) 15^{th} Jan. 1951.

[25] L.D. Landau & E.M. Lifshitz
'Landau and Lifshitz Course of Theoretical Physics' Vol.8 *Electrodynamics of Continuous Media'*
Butterworth Heinenman Ltd., 2^{nd} Edition, 1984.
'On the Theory of the Dispersion of Magnetic Permeability in Ferromagnetic Bodies'.
Soviet Physics: Semiconductors, pp. 153–169, **8**, 1935.

[26] A. Shadowitz
'The Electromagnetic Field.'
M^{c}Graw & Hill, Inc. New York, USA 1975.
ISBN:0-07-056268-3

[27] W. Voigt
'Magneto- und Elektro-optic.'
Teuner, Leipzig, 1908;
'Handbook der Elektrizität und des Magnetismus.'
Barth, Leipzig, 1915. Volume IV, 2, pp.39–.

[28] R.M.A. Azzam & N.M Bashara
'Ellipsometry and Polarised Light.'
Amsterdam:North Holland, 1977.

[29] A. Hubert & R. Schäfer
'Magnetic Domains — The Analysis of Magnetic Microstructures.'
Springer-Verlag, Berlin, 1998. ISBN:3-540-64108-4

[30] R.P. Hunt
'Magnetooptics, Lasers and Memory Systems.'
IEEE Transactions on Magnetics, pp. 700–707, **MAG-5**(4), Dec. 1969;
'Magneto-Optic Scattering from Thin Solid Films.'
Journal of Applied Physics, pp. 1652–1671, **38**(4), 15^{th} March 1967.

[31] C.-Y. You & S.-C. Shin
'Derivation of Simplified Analytic Formulae for Magneto-Optical Kerr Effects.'
Applied Physics Letters, pp. 1315–1317, **69**(9), 26^{th} Aug. 1999.

[32] C.-Y. You & S.-C. Shin
'Generalized Analytic Formulae for Magneto-Optical kerr Effects.'
Journal of Applied Physics, pp. 541–546, **84**(1), 1^{st} July 1998.

[33] G. Metzger, P. Pluvinge *et al.*
'Termes Linéaires et Quadratiques dans l'Effet Magnéto-Optique de Kerr.'
Annales de Physique, pp. 5-12, **t.10**, 1965.

[34] Toshiba Ultrabright LED, manufacturer's code TLRH190P.

[35] The laser diode was purchased from RS and consisted of an InGaAs substrate, code number, XX1234

[36] L. Callegaro & E. Puppin
'Lasers and light-emitting diodes as sources for fixed wavelength magneto-optical phase modulated ellipsometry.'
Review of Scientific Instruments, pp. 5375–5376, **66**(11), Nov. 1995.

[37] D.S. Kliger
'Polarized Light in Optics and Spectroscopy'
Academic Press, 1990.
ISBN:012414975

[38] Hamamatsu XX-143 matched photodiodes.

[39] Landolt-Börnstein
'Physics of Group IV Elements and III-V Compounds.'
Springer-Verlag, Berlin, Volume 17(a)
ISBN: 0387106103

[40] T. Gilbert
'A Langrangian Formulation of the Gyromagnetic Equation of the Magnetisation Field.'

The Physical Review, pp. 1243, **100**, 1955;
'Equation of Motion of Magnetization.'
Armour Research Foundation Report, No. 11, Chicago, Jan. 25^{th} 1955.

[41] F. Bloch
'Nuclear Induction.'
Physical Review pp. 460–474, **70**, 1946.

[42] R.F. Soohoo
'Magnetic Thin Films.'
Harper & Row, New York, USA, 1965

[43] *'Micromagnetics.'*
W.F. Brown Jnr.
Wiley, New York, 1963.

[44] J.A.C. Bland & B. Heinrich (Eds.)
'Ultrathin Magnetic Structures I : An Introduction to the Electronic, Magnetic and Structural Properties.'
Springer-Verlag, Berlin, 1994.
ISBN 3-540-57407-7

[45] V. Dureuil, C. Ricolleau *et al.*
'Phase Transitions in Co Grown by Pulsed Laser Deposition.
European Physical Journal D, pp. 83–88, **14**(1), April 2001;
C. Chappert & P. Bruno
'Magnetic Anisotropy in Metallic Thin Films and Related Experiments on Cobalt films.'
Journal of Applied Physics, pp. 5736–5741, **64**, 1998.

[46] T.M. Crawford, P. Kabos *et al.*
'Coherent Control of Precessional Dynamics in Thin Film Permalloy.'
Applied Physics Letters, pp. 2113–2116, **76**(15), 10^{th} April 2000.

[47] *'Ferromagnetism'*
R.M. Bozorth
D. Van Nostrand Company, Ltd., London (1968)

[48] *'Spin Dynamics in Confined Magnetic Structures.'*
Edited by B. Hillebrands, Selected Topics in Apllied Physics
Springer-Verlag, Berlin-London-New-York, (Nov. 2001)

Chapter 6

Conclusions and Discussion

The THz radiation emitted from InAs surfaces illuminated by ultrafast pulses of near infrared radiation has been studied, and the dependence of the emitted average power and the amplitude of the electric field transient has been investigated in terms of the dependence on the strength of the magnetic field, the sample temperature, the doping levels within the sample, the majority carrier type, the incident optical power density and the position of the sample relative to the applied magnetic field. The absorption coefficient for near infrared radiation of wavelength 765 nm incident on an n-type InAs sample with a carrier density of $2{\cdot}0\times10^{16}\,\mathrm{cm}^{-3}$ was found to be $(2{\cdot}5\pm0{\cdot}25)\times10^{5}\,\mathrm{cm}^{-1}$. This result shows that a large fraction of the photoexcited carriers are created within the region of the intrinsic surface accumulation layer. The emitted transient electric field has been simulated by assuming a model that includes a large contribution from coherent plasmon motion. This model has been shown to agree well with the observed electric field transients, and an extension to the work could include investigating the THz emission from GaAs p-i-n structures, where the form and direction

of the internal electric field is better understood. Extensions to the model that could be included in the future involve taking into account any significant effects caused by a diffusion current in the surface region.

A maximum generated average power of $\sim 30\,\mu$W was found for an *n-type* InAs sample with a carrier concentration of $1{\cdot}7\times10^{15}\,\mathrm{cm}^{-3}$ at a sample temperature of 10 K and a magnetic field strength of 6 T, with an incident near infrared average pump power of 1·2 W. This measurement could be repeated using a newly acquired helium cooled silicon bolometer and across a greater range of samples, to determine whether the emitted average power does indeed decrease with increasing carrier concentration. By using a bolometer, the problem of the dependence of the detection bandwidth of the receiver is overcome. Additionally, it would be advantageous to obtain more InAs samples over the range of carrier concentrations presented here. Particularly samples in the range of carrier concentrations that have bulk plasma oscillations in the frequency range encompassed by the detection bandwidth of the receiver.

An experiment that must be performed in the near future, so to better understand the mechanisms involved in the generation of the THz radiation, is to vary the energy of the incident light from just below the band gap of InAs ($\sim$0·40 eV), to above the energy used in this study ($\sim$1·63 eV). The free electron laser facility at FELIX in Holland is one such source of tunable radiation. By simply measuring the emitted average power, even at zero magnetic field, in the *p*-polarised geometry, a great deal could be learnt about the generation mechanisms, and the role of the diffusion current can be examined.

It has been demonstrated that an InAs chip, illuminated by ultrafast near infrared pulses can be used as a source of coherent THz radiation for the purposes of

FIR spectroscopy. This is the first reported use of InAs as a coherent source of radiation to investigate a separate material. The advantage of such a technique is that the optical beam and the THz radiation are self-aligning along the axis of the probing beam. Unfortunately, however, the time delay between near-infrared pulse, and the electrical THz transient cannot be varied very easily.

Finally, the magneto-optic Kerr effect has been measured in the time domain, and has been used to study small amplitude ferromagnetic resonance oscillations in different ferromagnetic thin films. The first reported observation of time resolved FMR oscillations from cobalt thin films has been presented, and the construction of the experimental system will allow other materials, such as manganese implanted GaAs or MnAs clusters embedded in GaAs, to be studied in a similar way. More investigation into the fabrication of a time resolved MOKE device for use with the ferromagnetic semiconductor materials needs to take place, so as to increase the production yield.

Initially an experiment in which the coherent control of the oscillations can be demonstrated, could be performed. In which two optical pulses, each incident on the photoswitch, but delayed in time relative to one another, could gate current pulses. The first of these current pulses would excite the oscillations, and the second pulse would excite more oscillations which would be 180° out of phase relative to the first. Hence the small amplitude FMR oscillations could be controlled.